Politecnico di Torino

Master of Science in Nanotechnologies for ICTs

Politecnico di Torino

Danmarks Tekniske Universitet

Master Degree Thesis

A coplanar, low-variation impedance flow cytometry design for characterization of bacteria

Supervisors:
Maria Dimaki
Christian Vinther Bertelsen
Rahul Singh
Winnie Edith Svendsen
Matteo Cocuzza

Candidate:
Sara Pittelli

October 24, 2025

If you can meet with Triumph and Disaster
And treat those two impostors just the same

Rudyard Kipling
(inscribed above the entrance to Centre Court at Wimbledon)

Preface

This thesis was prepared at the department of DTU Bioengineering in fulfillment to the Learning Agreement of the Erasmus+ exchange program. The project was entirely carried out in the facilities of the Technical University of Denmark campus in Kgs. Lyngby. It started in February 2025 and lasted for 5 months. The work was done in the NanoBio Integrated Systems (NaBIS) group, with supervision from Senior Researcher Maria Dimaki, Postdoc Christian Vinther Bertelsen, PhD student Rahul Singh and Professor Winnie Edith Svendsen.
Professor Matteo Cocuzza was the Italian supervisor at Politecnico di Torino.
Part of the work described in this report was done in collaboration with fellow student Sara Di Paolo.

Abstract

English version

Electrical characterization of bacteria is becoming increasingly relevant in various scientific fields, with impedance flow cytometry (IFC) emerging as a powerful label-free technique. However, coplanar electrode configurations suffer from a key limitation: the signal depends on the particle position above the electrodes, which can make differentiation of particles unreliable. This thesis investigates strategies to minimize the positional dependence of the signal through finite element method simulations in COMSOL. Several electrode layouts are explored and asymmetric gaps are found to introduce signal features that correlate with particle position in the channel. Two parameters related to width and amplitude of peaks in the characteristic IFC signal are identified as potential indicators of vertical position. An experimental setup including a 3D-printed holder for the chip and a 3D-printed framework for the alignment of electrodes in the channel is developed to experimentally validate the simulation results. Measurements on polystyrene beads show trends consistent with simulations, supporting the feasibility of a compensation strategy for the positional dependence of the signal based on the extracted parameters. While a full compensation model is not achieved here and tests with biological samples are yet to be performed, this study establishes a promising foundation for further research and future improvements in the performance of IFC systems using coplanar electrode configurations.

Danish version

Elektrisk karakterisering af bakterier bliver i stigende grad relevant inden for forskellige videnskabelige felter, og impedans-flowcytometri (IFC) er ved at etablere sig som en kraftfuld, mærkningsfri teknik. Dog lider koplanare elektrodekonfigurationer af en væsentlig begrænsning: signalet afhænger af partiklens position over elektroderne, hvilket kan gøre det vanskeligt at differentiere mellem partikler pålideligt. Denne afhandling undersøger strategier til at minimere signalets positionsafhængighed gennem simuleringer med finite element-metoden i COMSOL. Flere elektrodegeometrier analyseres, og asymmetriske afstande mellem elektroderne viser sig at frembringe signaturer i signalet, der korrelerer med partiklens position i kanalen. To parametre, relateret til bredden og amplituden af toppene i det karakteristiske IFC-signal, identificeres som potentielle indikatorer for den vertikale position. Et eksperimentelt setup, herunder en 3D-printet holder til chippen og en 3D-printet ramme til justering af elektroder i kanalen, udvikles for at eksperimentelt validere simuleringsresultaterne. Målinger på polystyrenkugler viser tendenser, der stemmer overens med simulationerne og understøtter muligheden for at udvikle en kompensationsstrategi for signalets positionsafhængighed baseret på de udtrukne parametre. Selvom en fuld kompensationsmodel ikke er opnået i dette arbejde, og tests med biologiske prøver endnu ikke er udført, udgør dette studie et lovende fundament for videre forskning og fremtidige forbedringer af IFC-systemers ydeevne med koplanare elektrodekonfigurationer.

Acknowledgments

First of all I would like to thank my DTU supervisors, Maria Dimaki, Christian Vinther Bertelsen, Rahul Singh and Winnie Edith Svendsen, for their continuous guidance and constant support. I am grateful for the kindness with which you have welcomed me and for the faith you have put in my abilities. Your gentle encouragement, patience and insightful feedback have been essential for the progression of this project. I will carry with me the passion and dedication you put into your work for a long time. Thank you for sharing your knowledge with me.

I would like to express my gratitude to my Italian supervisor Matteo Cocuzza for his availability throughout my exchange year in Denmark.

Un ringraziamento speciale va ai miei genitori, che con fiducia e amore inossidabili mi hanno donato la libertà di seguire la mia strada. Non importa dove io mi trovi nel mondo, sono sempre in grado di sentire il vostro supporto con me e so che nulla potrà mai cambiare ciò. Avete dato forma alla persona che sono oggi e di questo sono orgogliosa, quindi grazie mamma e papà.

Grazie anche a tutta la mia famiglia: zii, cugini e nonna Gemma, che non ha mai smesso di credere in me e di sostenermi ad ogni passo.

Un enorme ringraziamento va alla mia cara amica Sara, con cui ho condiviso gioie e dolori di una indimenticabile esperienza danese. Lavorare su questa tesi senza di te non sarebbe stato altrettanto divertente e stimolante, e chiamarti "fellow student" non rende giustizia al legame che ci unisce.

Grazie ai miei amici di sempre, Riccardo, Greta e Arianna, per aver gioito con me ad ogni traguardo: il nostro rapporto è una delle cose di cui vado più fiera e sono immensamente grata di poter sempre contare su di voi.

Grazie alla mia amica Claudia, che mi ha accompagnata negli anni universitari più difficili. Condividere con te interessi accademici e personali mi ha regalato momenti di serenità indispensabili.

Grazie ai miei amici della magistrale a Torino, per aver alleggerito interminabili sessioni di studio ed avermi incoraggiato a dare sempre il massimo.

Grazie ai miei amici italiani in Danimarca, che mi hanno permesso di trovare una comunità di persone che mi capisse e non mi hanno mai fatta sentire sola.

Thank you to all the international people with whom I have shared the past year, for giving me a fresh perspective on the world.

Finally, thank you to everything that makes me me, to my cats, for never failing at providing the sweetest distraction, and to music, for inspiring me to keep searching for purpose and push on through.

Contents

Chapter 1

Introduction

1.1 Motivation

The analysis of bacteria such as *Escherichia coli* (*E. coli*) is crucially relevant for multiple reasons across various fields, including food safety, environmental science and biotechnology. For instance, many different strains of *E. coli* exist, and some of them are pathogenic for humans [1]. Therefore, knowing their characteristics is fundamental in distinguishing harmful strains and limiting their concentration in potentially dangerous environments for public health, such as bathing ocean waters. Furthermore, monitoring the presence of *E. coli* in food is important in ensuring that hygiene standards are met in food production and processing [2]. In biotechnology, the presence of bacteria such as *E. coli* in bioreactors is not inherently unwanted; in fact, they are often intentionally used in many processes, e.g. for protein production [3]. Whether bacteria are beneficial or detrimental depends entirely on the specific bioprocess. Being able to detect and identify bacterial species is fundamental for monitoring, controlling and optimizing the bioreactor performance. Identification relies on parameters such as morphology and composition and, in this context, electrical characterization has emerged as a rapidly advancing technique for bacterial analysis.

In order to electrically characterize bacteria, using lab-on-a-chip devices can grant many advantages, the main of which is the ability to bypass the need for full laboratory equipment that is often rather expensive and requires expertise to be operated. Moreover, the analysis can be performed in situ, allowing for real time monitoring and faster decision-making without the delays associated with conventional laboratory processing. In addition to the intrinsic advantages of lab-on-a-chip devices, impedance flow cytometry offers a label-free method of analysis. This technique is commonly integrated in lab-on-a-chip systems and it eliminates the need for fluorescent markers, simplifying sample preparation and reducing both time and costs. Overall, the combination of miniaturization, portability and ease of use makes IFC a highly promising tool for electrical characterization of bacteria.

1.2 Electrical characterization

The origins of impedance flow cytometry (IFC) for the monitoring of liquid samples in real time can be found in the Coulter counter, a device for the counting and sizing of particles suspended in electrolytes that was first patented in 1953. The term *flow cytometry* was officially agreed on by the Conference of the American Engineering Foundation in 1976 and it gained traction in the scientific community rather quickly [4]. It is now employed mainly for labeled biosensors: particles are marked with a fluorescent dye before they can be discriminated based on the scattered light and fluorescence generated by a sample that has been optically excited with a laser [5]. The main concern about this method is the necessity for a marker that is specific to only one type of particle and that is where impedance flow cytometry finds the ground for its establishment, since no labeling of the sample is required. The first applications of IFC involved mainly the probing of blood cells populations [6], but the target fields are rapidly expanding.

As suggested by its name, IFC aims at characterizing particles suspended in a fluid by means of impedance measurements. It requires a microfluidic channel with patterned electrodes supplied with an AC voltage: as the sample flows through the channel, the signal at the electrodes is recorded and analyzed. The characterization of particles is achieved by the perturbation that the electric field undergoes when a particle interacts with it. Depending on the output signal, relevant physical parameters of the perturbing object can be extracted, such as electrical conductivity and permittivity. Based on the frequency of the probing signal, it is even possible to investigate different layers of the particles, including cell core or cell membrane when analyzing biological material [7].

As will be detailed in the next Chapter, there are generally two configurations for the electrodes: front-facing (Figure 1.1a) or coplanar (Figure 1.1b). A coplanar layout refers to a configuration in which all electrodes are patterned on the same plane, i.e. on the same wall of a microfluidic channel. This geometry simplifies fabrication, as it eliminates the need for precise vertical alignment typical of front-facing electrodes. However, in a coplanar setup, the electric field is generated horizontally between the electrodes, resulting in a non-uniform field distribution. The non-uniformity causes the recorded signal to vary with particle position, which is a key challenge associated with coplanar electrode configurations in IFC. This aspect will be one of the main concerns of the project.

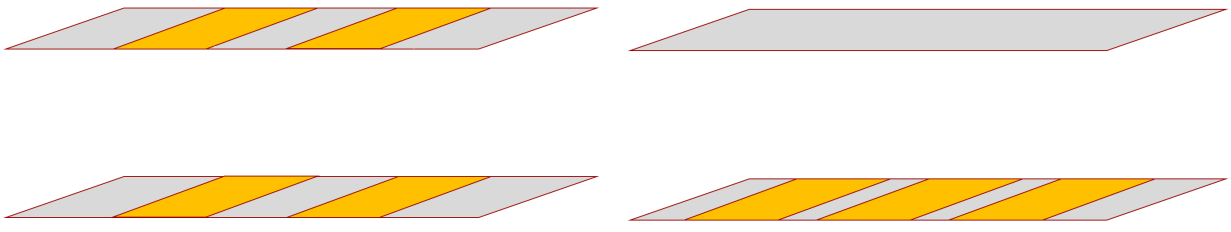

(a) (b)

Figure 1.1: Common electrode configurations for IFC: (a) front-facing layout and (b) coplanar layout.

1.3 Electrode configurations in scientific literature

The optimal shape for electrodes in an IFC setup is a topic that has already been investigated in scientific literature quite extensively.

One of the most creative designs, ideated by Caselli *et al.* in 2010 [8], involved two circumferential arrays of electrodes on the walls of a circular channel (Figure 1.2a). Excitation was applied to the electrodes with different combinations in finite element method (FEM) analysis, which showed how that can yield information on the morphology of the particles. Discrimination of cells and reconstruction of their volume is possible with this configuration; however, due to fabrication concerns, no prototype has ever been manufactured.

The same research group came up with a coplanar design in 2014 [9], involving four electrodes aligned in two different directions (Figure 1.2b). This allowed for the determination of the morphology of the particles once again, not depending on their position in the channel: that was useful to determine the anisotropy of cells, but still no information on the position of the particle along the height of the channel could be extracted.

Furthermore, in 2018, Caselli *et al.* [10] achieved position determination of particles independent on their size by applying an AC voltage to diagonally opposite electrodes and recording the differential signal on the remaining pair. The innovative wiring scheme can be applied both to front-facing electrodes and to coplanar ones, employing a set of so-called *liquid electrodes* [11]. The coplanar layout is showed in Figure 1.2c.

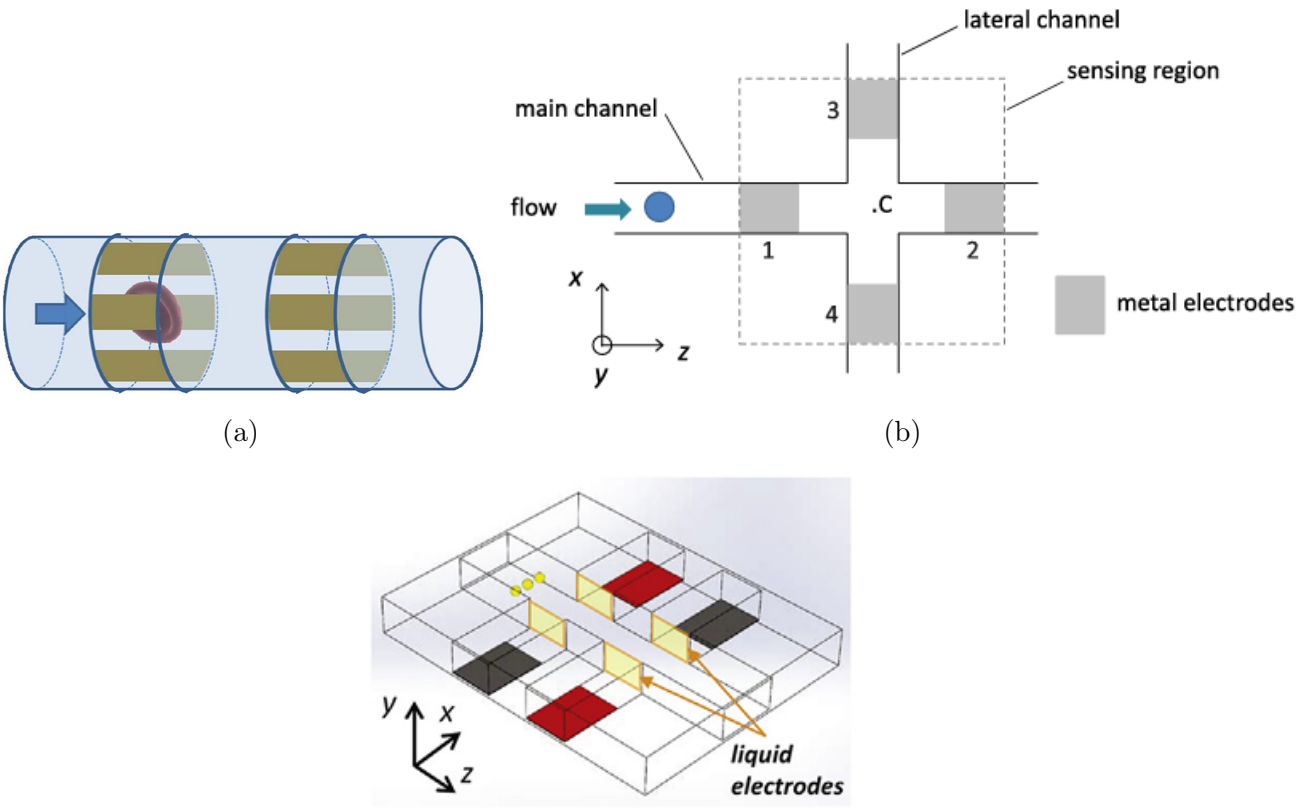

(a) (b)

(c)

Figure 1.2: Innovative IFC electrode designs from Caselli et al.: (a) two circumferential arrays of electrodes [8], (b) four electrodes aligned in two different directions [9] and (c) liquid electrodes in a coplanar layout [10].

In 2017, De Ninno *et al.* [12] designed a five coplanar electrodes layout, with two floating electrodes in between the active ones (Figure 1.3a): that allowed the research group to conceive a new metric correlating with particle trajectory, based on the peculiar shape of the recorded signal. Such design may be considered as very promising because it allowed for the correct sizing of the particles, completely eliminating the positional dependence issue without the need for focusing.

In the same year, Wang *et al.* [13] invented a non-parallel two-electrode design (Figure 1.3b), which turned out to be successful in the detection of particle position and discrimination of transverse trajectories. It worked even when the sample was composed of particles with various diameters.

The two previously described layouts were mixed together by Tang *et al.* [14] in 2021, when a five coplanar electrodes layout was designed. The two floating electrodes were not parallel to the active ones (Figure 1.3c) and that allowed for the determination of cell asymmetry irrespective on its position in the channel.

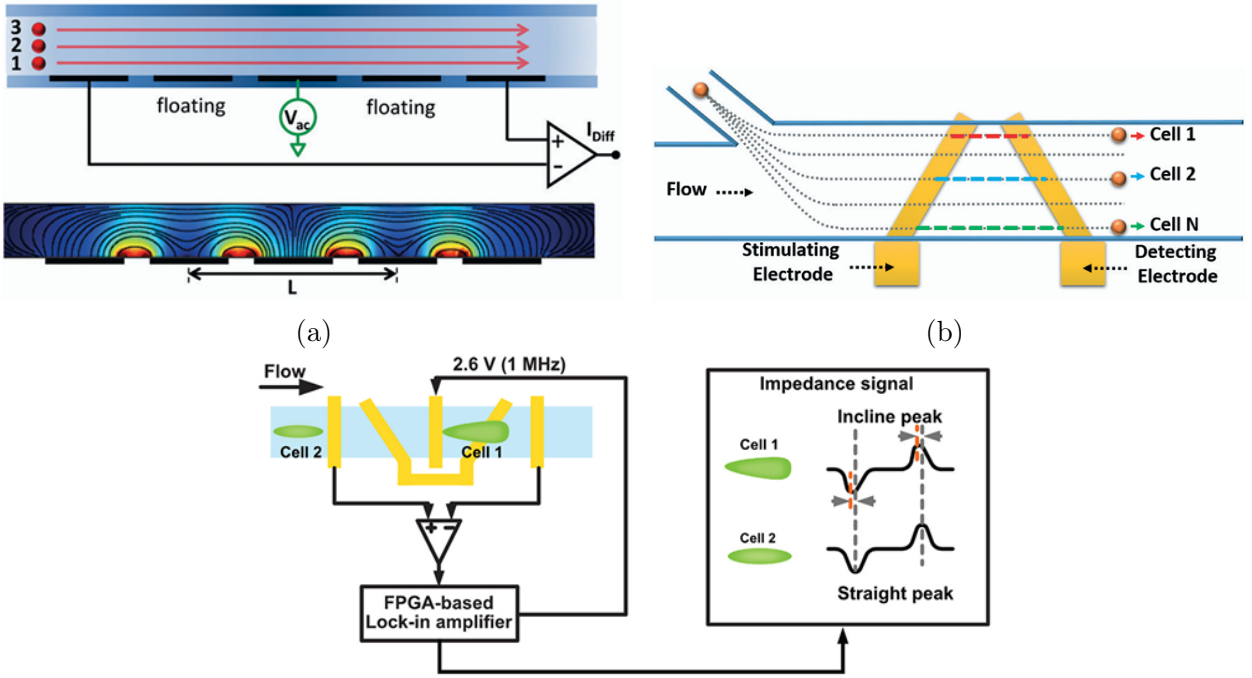

Figure 1.3: IFC coplanar electrode designs from literature: (a) five parallel electrodes by De Ninno *et al.* [12], (b) two non-parallel electrodes by Wang *et al.* [13] and (c) five non-parallel electrodes by Tang *et al.* [14].

In 2019, Reale *et al.* [15] combined a set of liquid electrodes with five simple coplanar electrodes (Figure 1.4a): the former allows for the determination of the lateral position of the particle in the channel, while the latter permits the extraction of information on the vertical position.

In 2021, Farooq *et al.* [16] optimized a set of three non-identical coplanar electrodes (Figure 1.4b) to differentiate non-spherical particles while keeping a high signal-to-noise (SNR) ratio.

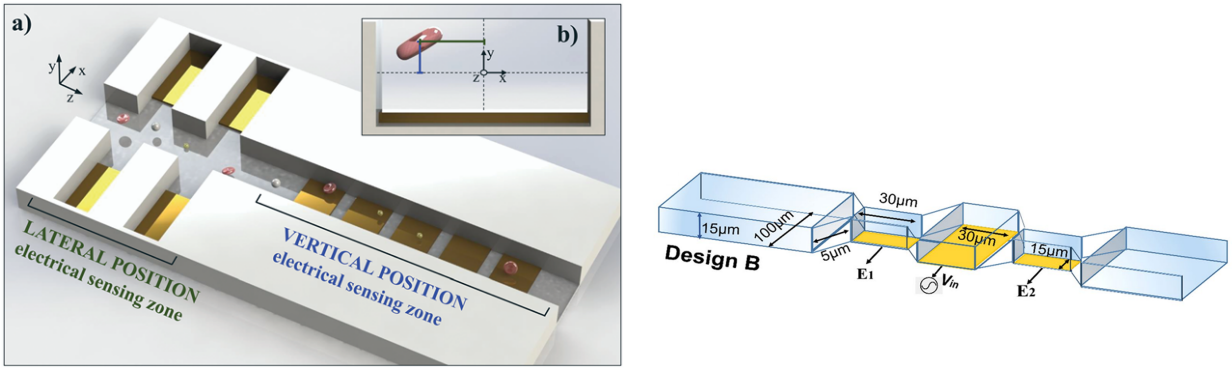

(a) (b)

Figure 1.4: More IFC coplanar electrode designs from literature: (a) liquid electrodes combined with five parallel electrodes by Reale *et al.* [15] and (b) three non-identical electrodes by Farooq *et al.* [16].

Although numerous electrode configurations have already demonstrated promising results in achieving a position-independent signal, there is a scarcity of studies focusing on particles smaller than 5 µm in diameter in combination with coplanar electrodes: considering that bacteria such as *E. coli* typically range from 1 to 3 µm in length, with an average radius of approximately 0.5 µm [17], this thesis aims at investigating and establishing methodologies for coplanar electrodes applicable at such microscale.

1.4 Problem framing

The work presented in this thesis serves as a foundation for the development of a device capable of providing comprehensive insight on the dielectric properties of bacteria. To achieve that, the electrodes for IFC that are going to be discussed here will ultimately need to be combined with a set of electrochemical impedance spectroscopy (EIS) electrodes. The EIS electrodes will be positioned in a dedicated trapping site where, ideally, only one single bacterium will get stuck due to variations in the hydraulic resistances of the channels. The idea for the device and its design is inspired by Feng *et al.* [18], who developed a similar system with the aim of enhancing the efficiency of electrical property measurement for single cells. The goal is to get information on the entire flow of particles with IFC, where only a limited number of frequencies can be investigated, and then obtain particle-specific properties exploiting EIS. In principle, the stationary condition of the trapped bacterium enables the acquisition of a full-frequency impedance spectrum. An exemplification of the concept for the final device is displayed in Figure 1.5. Fellow student Sara Di Paolo deals with the optimization of part 2 in her Master project, while part 1 is the topic of this thesis.

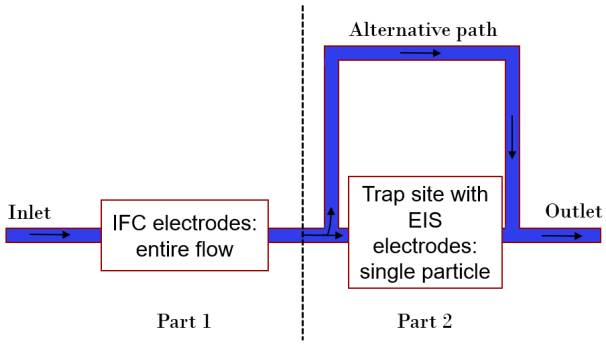

Figure 1.5: Conceptual sketch of the final device: IFC is performed on the entire flow (part 1), while a trapping site is designed to capture one single bacterium, allowing for EIS (part 2). Once the trap is full, the difference in hydraulic resistance between the two channels in part 2 will make the alternative path the preferred channel for the remaining flow. Inspired by [18].

For the trapped particle, the goal is to measure the electrical response over a wide range of frequencies. This approach allows for a detailed characterization of dielectric properties and enables the investigation of single-cell behavior. However, single-cell analysis is inherently time-consuming and has low throughput. In contrast, IFC allows for rapid analysis of large particle populations, which is desirable in most practical applications, but it typically operates at only one or two fixed frequencies. This results in limited information and yields an averaged response over all traveling particles, as the continuous nature of the flow prevents individual differentiation of each particle. Consequently, important biological variations at single-cell level may be missed. By immobilizing a particle, it becomes possible to accurately probe its electrical properties, so that cell-to-cell variability can be captured.

The combination of the two methods is therefore beneficial: single-particle analysis helps in determining the most suitable frequencies for IFC and provides particle-specific properties, while IFC gives insight into signal variations caused by particle position and allows for fast population probing. The combined information can improve accuracy and reliability of results.

1.5 Objectives and outline of the project

This project involves the designing, modeling and experimental testing of a device capable of providing real time position-independent information on the electrical properties of bacteria. The major goals are listed here.

- Optimize a coplanar electrode configuration using COMSOL simulations, with a focus on minimizing the signal dependence on particle position.
- Design a process that ensures proper alignment and bonding of the microfluidic device.
- Build an experimental setup for IFC integrating both fluidics handling and electronic connections.

- Test the experimental setup and validate the optimized electrode design through measurements performed on polystyrene beads and bacteria.

This is the end of **Chapter 1**. In **Chapter 2**, the theoretical background necessary to understand the topic at hand is delineated. **Chapter 3** illustrates the process of electrode optimization through FEM analysis and the data generated with COMSOL simulations is investigated. The experimental work starts in **Chapter 4**, where the physical chip and its fabrication process is described, while in **Chapter 5** an explanation on how the acquisition of data was possible is presented. **Chapter 6** focuses on the elaboration of experimental results and **Chapter 7** contains a disquisition on the agreement of such with simulated data, and the potential future work to be carried out. Finally, concluding remarks are included in **Chapter 8**.

Chapter 2

Theoretical background

2.1 Lab-on-a-chip devices

The term lab-on-a-chip (LOC) refers to a device that integrates multiple laboratory functions into a single portable chip. The advantages of such technology are numerous: analyses do not entail expensive facilities and equipment to be performed, the volume of sample required is very small and results can be obtained in a fast and efficient way. Consequently, the ease of operation makes them suitable for usage even in the least convenient settings, given that the systems can be hand-held and no specific training is needed for the user to operate. These characteristics place LOC devices among the perfect candidates to improve several research fields, including biotechnology and public health, thanks to the opportunity for the development of innovative diagnostics and treatment tools [19].

The first actual LOC was invented at Stanford University in 1979 to analyze volatile compounds, but interest for the technology in the scientific community spiked only in the late 1980s, with the improvement of microfabrication techniques; due to the small dimensions of the devices allowing for the investigation of similar-sized objects, cell biology has always been one of the main successful fields for LOCs [20]. The first official dedicated journal started in 2001 [21] and the appeal of such technology has been growing steadily in the past decades, in combination with the release of software dedicated to FEM analysis: the Microfluidics Module was launched on the market by COMSOL Multiphysics in 2011 [22].

The emergence of LOCs is tightly related to that of microfluidics, whose main notions relevant to the project at hand will be discussed in the following.

2.2 Microfluidics

In order to detect particles on the micrometer scale such as bacteria with IFC, the dimensions of the employed device must be of comparable size [6]; hence, the channels concerned in this project are micron-sized, and this permits the application of microfluidic theory to describe the dynamics of the flow in the system. A flow can be either viscosity-driven - and that represents a laminar flow - or inertia-driven - also known as turbulent flow [23]: the difference between the two is determined by the value of the Reynolds number (Re).

2.2.1 Reynolds number

The Navier-Stokes equation for an incompressible newtonian fluid allows the comparison between inertial and viscous forces, and thus indicates whether a flow can be considered laminar or turbulent; from such set of partial differential equation (PDE), the derivation of the Reynolds number (Re) is achievable [7]

$$Re = \frac{U\rho D_h}{\eta}, \tag{2.1}$$

where U is the fluid's characteristic velocity, ρ is the fluid's density, D_h is the channel's hydraulic diameter (defined as $\frac{4A}{P}$) and η is the fluid's dynamic viscosity.

A flow is considered to be laminar when Re is well below 1500, meaning that the viscous forces prevail over the inertial ones [24]; laminarity refers to a flow in which the fluid can be considered as a group of parallel layers sliding on top of each other smoothly, with minimal mixing between them [25]. Laminar flow is required in an IFC setup so that particles do not change position while traveling over the electrodes, causing an alteration of the signal [26]; furthermore, the laminarity of the flow ensures the stability of the electrical read-out [23].

When a suspension of particles is present in the fluid, drag and lift forces may influence their behavior; a new Reynolds number, referred to as particle Reynolds number (Re_p) and and based on Re, defines how viscous and inertial interactions affect particle dynamics [27]. That is given by

$$Re_p = Re\frac{a^2}{D_h^2} = \frac{U\rho a^2}{\eta D_h}, \tag{2.2}$$

where a is the particle diameter. When $Re_p \ll 1$, inertial forces are negligible and the viscous ones prevail. Conversely, particles may be subjected to inertial focusing when $Re_p \sim 1$, meaning that wall and lift forces are responsible for their focusing at specific positions along the cross section of the channel.

In Table 2.1, the two Reynolds number have been calculated for different flow velocities, based on the flow rates employed in this project, for a rectangular channel with a (10×10) µm cross section. Due to the extremely small dimensions of the channels involved, Re is always in the laminar flow regime, i.e. $\ll 1500$, and no inertial forces are expected to affect the particles. Based on the calculated Re and Re_p, the particles are not expected to change position while traveling over the electrodes, preventing any alteration of the signal caused by that. Moreover, the electrical read-out is expected to be stable.

Table 2.1: Re and Re_p for different characteristic velocities, considering $\rho = 1000$ kg/m^3, $\eta = 0.001$ Pa $\cdot$ s, $D_h = 10$ µm and $a = 2$ µm. U is obtained as $\frac{\text{flow rate}}{\text{cross section}}$.

Flow rate [µl/min]	U [m/s]	Re	Re_p
0.01	0.0017	0.017	0.0007
0.05	0.0083	0.083	0.0033
0.10	0.0167	0.167	0.0067
0.50	0.0833	0.833	0.0333
1.00	0.1666	1.666	0.0666
5.00	0.8333	8.333	0.3333

2.2.2 Hydraulic resistance

The hydraulic resistance R_{hyd} is analogous to the resistance of an electrical circuit as it quantifies the opposition of the channel to the flowing of a fluid inside of it. It relates to the flow rate Q and the pressure difference Δp required to have flow through Hagen-Poiseuille law [24]

$$\Delta p = Q R_{hyd} \tag{2.3}$$

Its value is fundamental in determining the correct flow rates to inject into the channels; moreover, thorough considerations on the impact of the channel dimensions on it are necessary for the correct and most convenient design of the trapping sites. For a channel with a rectangular cross section, the hydraulic resistance is given by [24]

$$R_{hyd} = \frac{12\eta L}{1 - 0.63(h/w)} \frac{1}{h^3 w}, \tag{2.4}$$

where η is the fluid dynamic viscosity, L is the channel length, h is the channel height and w is the channel width. A large hydraulic resistance implies that a large pressure difference between inlet and outlet is required in order to have flow: for a (10×10) µm cross section channel filled with water, the hydraulic resistance scales as $R_{hyd} \sim L \cdot 10^{18}$ Pa $\cdot$ s/m^4. All the components of the experimental system must be able to withstand the pressure that such a high resistance demands.

2.2.3 Poiseuille flow

A flow is said to be pressure-driven when the movement of the liquid is enabled by a pressure difference between the two ends of a channel; these type of flows are also known as Poiseuille flows, and they are particularly relevant for the description of liquids in lab-on-a-chip devices [24].

For simplicity, let us consider an infinite parallel-plate channel configuration as sketched in Figure 2.1, where a pressure drop Δp is applied between the two ends.

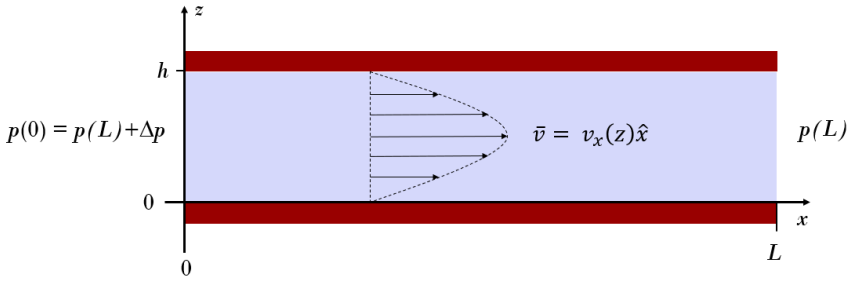

Figure 2.1: Sketch for an infinite parallel-plate channel in the xz-plane: the flow is driven by a pressure difference Δp along the length of the channel L, while translational invariance is valid in the y direction (normal to the plane). The parabolic velocity profile of the flow is represented by a dashed line.

The general Navier-Stokes equation for an incompressible fluid reads as [24]

$$\rho\left[\partial_t \overline{v} + (\overline{v}\cdot\overline{\nabla})\overline{v}\right] - \rho\overline{g} = -\nabla\overline{p} + \eta\nabla^2\overline{v}, \tag{2.5}$$

where ρ is the fluid density, $\overline{v}$ is the fluid velocity, $\overline{g}$ is the gravitational acceleration acting on the fluid and $\overline{p}$ is the considered pressure. With the following hypotheses, suitable for an infinite parallel-plate geometry, it is possible to simplify the non-linear PDE.

- The fluid is in mechanical equilibrium and horizontal, thus the gravitational force can be neglected: $\rho\overline{g} \simeq 0$.
- The flow is parallel and invariant in the x and y directions, hence the only surviving component for the velocity is $\overline{v} = v_x(z)\hat{x}$. Due to a laminar flow, the non-linear term can be neglected: $(\overline{v}\cdot\overline{\nabla})\overline{v} \simeq 0$.
- Steady-state is reached, so $\partial_t\overline{v} = 0$.

By applying the above consideration to Equation 2.5, the left-hand side can be completely disregarded and the remaining equation is easily solved for the velocity by integrating twice and applying no-slip boundary conditions ($v_x(0) = v_x(h) = 0$). This procedure results in a simple parabolic velocity profile

$$v_x(z) = \frac{\Delta p}{2\eta L}(h - z)z, \tag{2.6}$$

an outline of which is visible in Figure 2.1.

If two more walls are added so that a rectangular cross section is achieved, more boundary conditions should be taken into consideration; a complete derivation of the velocity profile for the aforementioned scenario can be found in the book *Theoretical Microfluidics* written by H. Bruus, which illustrates how the results are in agreement with Equation 2.6. The calculations yield that the maximum velocity is reached in the middle of the channel, while it is the lowest when in contact with any of the walls.

When the length of a rectangular channel is much longer than the characteristic dimension of its cross section, the infinite parallel-plate configuration is a good enough approximation to describe the dynamics of the system [24]; that happens to be the case of the microfluidic channels involved in this thesis, hence the parabolic velocity profile will affect the traveling speed of the particles depending on their position in the channel. A particle in the middle of the channel will travel faster than one close to a wall, therefore additional caution must be adopted when analyzing experimental data.

The aforementioned notions on microfluidics will be crucial in understanding the information that impedance flow cytometry can yield.

2.3 Impedance flow cytometry

As mentioned in Chapter 1, impedance flow cytometry (IFC) is a label-free electrical characterization technique that involves electrodes patterned in a microfluidic channel. Its principle of operation will be detailed in the upcoming Subsection.

2.3.1 Working principle

The condition for IFC is rather simple, as it merely requires the presence of a microfluidic channel patterned with electrodes that generate an alternating electric field. Let us consider a generic particle traveling through a simple straight channel with three coplanar electrodes on the bottom wall, as displayed in Figure 2.2: an AC voltage is applied to the middle electrode, while the output current is recorded by the outer ones. It is customary to consider the response of the system as the differential current, which results in a few advantages, including mitigation of common-mode effect, minimization of crosstalk and higher SNR for the same applied voltage [28]. When the particle has not reached the area covered by the electrodes yet, the signal registered by the outer ones is the same and so the differential current is zero (Figure 2.2a). As time goes by, the particle begins to enter the area covered by the first electric field, which undergoes a perturbation that is reflected on the current registered at the first electrode; the second electric field remains unchanged, and this gives rise to a change in the differential current, which reaches a maximum when the particle is exactly in between the first two electrodes (Figure 2.2b). Then, the signal starts to decrease as the particle flows further and it is zero again when the travelling object is exactly above the middle point of the second electrode, where the field are equally perturbed (Figure 2.2c). The exact same progression unrolls as the particle moves ahead, but this time the signal has opposite sign (Figure 2.2d); the differential current returns to zero when the area covered by electrodes is left behind (Figure 2.2e). In light of this, the overall registered signal for a travelling particle is the succession of two peaks with opposite sign in a background that would be zero otherwise: from now on, this peculiar shape will be referred to as a bipolar double Gaussian.

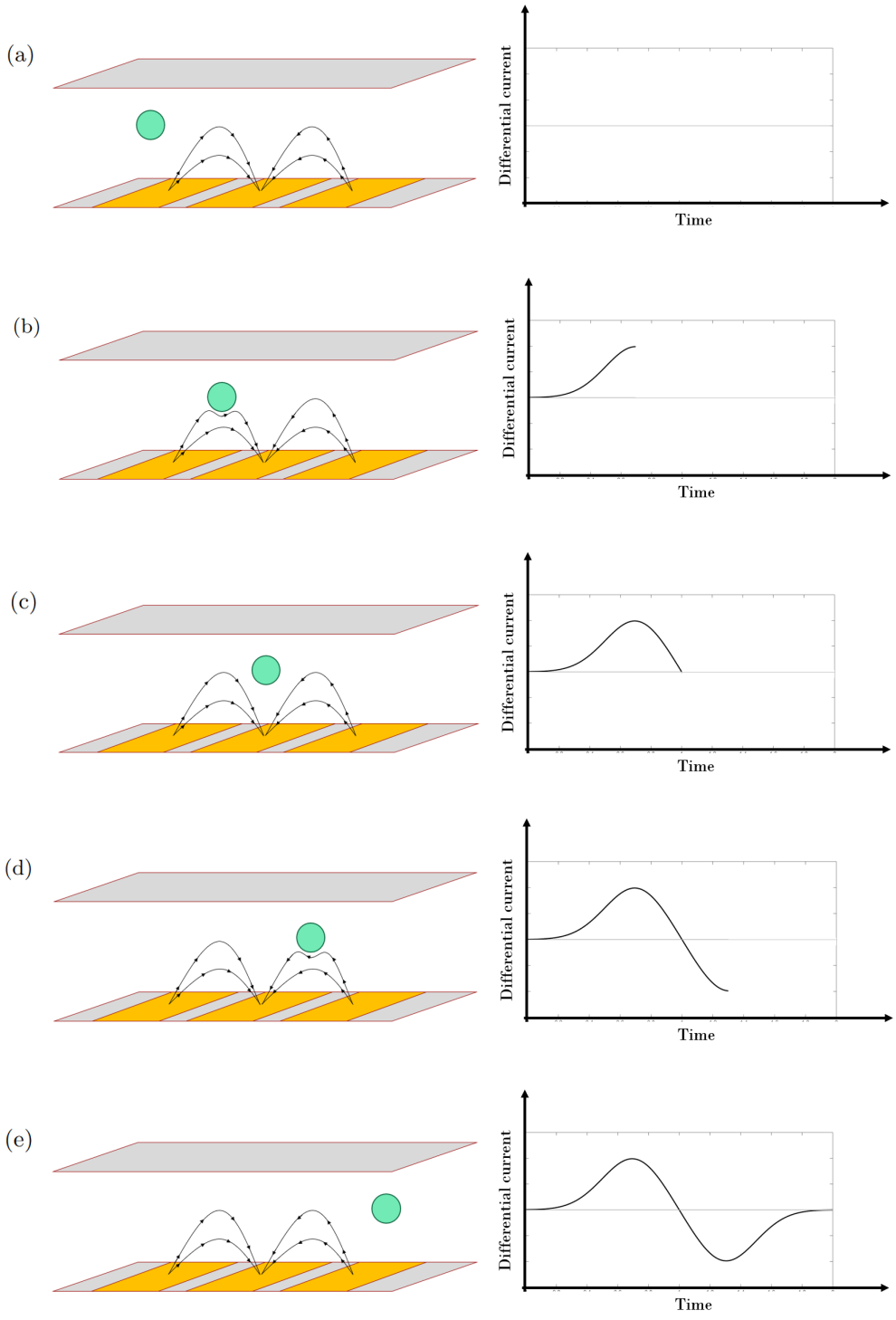

Figure 2.2: IFC working principle: the differential current is zero when the particle is outside the area of influence of the electric fields generated by the electrodes (a-c-e), while it reaches a peak when the object is exactly in between them (b-d). This behavior gives rise to a bipolar double Gaussian as the particle moves along the channel in the direction of the flow.

The characteristics of the complete curve representing a transition (Figure 2.2e, right), such as amplitude of the peaks and total time required for the transition, are related to the dielectric properties and dimensions of the individual particle; it is possible to model the impedance response of a single cell in a microfluidic cytometer with an equivalent circuit model, which allows to draw the same conclusions as the ones derived with the more complex Maxwell Garnett mixing formula [29]. An overview of the mathematical model can be found in Appendix A, while subsection 2.3.4 will focus on the circuital model.

In the following, the most common electrode configurations for IFC are presented.

2.3.2 Electrode configurations

Historically, two main configurations of electrodes have been employed in IFC setups: front-facing electrodes and coplanar electrodes, as shown in Figure 2.3. Both designs are characterized by their own advantages and disadvantages.

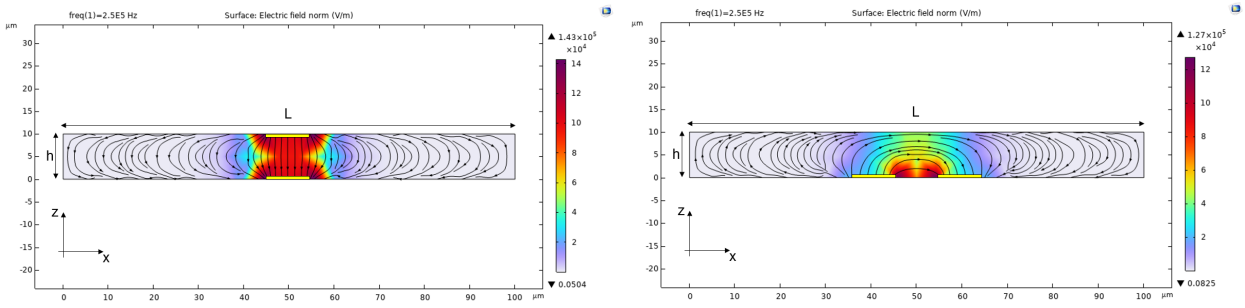

(a) Front facing electrodes.

(b) Coplanar electrodes.

Figure 2.3: Typical electrode configurations for IFC. For better visibility, the yellow electrodes have been drawn out-of-plane. The black lines represent the electric field lines for front facing (a) and coplanar (b) layout. The overlaid color maps show the strength of the field.

The front-facing configuration consists of electrodes patterned on two opposite walls, but the principle of operation is similar to that described previously for a coplanar configuration. It benefits from a fairly homogeneous distribution of the electric field along the height of the channel, making the recorded signal independent on the particle position. However, when a second pair of electrodes is added to register the differential signal, crosstalk due to fringing effects between the two pair of electrodes is higher with respect to the coplanar layout, affecting the noise in the signal and the sensitivity of the system as a consequence. Moreover, fabrication is much more challenging, as it requires the precise alignment of the two pair of electrodes on top of each other.

Conversely, no alignment is required in the manufacturing process for the coplanar configuration and crosstalk is reduced. The main disadvantage for such layout is the non-uniformity of the electric field; the complete derivation for its expression requires complex integration techniques and it is not straightforward due to the finite dimensions of the electrodes. Nevertheless, its magnitude will be maximum close to the electrodes at the bottom of

the channel, and it will decrease going up towards the top wall. The potential consequences on the ability of the system to differentiate particles is evident: a small particle travelling at the bottom of the channel may yield the same response as a bigger one travelling at the top.

The electric field considerations are supported by data simulated with COMSOL: in Figure 2.3a and Figure 2.3b respectively, front facing and coplanar electrodes are juxtaposed. An AC signal at 250 kHz is applied to the two layouts made of 10 µm-wide electrodes, which are set in a (100 × 10) µm channel. In black, the streamlines for the electric field show that, in the first case, the direction does not vary in the area covered by the electrodes, while, in the second case, the field is not uniform in the same region. The attached color map demonstrates that in Figure 2.3a the magnitude of the electric field does not undergo significant variations along the height of the channel h. On the contrary, it decreases in the z-direction in Figure 2.3b.

To quantify how the variation in electric field affects the signal in IFC, a spherical particle with radius 3 µm has been added to the geometries being examined (Figure 2.4): its center is identified by the coordinates (xc,zc), and xc has been fixed in between the electrodes at $\frac{L}{2}$ (L being the length of the channel), while a parametric sweep of zc has been performed from 3.5 to 6.5 µm.

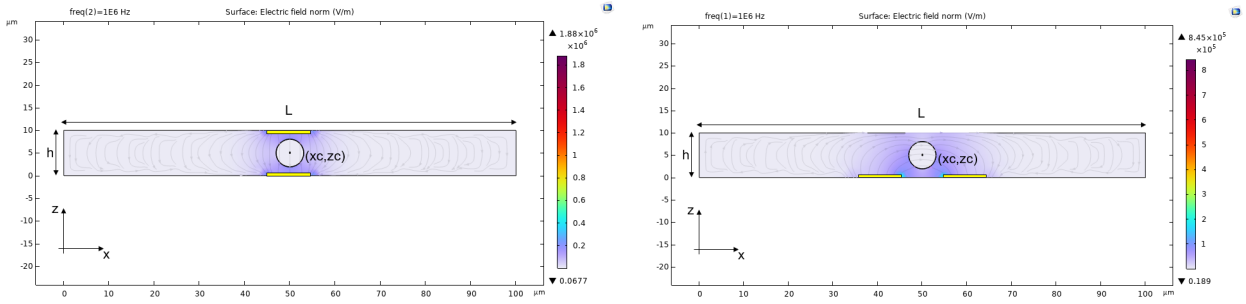

(a) Front facing electrodes.

(b) Coplanar electrodes.

Figure 2.4: Spherical particle in between front facing (a) and coplanar (b) electrodes. The center of the particle is identified by the coordinates (xc,zc).

A voltage of 1 V is applied to one of the electrodes in each configuration, while the current is recorded on the remaining one; for a frequency of 1 MHz, the variation in current magnitude I has been plotted on MATLAB as function of the zc sweep, where $I\left(zc = \frac{h}{2} = 5\ \mu\text{m}\right)$ is the reference value.

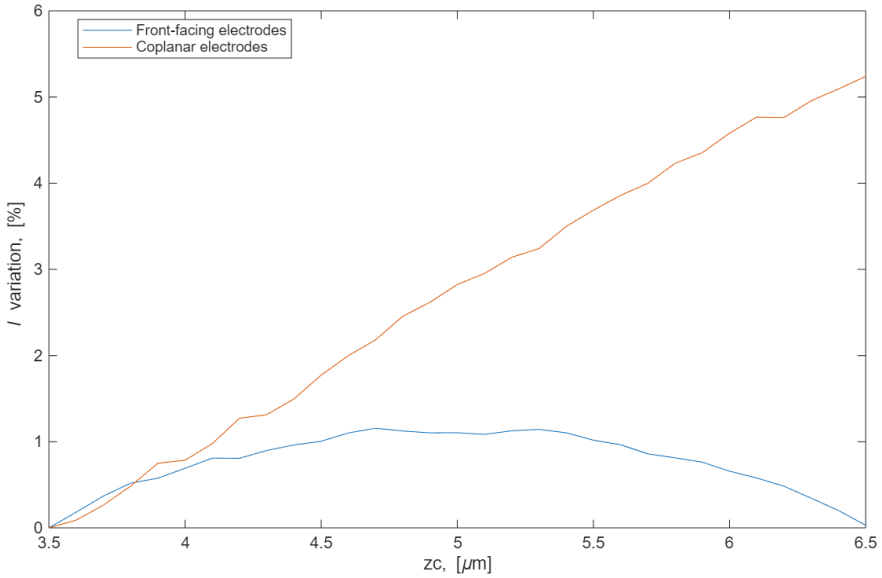

Figure 2.5: Current variation as function of zc for front facing (blue curve) and coplanar (red curve) electrodes.

It can be observed in Figure 2.5 that, for the front facing configuration, the current variation is maximum for $zc = 5$ µm, but it is never greater than 1% in any case. On the contrary, for coplanar electrodes, the current variation increases steadily for growing zc. The signal response in the latter case is heavily dependent on zc.

The focus in Chapter 3 will be the mitigation of this effect in the coplanar configuration, with the objective of finding a parameter that can yield information on the coordinate zc of the particle in the channel; that is the starting point for the development of a strategy to correct such unwanted effect.

2.3.3 General structure of bacteria

In order to create a model to understand the electrical response of bacteria in an IFC setup, it is convenient to have a general knowledge of their structure. Bacteria can have many different shape and sizes [30]. *E. coli* are Gram-negative bacteria, with a rod-like shape typically in between 1-3 µm in length and 0.5 µm in diameter. They are one of the main bacterial species in the intestines of mammals. Usually they are non-pathogenic and they can be easily grown in laboratory, but some strains are harmful to humans [31]. All bacteria share some common features: DNA is not enclosed in a nucleus and it occupies the center of the cell, which is called cytoplasm and is highly conductive. The cytoplasm resides inside an isolating membrane that is usually made of many different layers. Its movement is enabled by thin flagella. A sketch of a bacterium is showed in Figure 2.6.

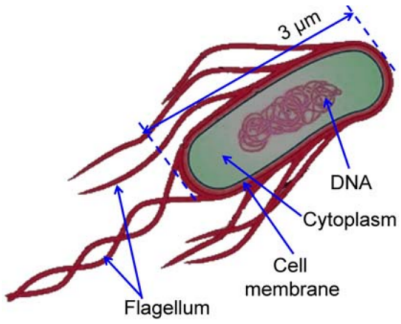

Figure 2.6: Sketch of a bacterium [31].

Due to its structure and its electrical properties, it is a fair approximation to model a bacterium as a single-shelled particle with a conductive core and an isolating membrane. This is what will be done in the following in order to illustrate an equivalent circuit model for IFC.

2.3.4 Equivalent circuit model

An equivalent circuit model (ECM) can be employed to simplify the analysis of the impedance response, on account of the fact that all the electrical characteristic of the original circuit are retained. The equivalent circuit is designed with basic electrical components such as resistors and capacitors, and the model assumes that the complex conductivities and permittivities of the system can be substituted by them [23]. Let us consider a shelled particle representing a bacterium, made of a conductive core (cytoplasm) surrounded by an isolating shell (membrane), immersed in an electrolyte above two coplanar electrodes; an ECM for this system is displayed in Figure 2.7.

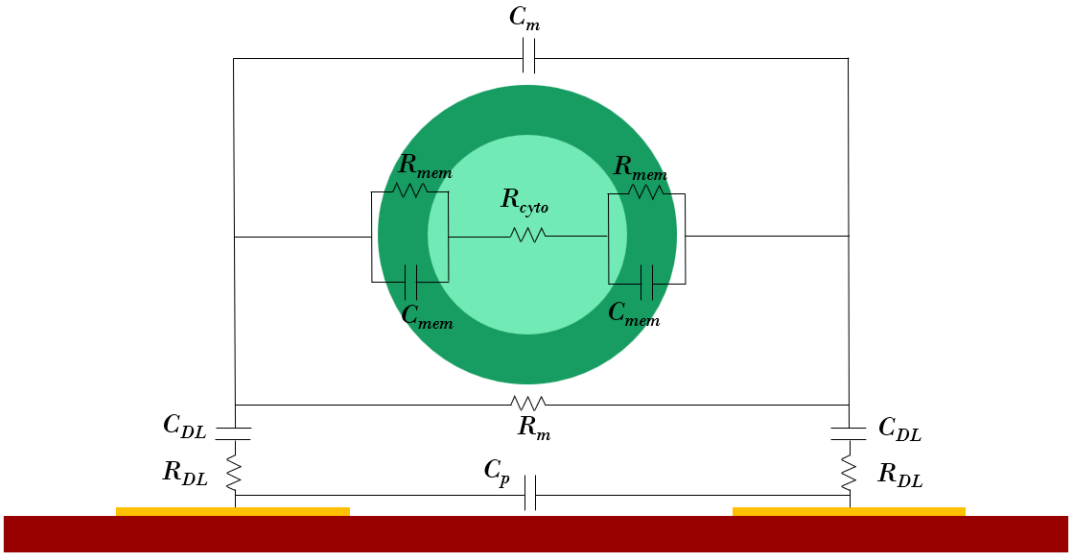

Figure 2.7: ECM for a shelled particle on top of two coplanar electrodes.

For this model, the components displayed are the double layer resistance R_{DL} and the double layer capacitance C_{DL}, the parasitic capacitance C_p, the resistance R_m and the capacitance C_m of the medium in which the particle is immersed: those are the intrinsic characteristic of the system. Due to the presence of the particle, it is necessary to add the resistance and the capacitance of the membrane, R_{mem} and C_{mem} respectively, and the resistance of the cytoplasm R_{cyto}.

Assuming that an alternating current with angular frequency ω is applied to the system and remembering the j represents the imaginary unit, a break down of the electrical double layer impedance Z_{DL}, the parasitic impedance Z_p, the medium impedance Z_m and the particle impedance Z_{ptc} respectively is explored in the following paragraphs.

Electrical double layer impedance When a metal is immersed in an electrolyte solution, the electrical charges at the interface tend to rearrange due to the arising of a potential difference; positive ions in the solution are attracted by electrons in the metal, generating an accumulation of charge that is known as electrical double layer (EDL) [32]. It is possible to distinguish two main sublayers: closest to the metal is the so-called *Stern layer*, which contains species that are specifically adsorbed, while towards the bulk of the solution long-range electrostatic forces are involved and a *diffuse layer* of nonspecifically adsorbed particles can be identified.
The relationship between the potential Φ generated by the EDL and the distance r from the electrode can be mathematically represented by a function that decreases linearly at the very beginning of the Stern layer and then decays exponentially as r increases [33] (Figure 2.8).

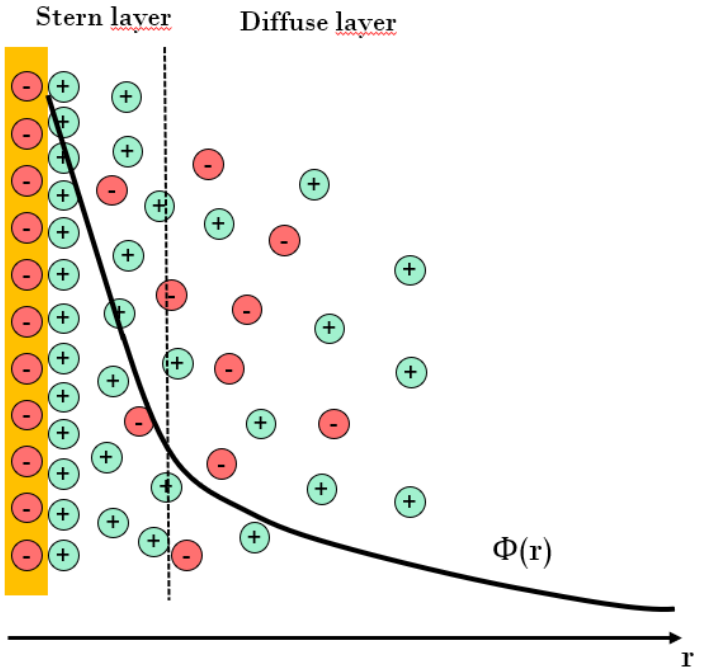

Figure 2.8: EDL at the interface between electrolyte solution and electrode (yellow). The potential $\Phi(r)$, decreasing at first linearly and then exponentially, is overlaid on the sketch.

The separation of charges in an EDL is reflected as a capacitance in terms on electrical components; to represent the whole system, it needs to be connected in series with a resistance simulating the electrolyte [34]. Consequently, the impedance Z_{DL} corresponding to the EDL is given by

$$Z_{DL} = \frac{1}{j\omega C_{DL}} + R_{DL} \tag{2.7}$$

Parasitic impedance When handling electrical circuits, a parasitic capacitance must always be taken into consideration. Its name arises from the fact that it is unwanted and not part of the ideal design of the circuit; it arises from wiring, interconnections between components and merely the fact that such elements are placed inevitably in close proximity [35]. The parasitic impedance Z_p is given by

$$Z_p = \frac{1}{j\omega C_p} \tag{2.8}$$

Medium impedance In the ECM shown in Figure 2.7, the medium is represented by a capacitor connected in parallel with a resistor; following the laws of circuit theory, the calculation for the total medium impedance Z_m is straightforward, hence

$$Z_m = \frac{R_m \frac{1}{j\omega C_m}}{R_m + \frac{1}{j\omega C_m}} = \frac{R_m}{1 + j\omega C_m R_m} \tag{2.9}$$

It is to be noted that C_m is only relevant at high frequencies, therefore it can be neglected completely in most cases [23]; for completeness, it is taken into account in the present model.

Particle impedance In principle, in an ECM the parallel of a capacitor and a resistor should be assigned to each layer of a particle; however, it is possible to notice from Figure 2.7 that the capacitor for the core of the particle under analysis has been ignored. That is due to the fact that biological particles such as bacteria tend to have a highly conductive cytoplasm (440 mS/m for *E. coli* [36]), thus the associated capacitance can be neglected. The expression for the total impedance Z_{ptc} of the remaining components simulating the particle is

$$Z_{ptc} = R_{cyto} + \left(\frac{1}{R_{mem}} + j\omega C_{mem} \right)^{-1} \tag{2.10}$$

Before deriving the total impedance of the system in Figure 2.7, it is now convenient to go through some frequency considerations in order to simplify the model. Let us pretend for a moment that no particle is present: the frequency response of the system where only Z_{DL}, Z_p and Z_m are present is shown in Figure 2.9. The curve is obtained by inserting Equation 2.7, Equation 2.8 and Equation 2.9 into the equation for the total impedance of the channel, given by Equation 2.11.

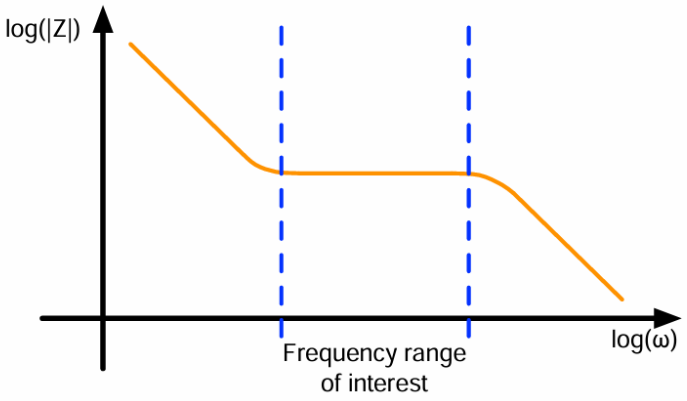

Figure 2.9: Frequency response for a channel patterned with electrodes and filled with an electrolyte solution, obtained from Equation 2.11. The frequency range of interest is highlighted. Taken from [23].

$$Z_{ch} = \left(\frac{1}{Z_p} + \frac{1}{Z_{DL} + Z_m} \right)^{-1} \tag{2.11}$$

When the frequency is low, the impedance response is governed by the effect of Z_{DL}; as ω is increased, the EDL capacitance is short circuited and the signal reaches a flat area, so that a variation in frequency does not yield any change in impedance response. At high frequencies, the signal is dominated by C_p and C_m. When performing analysis on particles, it is desirable for the signal to be affected only by the electrical properties of the sample; this can be achieved in the flat area of the graph, denominated *frequency range of interest* and highlighted in Figure 2.9. By choosing to operate at frequencies in such range, which can be defined experimentally with a frequency sweep, the influence of Z_{DL} and Z_p can be avoided.

Now let us go back to the setting depicted in Figure 2.7 and assume to be working in the frequency range of interest: the only relevant impedances remaining are Z_m and Z_{ptc}. The total impedance Z_{tot} in this simplified scenario is given by the parallel of the two, which can be derived by combining Equation 2.9 and Equation 2.10

$$Z_{tot} = \frac{Z_m Z_{ptc}}{Z_m + Z_{ptc}} = \frac{R_m \left(\left(\frac{1}{R_{mem}} + j\omega C_{mem} \right)^{-1} + R_{cyto} \right)}{R_m + (R_m j\omega C_m + 1) \left(\frac{1}{R_{mem}} + j\omega C_{mem} \right)^{-1} + R_{cyto} (R_m j\omega C_m + 1)} \tag{2.12}$$

Knowing the physical parameters relating to resistance and capacitance of the particle and of the medium, the expected impedance response for the system can be simulated and species can be differentiated.

Non-uniformity of electric field The non-uniformity of the electric field intrinsic to the coplanar electrode configuration involved in the project has not been addressed so far in the

ECM. Nevertheless, it is worth mentioning that this will cause an error in the derived values of the electrical components, which should be corrected with a conformal mapping of the electric field. This method will yield a cell constant κ to take the non-uniformity of the field into account; the new parameter can be exploited to calculate resistance and capacitance of a simple microfluidic channel filled with a medium as [37]

$$R = \frac{1}{\sigma}\frac{\kappa}{l}, \quad C = \epsilon_0 \epsilon_r \frac{l}{\kappa}, \tag{2.13}$$

where σ is the conductivity of the medium, l is the width of the channel, ϵ_0 is the vacuum permittivity and ϵ_r is the relative permittivity.
When a suspension of particles is present in the channel, the association between physical and electrical model is cumbersome and requires several considerations, therefore it is beyond the scope of this work; a description of it can be found in the Master thesis *Using impedance spectroscopy for antibiotic susceptibility testing* written by C. Bertelsen.

Chapter 3

Electrode optimization: FEM analysis

In this Chapter, the optimization process for three electrodes in a coplanar configuration is outlined. The traveling particle chosen for testing is a simple polystyrene bead for all FEM simulations, which have been performed with the software COMSOL Multiphysics 6.3. At first, the dependence of the signal in a simple layout with identical electrodes is verified. Then, asymmetry is implemented in the design, starting from modifying the width of the electrodes and concluding with assessing the effect of having non-identical gaps between them. The data from all simulations is exported and plotted on OriginPro 2024b, while further analysis is performed on MATLAB R2025a.

Finite element method (FEM) is a popular technique employed to simplify engineering problems, as it allows to solve differential equations numerically by breaking down complex systems into smaller elements. Space is discretized by means of a mesh, that is a numerical domain for the solution of PDEs in which a finite number of points is contained. COMSOL permits the application of such approach through numerical simulations, which are going to be detailed throughout this Chapter.

The geometry of the system with the name of the variables that will be referenced in the following is displayed in Figure 3.1. The channel consists of a simple straight canal with square cross section, while the bead is spherical and has radius r; the coordinates of its center point are (xc, yc, zc). Three coplanar electrodes, identified by numbers 1, 2 and 3, are placed on the bottom of the channel, at $z = 0$ µm.

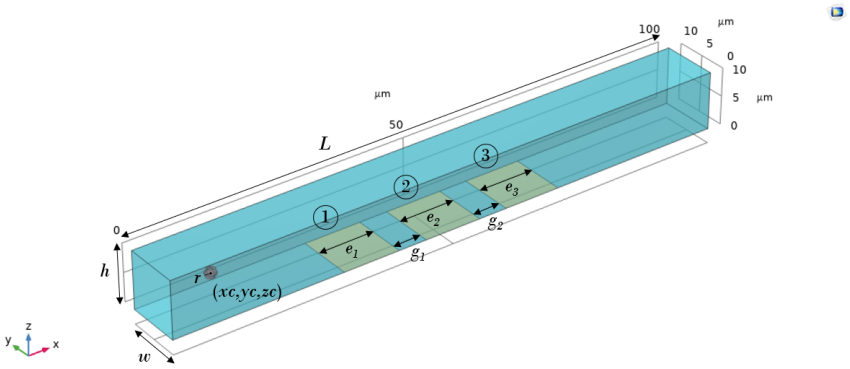

Figure 3.1: Geometrical description of the simulated system. It is to be considered as a reference for all the subsequent simulations.

The material for the channel is set to *Water* from COMSOL libraries; in order to reproduce the medium that will be employed for experimental data acquisition,i.e. a diluted PBS solution, the electrical conductivity σ_m and the relative permittivity ϵ_m are selected manually. Likewise, the bead is made of *Polystyrene [solid]* from the same database, with conductivity σ_b and permittivity ϵ_b.

The only physics involved is *Electric Currents*: electrode 1 and electrode 3 are terminals with 0 V applied, where two boundary probes for the terminal currents are placed, while electrode 2 is a terminal with an applied voltage V. The output of the simulations is taken as the differential current I_{diff} defined as

$$I_{diff} = \mathrm{Re}(I_1) - \mathrm{Re}(I_3), \tag{3.1}$$

where I_1 and I_3 are the currents at electrode 1 and 3, respectively. The *Study* in COMSOL involves a *Parametric Sweep* and a *Frequency Domain* step with frequency f.

The parameters given in Table 3.1 are used for all subsequent simulations unless otherwise stated.

Table 3.1: Common conditions for all simulations: (a) geometrical parameters, (b) physical properties and (c) electrical parameters of the system.

L	w	h
100 μm	10 μm	10 μm

(a)

σ_b	ϵ_b	σ_m	ϵ_m
1×10^{-13} mS/m	2.5	80 mS/m	80

(b)

V	f
3 V	250 kHz

(c)

In the following, the main objectives will be the maximization of I_{diff} and the minimization of its dependence on zc.

3.1 Three symmetric coplanar electrodes

As a first approach, a symmetric configuration of electrodes like the one seen in Figure 3.1 is investigated. Particle radius, electrode width and electrode gap specific to the simulation are collected in Table 3.2.

Table 3.2: Geometrical characteristic for a first analysis of a three-symmetric-electrode configuration.

r	$e_1 = e_2 = e_3$	$g_1 = g_2$
1 µm	10 µm	5 µm

Before assessing the influence of the particle position on the output signal, mesh considerations are necessary in order to determine the correct element size allowing for a reasonable trade-off between computational time and the yielded accuracy.

3.1.1 Mesh optimization

Besides providing a general *Physics-controlled mesh*, COMSOL allows the user to implement their own custom mesh by choosing the size of the elements in each domain of the geometry. Bigger elements correspond to faster computational time, but, at the same time, the best accuracy is obtained for smaller elements. Therefore, a compromise between the two is necessary. Considering that the most critical region for FEM analysis is the one of the electrodes, adjustments are needed to the mesh generated by the software, which can be exploited as a starting point.

The general mesh, calibrated for fluid dynamics, consists of free tetrahedral elements and it is finer in the domain of the bead and on the electrodes. The influence of the *Maximum element size* in the electrode domains on I_{diff} has been investigated by means of a parametric sweep from 0.1 µm to 0.7 µm, with a step of 0.01 µm; the resulting plot is showed in Figure 3.2. For this simulation, the bead was fixed in between electrode 1 and 2 ($xc = 42.5$ µm) and in the middle of the channel ($yc = zc = 5$ µm), resulting in a non-zero differential current.

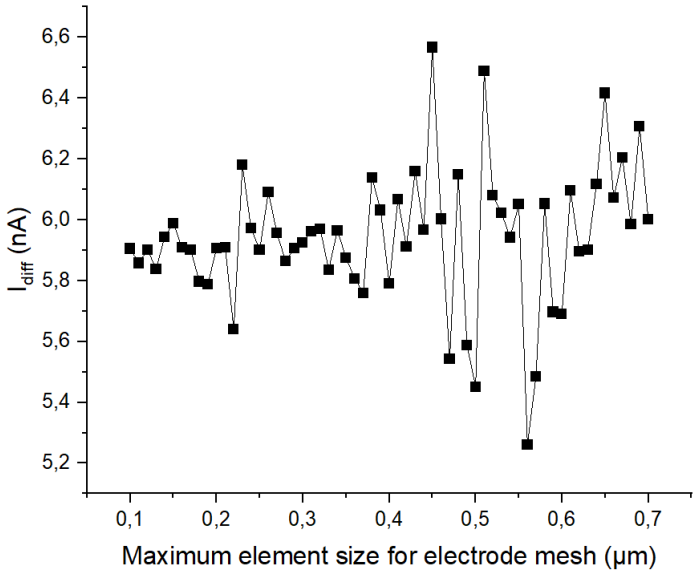

Figure 3.2: Dependence of I_{diff} on the maximum element size for the electrode mesh.

Taking a look at the graph, it is possible to notice that the current fluctuations are irregular and never really seem to stabilize completely. However, the signal appears less noisy when the maximum element size for the electrode mesh is smaller than 0.4 μm: that is supported by a standard deviation of 0.11 nA in the range $(0.1 - 0.4)$ μm, as opposed to 0.30 nA for values bigger than 0.4 μm. It means that, in this range, the size of the mesh will have the smallest impact on I_{diff}, which is desirable to preserve accuracy. As a consequence, the optimal value lies in the mentioned range, but taking a value on the lower end would make the computation extremely time-consuming; that is the reason why 0.35 μm is the settled upon choice for the maximum element size of the electrode mesh. Such value will be maintained in all the simulations performed in the project.

The remaining element sizes were not modified with respect to the ones provided by COMSOL. The final complete mesh is depicted in Figure 3.3 and consists of 746152 domain elements, 31250 boundary elements and 1166 edge elements. At these settings, all simulations had a runtime between 0.5 and 4 hours.

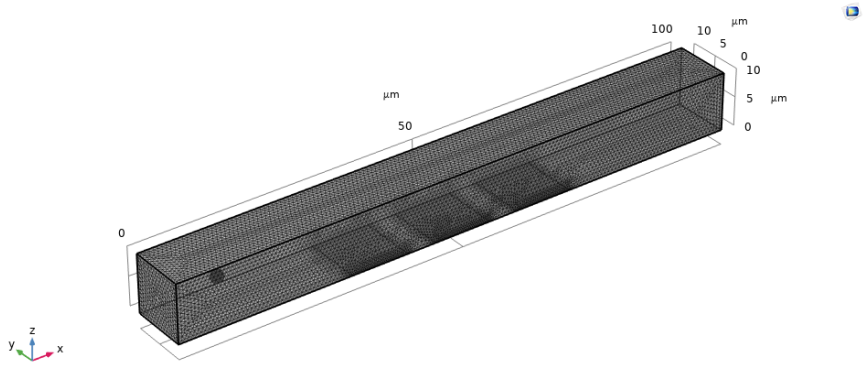

Figure 3.3: Final mesh for a channel with three coplanar electrodes and a spherical bead.

It is worth mentioning that Figure 3.2 only provides an indication of the effect of the mesh on the output signal. In subsequent simulations, where the bead is swept across different positions, the mesh dynamically adapts and morphs around the particle, undergoing local changes. As such, the conclusions drawn from the mesh analysis should not be regarded as universally applicable, but rather as a guideline for the protraction of the study.

3.1.2 xc sweep

As a first approach to visualize the expected simulation outcomes and get a sense of the anticipated data for IFC analysis, the bead was moved along the length of the channel in order to emulate flowing: with reference to Figure 3.1, the particle was in the center of the cross section of the channel ($yc = zc = 5$ µm) and xc was swept from 0 µm to 100 µm. Then, the data was extracted from COMSOL and fitted using the *Multiple Peak Fit* tool of OriginPro with *Gauss* function [38]

$$y = y_0 + \frac{A}{w\sqrt{\pi/2}} e^{-2\frac{(x-x_c)^2}{w^2}}, \tag{3.2}$$

where $y = I_{diff}$ and $x = xc$ in this case.

The final plot for I_{diff} as a function of the swept parameter xc is shown in Figure 3.4a. As predicted in subsection 2.3.1, a bipolar double Gaussian is obtained; the quality of the fitting, characterized by the statistical parameter R^2, is sufficiently high to assert that the adopted method is reliable for the quantitative extrapolation of information from the curve.

In view of that, the dependence of the output signal on zc was investigated. The same sweep of xc that has just been described was performed again for different height positions of the particle in the channel. The resulting bipolar double Gaussians are overlaid in Figure 3.4b, where it is possible to notice that the magnitude of the peaks decreases as the bead moves further away from the electrodes. The result is in agreement with the theoretical discussion in subsection 2.3.2.

By taking as a reference the bead at $zc = 5$ µm, the magnitude of positive and negative peaks in Figure 3.4b provided by OriginPro was annotated, and the percentage variation from the reference was calculated: a plot of its behavior is presented in Figure 3.5. No

difference between positive and negative peak was observed, hence the curve for negative peaks is omitted. The graph highlights and quantifies the dependence of the output signal on zc, which is analyzed further in the upcoming subsection.

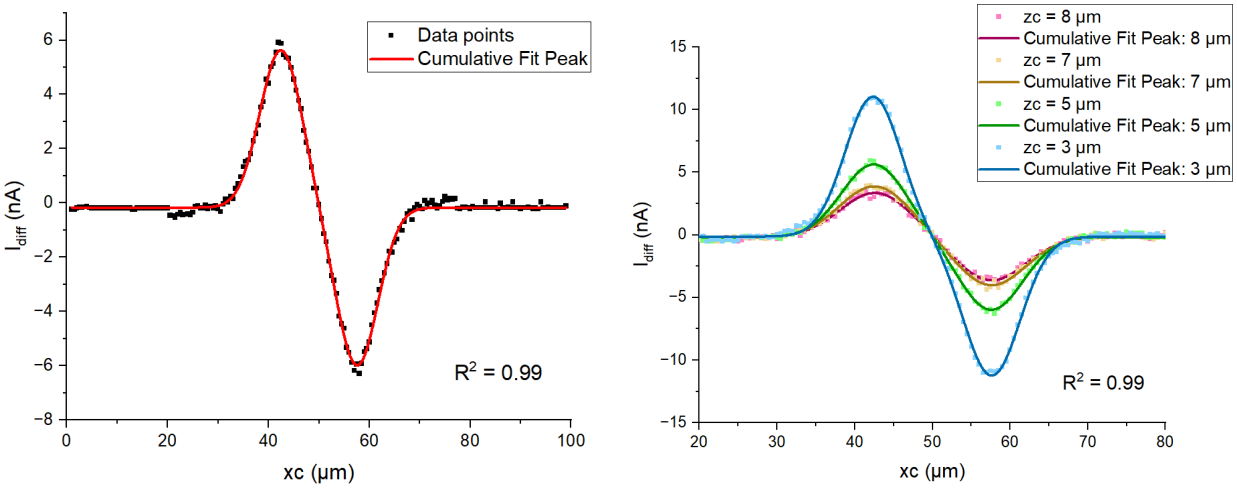

(a) (b)

Figure 3.4: I_{diff} as a function of xc in a symmetric three-coplanar-electrode configuration for various position of the bead in the cross section of the channel. (a) $yc = zc = 5$ µm: the typical double Gaussian curve of IFC is evident and $R^2 = 0.99$. (b) $yc = 5$ µm, while zc assumes various values (3 µm, 5 µm, 7 µm, 8 µm): $R^2 = 0.99$ in all cases.

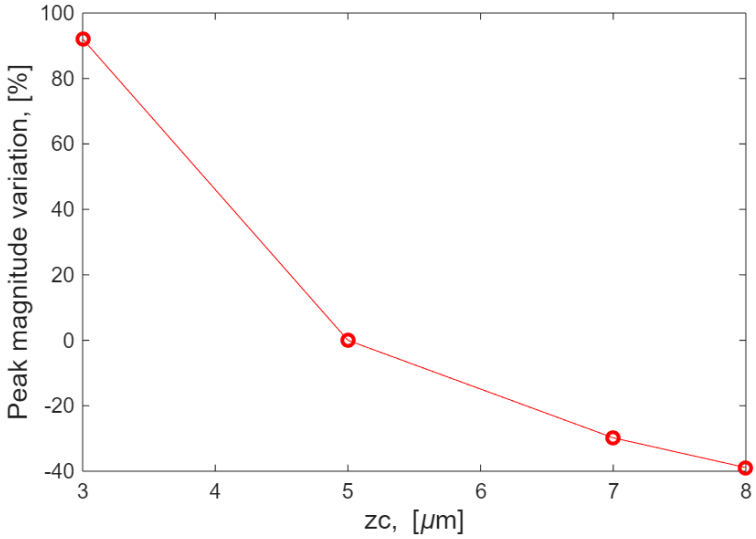

Figure 3.5: Percentage variation of positive peak magnitude as a function of zc for a symmetric three-coplanar-electrode configuration.

3.1.3 zc sweep

To proceed with the analysis, the bead was pinned in the middle of the gap between electrode 1 and 2, and a sweep of zc was executed: the expected behavior of I_{diff} is decreasing for increasing zc, but data has been been fitted on OriginPro once again to assess the type of dependence between the two variables. The most suitable function turned out to be a decreasing exponential (*ExpDec1* [39]), for which the quality of the fitting was very high ($R^2 = 0.99$) in all the considered situations; the resemblance with Figure 3.5 is noticeable in Figure 3.6.

To take a step further, the same parametric sweep was repeated for several values of $e_1 = e_2 = e_3$, in order to evaluate the most convenient width for the electrodes. The outcomes of the simulations are plotted in Figure 3.6.

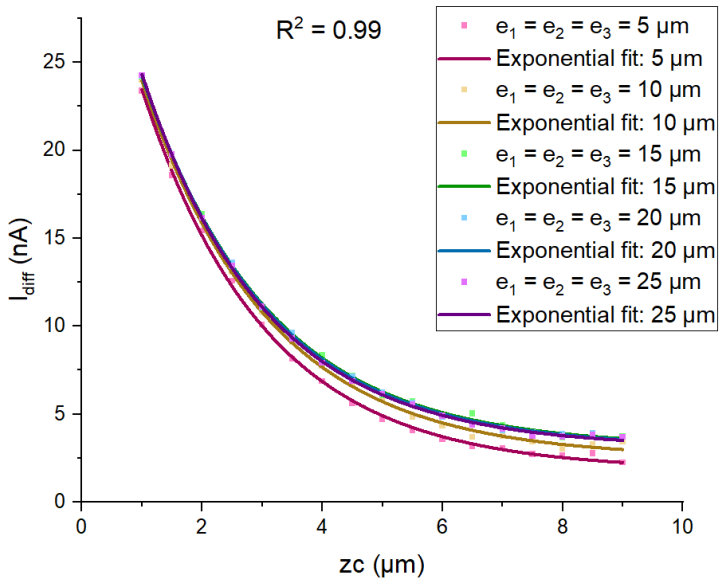

Figure 3.6: Simulated I_{diff} as a function of zc in a symmetric three-coplanar-electrode configuration for different values of electrode width (5 µm, 10 µm, 15 µm, 20 µm, 25 µm).

Although the curves being very similar, by taking a closer look it emerges that the wider the electrode, the smaller the current range. To have the smallest variation in current when zc changes, the electrode should be as wide as possible. However, the change in range fro electrodes above 10 µm is not significant, therefore 10 µm will be used for cleanroom fabrication and further simulations.

A similar process of thought was followed for the selection of the optimal gap: the same zc sweep was performed for multiple values of $g_1 = g_2$, while $e_1 = e_2 = e_3$ were fixed and equal to 10 µm. The results are displayed in Figure 3.7, where the simulated data has been fitted with the previously mentioned exponential function. It is possible to notice that the I_{diff} range is smaller when the gap is the biggest; however, even if still being high ($R^2 > 0.84$ for all curves), the accuracy of the fitting has an opposite trend, making the results less reliable. Moreover, a larger gap gives an overall smaller current, which is an issue

due to the expected noise in the system for experimental acquisition. As a consequence, the most suitable gap was deemed to be the 5-µm-wide one.

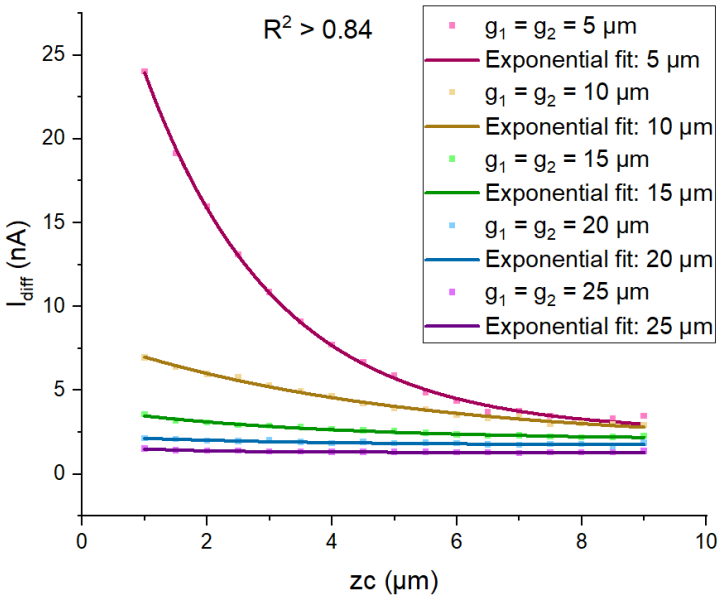

Figure 3.7: I_{diff} as a function of zc in a symmetric three-coplanar-electrode configuration for different values of electrode gap (5 µm, 10 µm, 15 µm, 20 µm, 25 µm).

3.1.4 $e_1 = e_2 = e_3$ and $g_1 = g_2$ sweep

The next step was to determine if the best electrode parameters defined with a zc sweep are a sensible choice by means of a sweep of $e_1 = e_2 = e_3$ firstly and $g_1 = g_2$ secondly. The bead was fixed in between electrode 1 and 2 along the length of the channel, with $yc = zc = 5$ µm.

A sweep of $e_1 = e_2 = e_3$ was performed from 2.5 µm to 30 µm for a gap of 5 µm, then the extracted data was fitted on OriginPro with the exponential function *ExpGro1* [40], as seen in Figure 3.8a. The signal appears noisy as the width increases, but a clear trend is discernible: for $e_1 = e_2 = e_3 > 10$ µm, I_{diff} tends to stabilize and the dependence on the swept parameter fades away. Furthermore, the current is maximum in the same range, which is desirable as it is more easily detectable by instrumentation. Because of this, 10 µm is confirmed to be a reasonable value for the width of the electrodes.

The width of the gaps was investigated as well: for the bead being in the same position as the previous simulation and keeping the electrodes at 10 µm, a sweep of $g_1 = g_2$ was conducted from 2.5 µm to 30 µm. The exponential function *ExpDec1* [39] was used to fit the data, and the resulting plot is exhibited in Figure 3.8b. The maximum current is observed for the smaller gaps; however, to avoid fabrication issues, 5 µm is a logical choice for $g_1 = g_2$.

The results obtained from the simulations where the electrode characteristics are swept are in good agreement with those in subsection 3.1.3, where zc was the variable subjected to a sweeping.

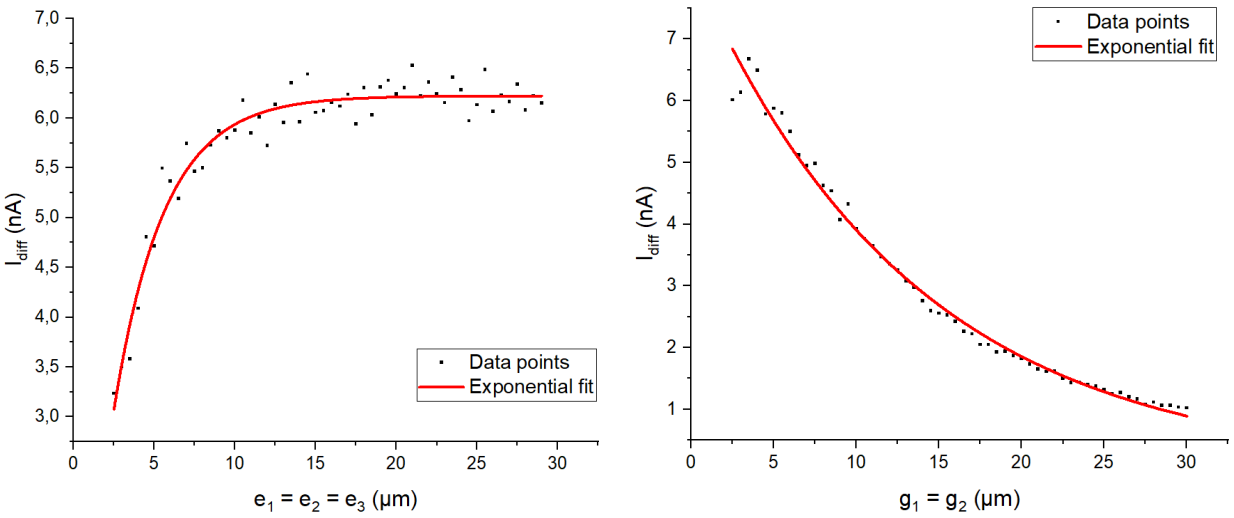

(a) (b)

Figure 3.8: I_{diff} as a function of the electrode characteristics: (a) the width of the electrodes is changed, (b) the gap between the electrodes is changed.

3.2 Three asymmetric coplanar electrodes: changing widths

The simple layout defined previously can be considered as the starting geometry for all the subsequent simulations; the first modifications applied to it consists in asymmetry in the widths of the electrodes. The objective is to identify in the results any characteristics that can yield information on the position zc of the bead, so that a compensation strategy can be developed; to be significant enough, such characteristics also needs to be independent of the size of the particle.

Both variations in e_3, which has zero voltage applied, and e_2, to which 3 V are supplied, were implemented.

3.2.1 Variation of e_3

For better visualization, the limits of the range into which e_3 was modified are showed in Figure 3.9.

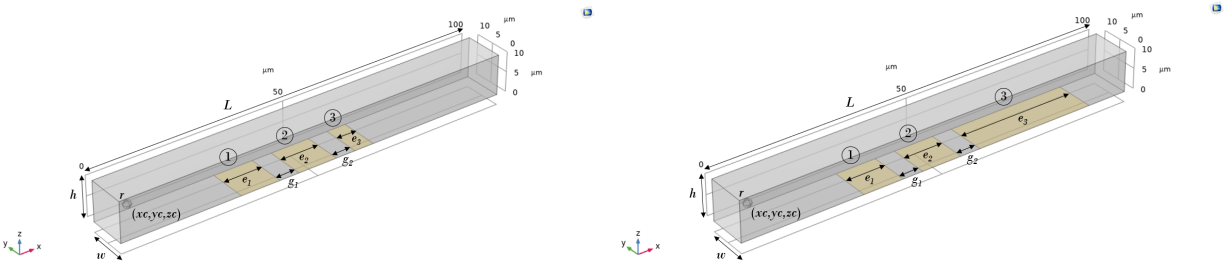

(a) (b)

Figure 3.9: Range of variation for e_3: (a) $e_{3,min} = 2.5$ µm, (b) $e_{3,max} = 30$ µm.

To begin with, the bead was moved along the length of the channel for different values of e_3; the remaining electrodes stayed unchanged. With $yc = zc = 5$ µm, a sweep of xc was explored and the obtained differential current is illustrated in Figure 3.10a. Additionally, the bead was pinned in between electrode 2 and 3, with $yc = zc = 5$ µm, while only the width e_3 was varied (Figure 3.10b). Looking at the first plot, it is evident that the background signal decreases in magnitude, i.e. the whole bipolar double Gaussian shifts downwards, for $e_3 < 10$ µm, while it increases, i.e. the entire curve shifts upwards, for $e_3 > 10$ µm. For 15 µm and beyond, no significant alteration is appreciable. The variation of e_3 does not yield any change in the shape of the Gaussian, meaning that the position of the peaks and their width is not affected at all. In the second plot, it can be observed that the current increases with e_3, but a plateau is reached from 15 µm onward; this behavior is very similar to the symmetric case in which the width of all electrodes was modified (see Figure 3.8a).

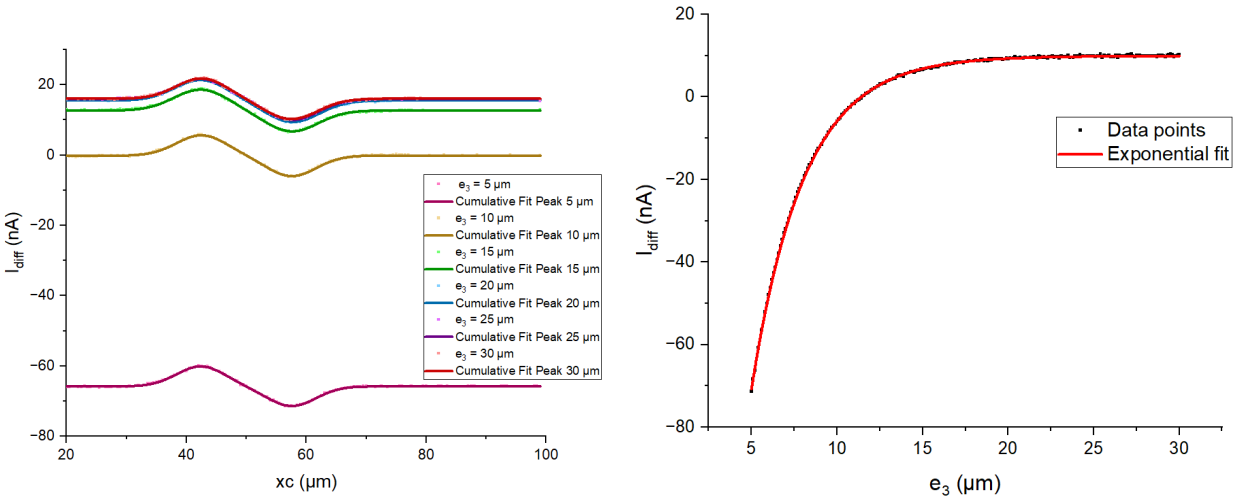

(a) . (b) .

Figure 3.10: Analysis of asymmetric configuration where e_3 is modified. (a) I_{diff} as a function of xc for different values of e_3 and (b) I_{diff} as a function of e_3.

When comparing to the symmetric case in section 3.1, no peculiarity useful to the objective can be observed in the analyzed results. Therefore, the strategy of varying electrode

width e_3 was declared ineffective.

3.2.2 Variation of e_2

The extremes of the range into which e_2 was modified are showed in Figure 3.11 for improved visual clarity.

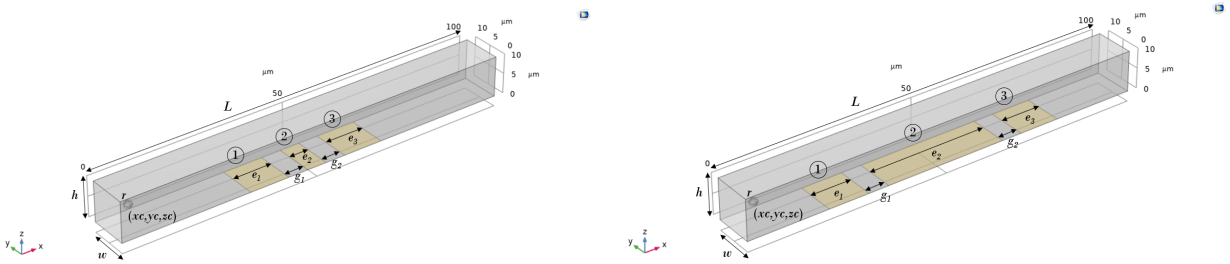

(a) (b)

Figure 3.11: Range of variation for e_2: (a) $e_2 = 2.5$ µm, (b) $e_2 = 30$ µm.

The particle was shifted along the length of the channel for different values of e_2, while the remaining electrodes remained constant. With $yc = zc = 5$ µm, a sweep of xc was carried out and the resulting graph for I_{diff} is visible in Figure 3.12a. The width of the peaks is not affected, but the signal shrinks slightly for $e_2 = 5$ µm; the position of the peaks is affected as well, as they shift towards the center of the transition at $x = 50$ µm. The opposite occurs for $e_2 = 30$ µm, seeing that the separation between positive and negative peak is greater.

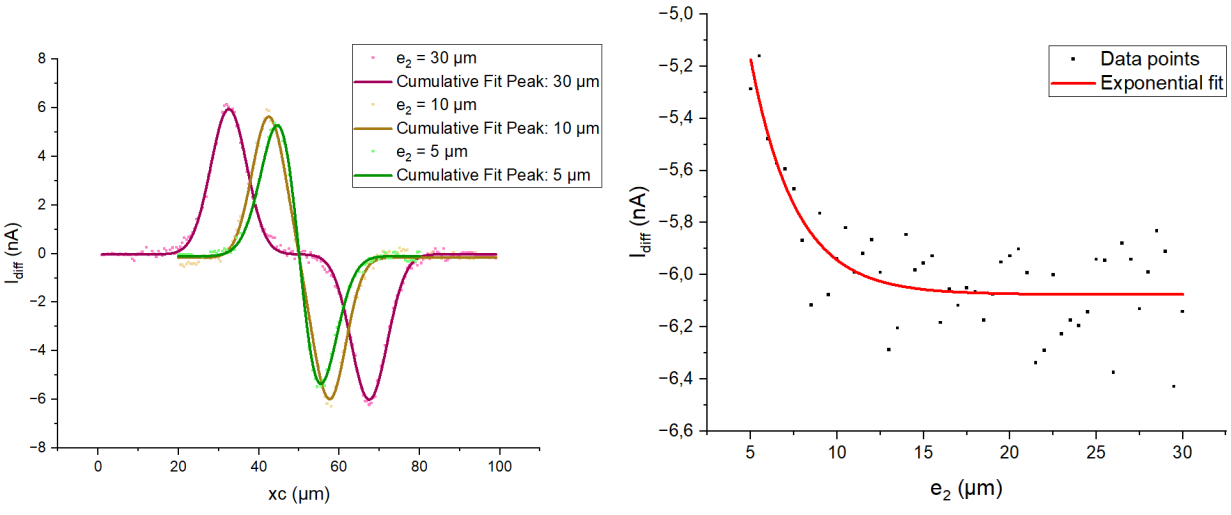

(a) . (b) .

Figure 3.12: Analysis of asymmetric configuration where e_2 is modified. (a) I_{diff} as a function of xc for different values of e_2 and (b) I_{diff} as a function of e_2.

For the second simulation of this case study, the bead was pinned in between electrode 2 and 3, with $yc = xc = 5$ µm, while only the width e_2 was varied (Figure 3.12b). The signal appears to be very noisy and no useful information could be extrapolated.

This approach was inconclusive as well.

3.3 Three asymmetric coplanar electrodes: changing gaps

A further strategy to be implemented was the introduction of asymmetry in the gaps between the electrodes: this time, e_1, e_2 and e_3 were kept constant and equal to 10 µm, which has been verified to be the most suitable choice in subsection 3.1.4. Due to the conclusions regarding the gaps in the same subsection, g_1 was unmodified as well and set as 5 µm. The limits of the range in which g_2 was varied are shown in Figure 3.13.

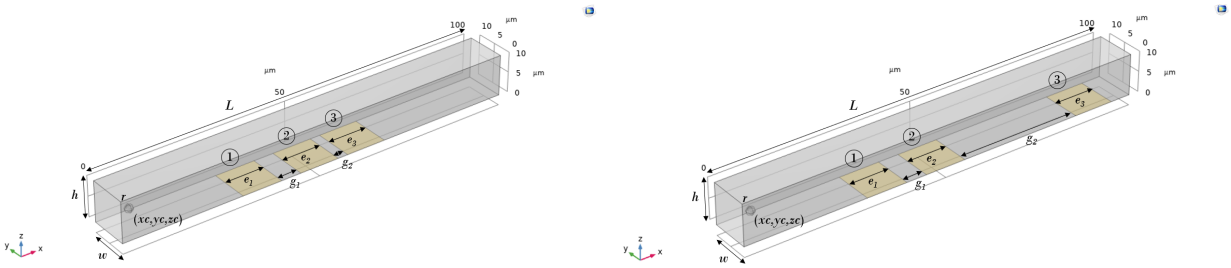

(a) (b)

Figure 3.13: Range of variation for g_2: (a) $g_2 = 2.5$ µm, (b) $g_2 = 30$ µm.

3.3.1 Determination of gap widths

As a continuation of the thought process followed until now, the bead was moved along L in the center of the cross section of the channel ($yc = zc = 5$ µm) for multiple values of g_2. The general outputs are plotted in Figure 3.14a, where it can be observed that the background signal changes in magnitude as the asymmetry in the system increases: if $g_2 > g_1 = 5$ µm the curve shifts downwards, while it shifts upwards for $g_2 < g_1 = 5$ µm. However, the most notable remark arises when zooming in on one single curve, which can be seen in Figure 3.14b. The asymmetry of gaps is reflected in asymmetry in the bipolar double Gaussian, as now the negative peak appears wider and lower in magnitude with respect to the positive one. Potentially, these characteristics may be linked to the position of the particle along h and that is what the subsequent analysis will focus on.

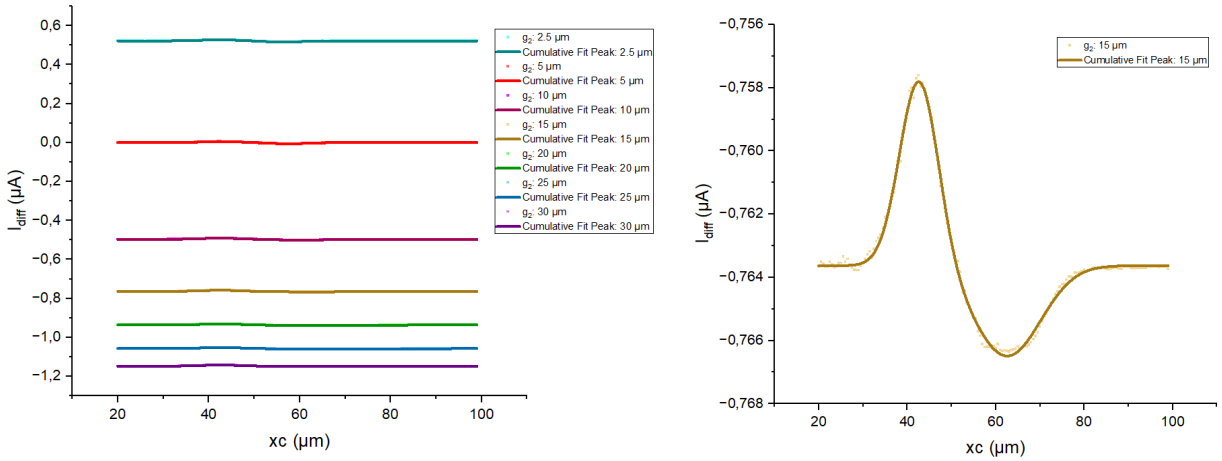

(a) (b)

Figure 3.14: Analysis of asymmetric configuration where g_2 is modified. (a) I_{diff} as a function of xc for different values of g_2 and (b) I_{diff} as a function of xc for $g_2 = 15$ μm.

In the following subsections, g_2 will be fixed at 15 μm. In this way, the asymmetry in the bipolar double Gaussian is ensured and, at the same time, the loss of current magnitude characteristic of larger gaps (see Figure 3.8b) is minimized. A picture of the final geometry is shown in Figure 3.15 and its dimensions are detailed in Table 3.3.

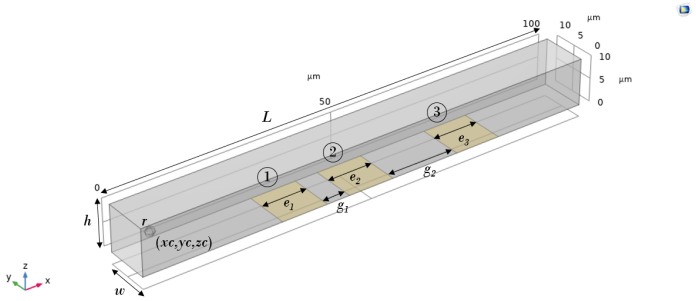

Figure 3.15: Final geometry for a three-coplanar-electrode configuration with asymmetric gaps.

Table 3.3: Final geometrical parameters for a three-coplanar-electrode configuration with asymmetric gaps.

L	h	w	$e_1 = e_2 = e_3$	g_1	g_2
100 μm	10 μm	10 μm	10 μm	5 μm	15 μm

3.3.2 Effect of zc

Once the geometry of the electrodes has been set, the impact of the zc position of the bead on the asymmetric curve needs to be investigated. The particle was moved along L in the center of the channel width ($yc = 5$ µm) for multiple values of zc; the resulting graph is depicted in Figure 3.16.

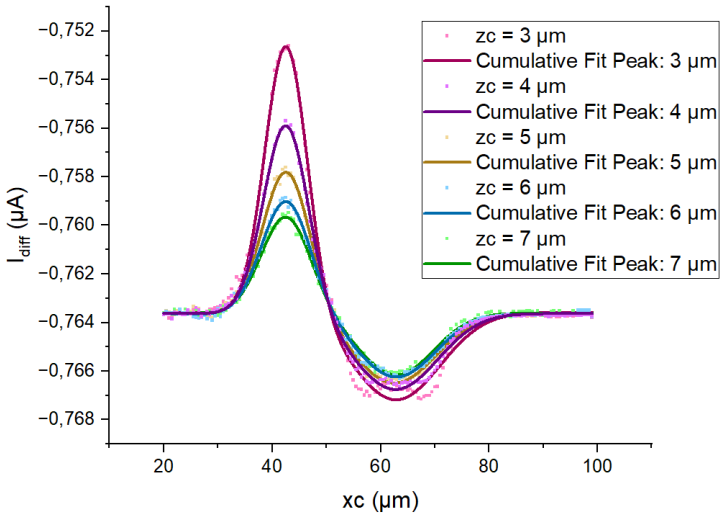

Figure 3.16: I_{diff} as a function of xc for multiple values of zc in an asymmetric three-coplanar-electrode configuration.

As expected, both positive and negative peaks decrease in magnitude as the bead moves further away from the electrodes at the bottom of the channel. When the particle is in close proximity with the terminals, e.g. $zc = 3$ µm, the accuracy of the fitting is uncertain especially around the negative peak; the double peak nature of the data points extracted from COMSOL in that region was attributed to electric field edge effects.

Seeing that the width of the peak and their magnitude vary, but asymmetry in the bipolar double Gaussian is maintained, possible relevant parameter relating to zc involve peak magnitude and the full width at half maximum (FWHM), which is the standard way to quantify the width of a peak in distribution theory. FWHM is defined as the width of the curve where the amplitude is half of its maximum value and, together with peak magnitude, could be the starting point to the development of a compensation strategy for the dependence on I_{diff} on zc. In particular, the ratio of such variables was chosen and new parameters were defined as

$$W_r = \frac{\text{FWHM of negative peak}}{\text{FWHM of positive peak}} \tag{3.3}$$

$$H_r = \frac{\text{Magnitude of negative peak}}{\text{Magnitude of positive peak}}. \tag{3.4}$$

W_r and H_r were extracted from each curve corresponding to a zc value in Figure 3.16 and plotted as a function of the bead position along the height of the channel in Figure 3.17.

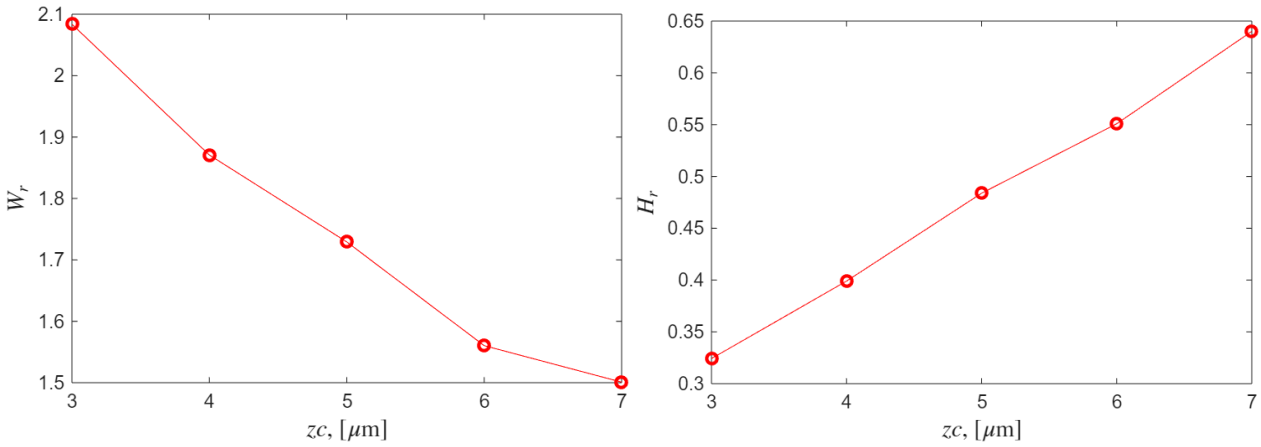

(a) (b)

Figure 3.17: Selected parameters as function of zc for a bead with $r = 1$ µm: (a) $W_r(zc)$ and (b) $H_r(zc)$.

A decreasing trend in W_r can be observed as the bead is moved towards the top of the channel, while the opposite tendency characterizes H_r. The result is promising, but, in order to be effective for a compensation strategy, W_r and H_r must not depend on the size of the bead. That is the reason why a variation in r will be implemented in the following.

W_r and H_r are the most encouraging ones, but they are just two of the possible parameters that can be extracted from Figure 3.16. More were taken into account and investigated, such as difference of FWHM W_d and magnitude of peaks difference H_d; their definition and their dependence on zc is reported in Appendix B.1.

3.3.3 Investigation on W_r and H_r

The same analysis discussed in the previous subsection was repeated for two more values of the bead radius, i.e. $r = 0.5$ µm and $r = 2$ µm. By keeping $yc = 5$ µm, the bead coordinate xc was swept for the same zc positions considered in Figure 3.16 and analogous curves were obtained (see Appendix B.2). W_r and H_r were extracted and plotted on the same graph in Figure 3.18.

It is possible to notice that, in both cases, the curve for $r = 1$ µm (red curve) and the one for $r = 2$ µm (blue curve) are almost exactly overlapping. When $r = 0.5$ µm (green curve), the data are not completely overlaying anymore. It is worth mentioning that, in the latter instance, the quality of the fitting for the bipolar double Gaussians is not as good as the previous ones (where R^2 was never lower than 0.99), with R^2 values as low as 0.79. Nevertheless, the overall tendencies are still valid, with W_r decreasing and H_r increasing as zc increases for all the considered values of r. That means that, if the trend is confirmed by experimental evidence, a strategy to compensate the dependence of I_{diff} on zc based on W_r and H_r may be developed.

Conceding that the determination of zc is achieved by analyzing the shape of the bipolar double Gaussian, i.e. by W_r or H_r, independently on the size of the bead that excited it, in principle a correction factor could be applied to the transition signal. In this way, after

post-processing of data, the curve would not be affected by the position of the particle along the height of the channel anymore.

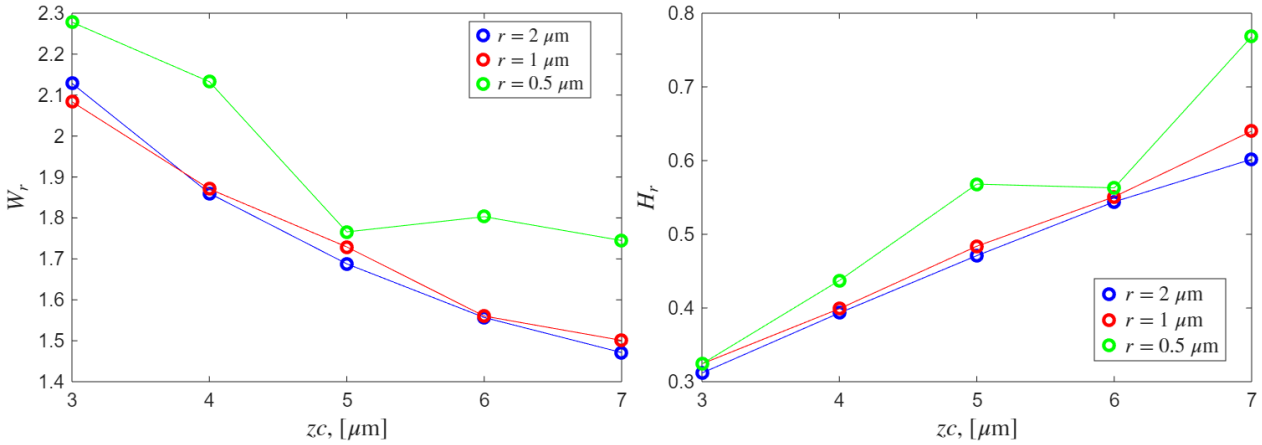

(a) (b)

Figure 3.18: Selected parameters as function of zc for a bead with different radii ($r = 0.5$ µm, $r = 1$ µm, $r = 2$ µm): (a) $W_r(zc)$ and (b) $H_r(zc)$.

Having assessed the potential of W_r or H_r as a starting point to develop a compensation strategy for the position-dependent signal intrinsic to a coplanar electrode configuration in IFC, the effectiveness of such computer-based deduction must be experimentally validated. However, it would not be possible to obtain directly the dependence of W_r and H_r on zc, as the position of particles along the height of the channel is not obvious and cannot be controlled in experiments. As will be detailed later in Chapter 5, the output of experimental data is the current as function of time, resulting in the bipolar double Gaussian characteristic of IFC: the magnitude of the positive peak can be extracted from it, which is equivalent to I_{diff} when the particle is in between electrode 1 and 2 along the length of the channel. The relationship between I_{diff} and zc obtained from simulations in these conditions was illustrated in Figure 3.6, thus, exploiting the fit in such plot for the selected electrode width of 10 µm, it is possible to convert the zc-dependence of W_r and H_r to an I_{diff}-dependence. The results are shown in Figure 3.19 and, in this way, the graphs can be directly compared with experimental data.

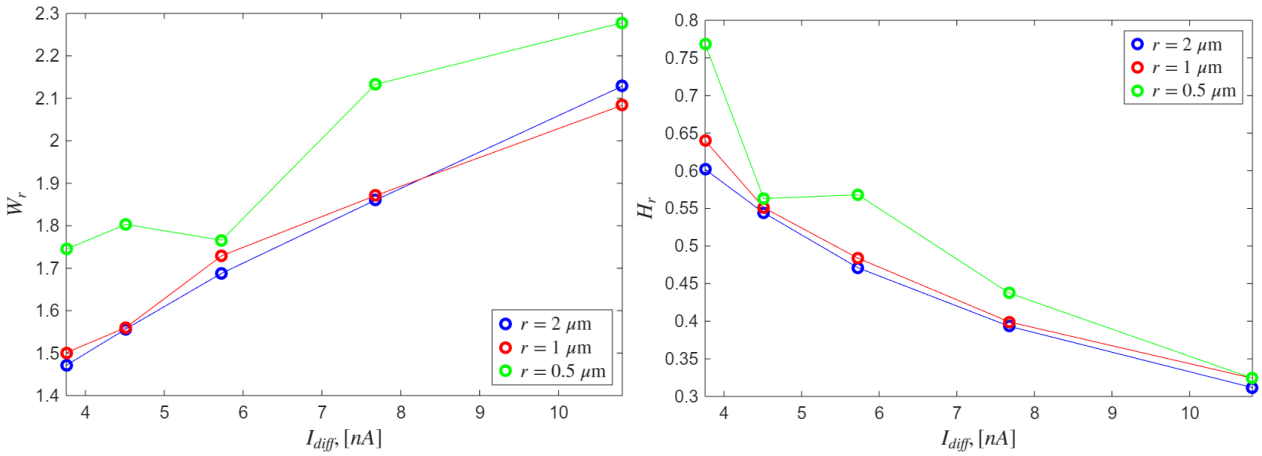

(a) (b)

Figure 3.19: Selected parameters as function of I_{diff} for a simulated bead with different radii ($r = 0.5$ µm, $r = 1$ µm, $r = 2$ µm): (a) $W_r(zc)$ and (b) $H_r(zc)$.

To acquire experimental data, a physical chip has to be designed and fabricated, therefore that is what the next Chapter will revolve around.

Chapter 4

Chip fabrication and design

This Chapter is focused on the layout and on the process of fabrication for the physical chip used for experimental measurements. The device developed in this thesis is made of two parts: a glass substrate onto which gold electrodes are patterned, and a Polydimethylsiloxane (PDMS) slab that will host the microchannels into which liquids can flow. The former was manufactured by Sara Di Paolo in the cleanroom at DTU Nanolab, while the latter was made in a standard chemistry laboratory. The mold for PDMS is an etched silicon wafer containing the microstructures for the channels, fabricated in the cleanroom as well. A cross section of the device is displayed in Figure 4.1.

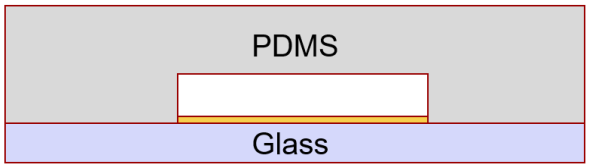

Figure 4.1: Cross section of the device: Au electrodes (yellow) are patterned on a glass substrate (blue), while the microchannels are casted in a PDMS slab (grey).

Besides tight bonding to prevent leakage of the sample, electrodes and PDMS need to be aligned carefully on top of each other, thus a few strategies were adopted to achieve that.

The choice for the materials was made based on the availability of equipment in the laboratories and on the 5-months time constraint that this Master thesis was subjected to: the relatively easy, fast and reproducible fabrication of PDMS and its good adhesion with glass was what deemed such materials to be the most suitable options for the project.

4.1 Chip design

Based on the work presented in Chapter 3 which showed encouraging results for a three coplanar electrode layout with asymmetric gaps, it was decided to fabricate a chip with this configuration. In particular, all electrodes were 10 µm wide and the first gap was 5 µm wide. Concerning the second gap, chips with $g_2 = 5, 15, 25$ µm were fabricated. In continuity with

COMSOL simulations in which the cross section of the channel was (10 × 10) µm, the same dimensions were chosen for the fabrication of a simple straight channel. A sketch of the overall layout for a chip is illustrated in Figure 4.2. A guideline to direct subsequent cutting of PDMS is present, delineating the correct rectangular shape for the final slab.

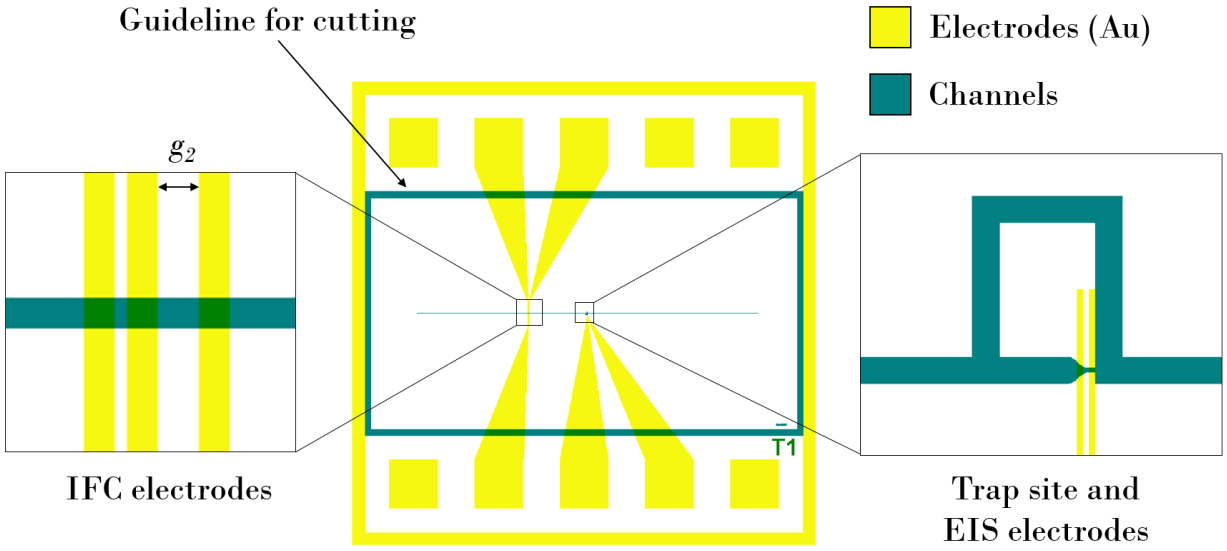

Figure 4.2: Chip design for fabrication: the trap site was designed by Sara Di Paolo.

The chip dimensions are (2 × 2) cm and both IFC and EIS electrodes are included, allowing for faster acquisition of results as they can be tested at once in the same experiment. EIS electrodes, along with the trap site, were designed by Sara Di Paolo.

A detailed walkthrough of cleanroom microfabrication is not part of this project and more can be found in Sara Di Paolo's thesis. A general overview of it is provided in the following.

4.2 Au electrodes

The gold electrodes are deposited on a boron silicate glass wafer, which allows for the monitoring of what is happening inside the final device thanks to its transparency. The process flow includes a photolithography step, a metal deposition step and a lift-off step to remove the remaining photoresist. Details about the process flow are reported in Appendix C.1 and an illustration of the various steps is depicted in Figure 4.3.

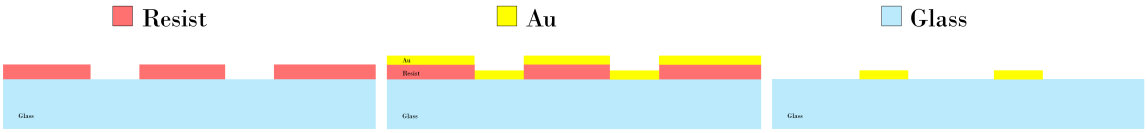

Figure 4.3: Electrode fabrication process: (a) resist (red) on glass wafer (blue) after lithography, (b) wafer after metal deposition of Au (yellow) and (c) wafer after lift-off.

A close up sketch of the glass chip after dicing of the wafer is reported in Figure 4.4. Connection pads can be seen on two sides of the frame: they will allow for connection to the equipment that both provides and collects the signal.

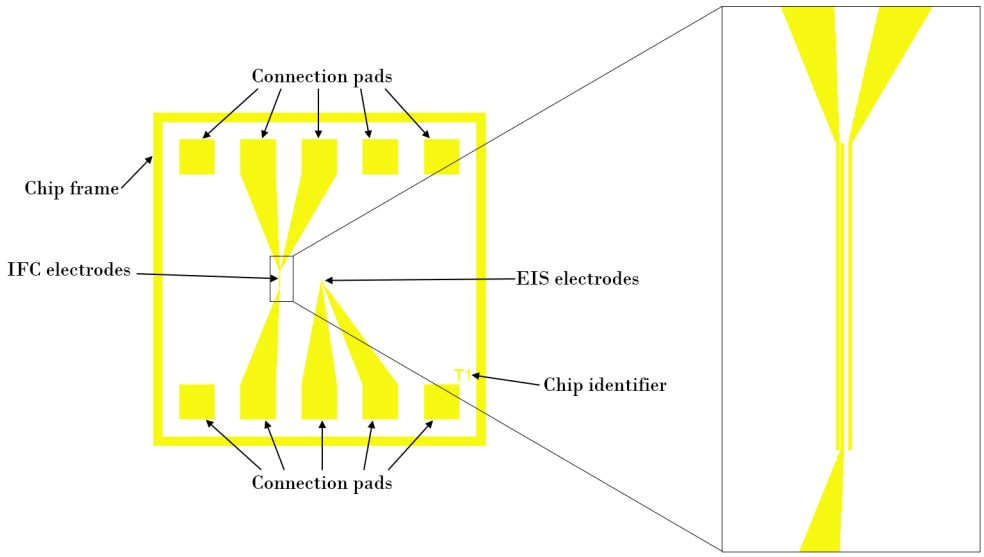

Figure 4.4: Glass chip patterned with Au electrodes: the main characteristics are highlighted and a zoom in on IFC electrodes is included.

The electrodes for IFC were specifically designed with vertical symmetry to facilitate alignment with the microfluidic channel. The system is compatible with both top and bottom channel placement along the length of the electrodes, increasing the tolerance for vertical alignment.

4.3 Si mold

IFC only requires a simple straight channel, while EIS involves more complex geometries in addition to the main channel. In order to imprint the layout of the microfluidic channels in the PDMS slab, a mold is needed and a Si wafer was chosen for the purpose. Due to its small dimensions, the only viable approach was cleanroom fabrication. The process flow for the production of the mold includes a photolithography step to spin-coat the photoresist that enables the dry etching step. The resist acts as a mask for etching, so that anything

underneath will not be etched away. After etching, the resist is stripped away and an anti-stiction coating is deposited via molecular vapor deposition on the Si surface. The purpose of the last step is to facilitate the detachment of the mold from the PDMS that has to be poured on top. The described process flow was optimized thoroughly by Sara Di Paolo and more can be read about it in her Master thesis; the final version can be found in Appendix C.2, while a representation of it is shown in Figure 4.5.

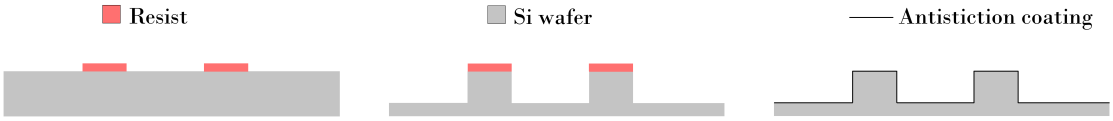

(a) (b) (c)

Figure 4.5: Si mold fabrication process: (a) resist (red) on Si wafer (grey) after lithography, (b) wafer after dry etching and (c) wafer after resist removal and anti-stiction coating deposition (black).

Due to the high aspect ratio of the target features, deep reactive ion etching (DRIE) is used to etch the Si wafer. This process involves the repetition of an isotropic etching step an a passivation step, which causes the sidewalls of the final product to present scallops. The scalloped sidewalls resulting from DRIE were initially suspected to represent a problem in the release of the cured PDMS from the Si mold due to increased surface roughness. However, no significant complication was encountered during demolding, meaning that scallops did not negatively affect the replication process. Scalloped sidewalls are visible in Figure 4.6b, while a full Si microstructure can be seen in Figure 4.6a.

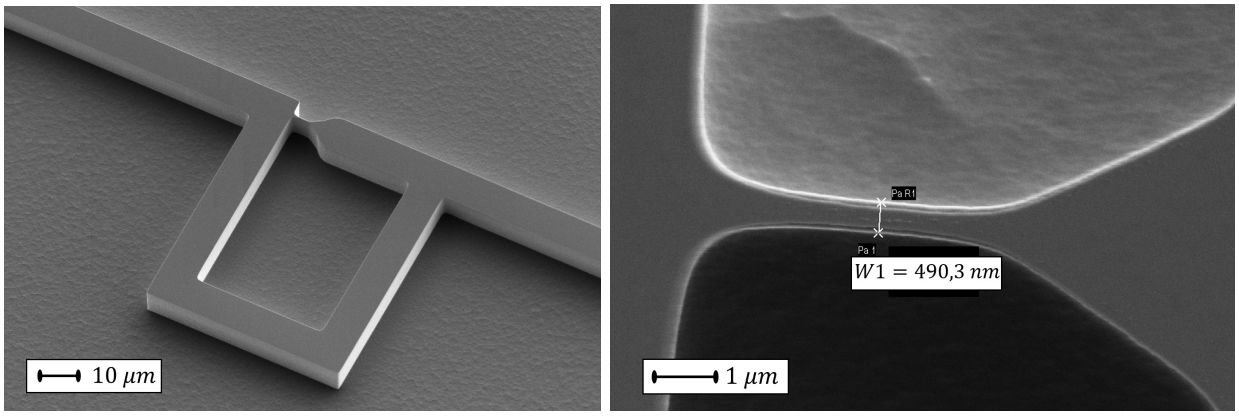

(a) (b)

Figure 4.6: SEM image of the etched Si mold: (a) trap site and (b) close up on scallops.

4.4 PDMS slab

PDMS is a mineral organic polymer widely employed for soft lithography in microfluidic devices. Its advantages include transparency, chemical stability, ease of fabrication and good

adhesion with glass. [41]. These characteristic made it the most suitable choice for the device developed in this project.

Once the Si mold is obtained, liquid PDMS can be poured on top of it. SYLGARD 184 Silicone Elastomer kit is used, which contains a liquid polymer and a curing agent. The production protocol includes mixing the two components, pouring the mixture on top of the mold, desiccate it to let incorporated air out and letting it cure. Details about the protocol are stated in Appendix C.3.

After curing, PDMS is cut with a scalpel following the imprinted guidelines that yield a (16 × 8) mm slab. Then, holes are punched throughout the thickness of the slab, at the two ends of the main channel. The holes are where tubing will be connected to the chip, in order to allow for the injection of fluids. It is possible to cut the PDMS and punch the holes by naked eye, as the imprinted microstructures are large enough to be visible. Nevertheless, particular care is needed in making sure that punched holes connect to the main channel and that extra PDMS flakes do not accidentally obstruct it.

Inspection of the punched holes with an optical microscope revealed that the exit side exhibited more damage and less well-defined edges compared to the entry side, as shown in Figure 4.7. Therefore, the entry side was deemed to be better suited to be in contact with glass when bonding the chip. This approach was intended to reduce the risk of damaging the microfluidic channels during manual hole punching. However, despite this precaution, it was not sufficient to prevent all chips from experiencing some degree of damage near inlet and outlet holes.

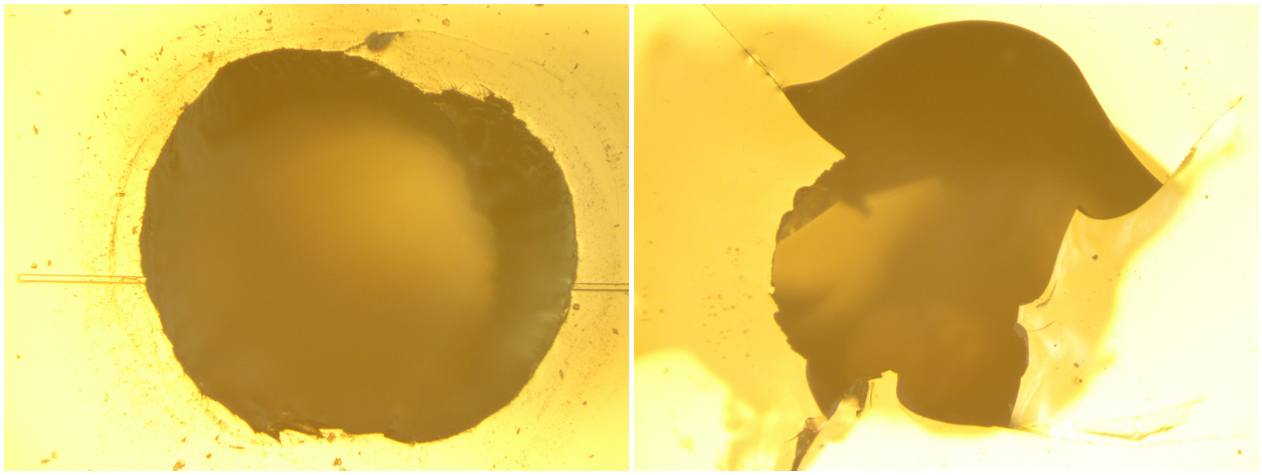

(a) Entry hole. (b) Exit hole.

Figure 4.7: Punched holes in PDMS: (a) entry side of the hole, less damaged and (b) exit side of the hole, more damaged.

4.5 Chip assembling

Once all the components of the chip are fabricated, the finalization of the device involves alignment and bonding of the two parts. Several approaches were implemented and they

will be detailed in the following.

4.5.1 Glass-PDMS alignment

Careful alignment of glass and PDMS is necessary in order to position the electrodes in the correct location to record a signal. In particular, the trap site is characterized by small dimensions down to 1 µm due to the size of the target particles. In this context, as shown in Figure 4.8, precise placement of EIS electrodes is critical because any misalignment could result in the signal from the single trapped particle being affected by contributions from the surrounding flow, thereby compromising the accuracy of the measurement.

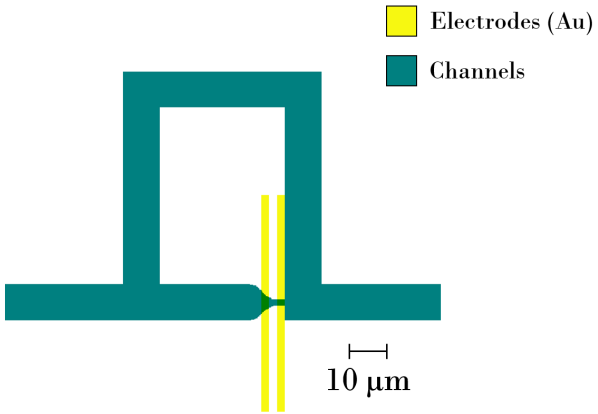

Figure 4.8: Trap site designed on the software CleWin6 by Sara Di Paolo: EIS electrodes (yellow) must be aligned accurately with the channels (blue).

An alignment framework and a microscope plate were designed to facilitate the union of glass and PDMS. The concept originated from the ability of an optical microscope to move samples in the $x - y$ plane. In this setup, the PDMS slab is held stationary, while the glass chip is maneuvered beneath it using the microscope stage. This allows for alignment under suitable magnification. Once the desired positioning is achieved, the PDMS can be carefully pressed onto the glass to complete the alignment process. The framework was designed on Autodesk Fusion (formerly Fusion 360) v.2602.0.71, a computer-aided-design software for the modeling of objects. A rendering of the alignment framework and of the custom microscope plate is displayed in Figure 4.9. It is worth highlighting that design and dimensions are suitable specifically for the optical microscope OLYMPUS CKX31 belonging to the NaBIS research group in DTU Bioengineering facilities.

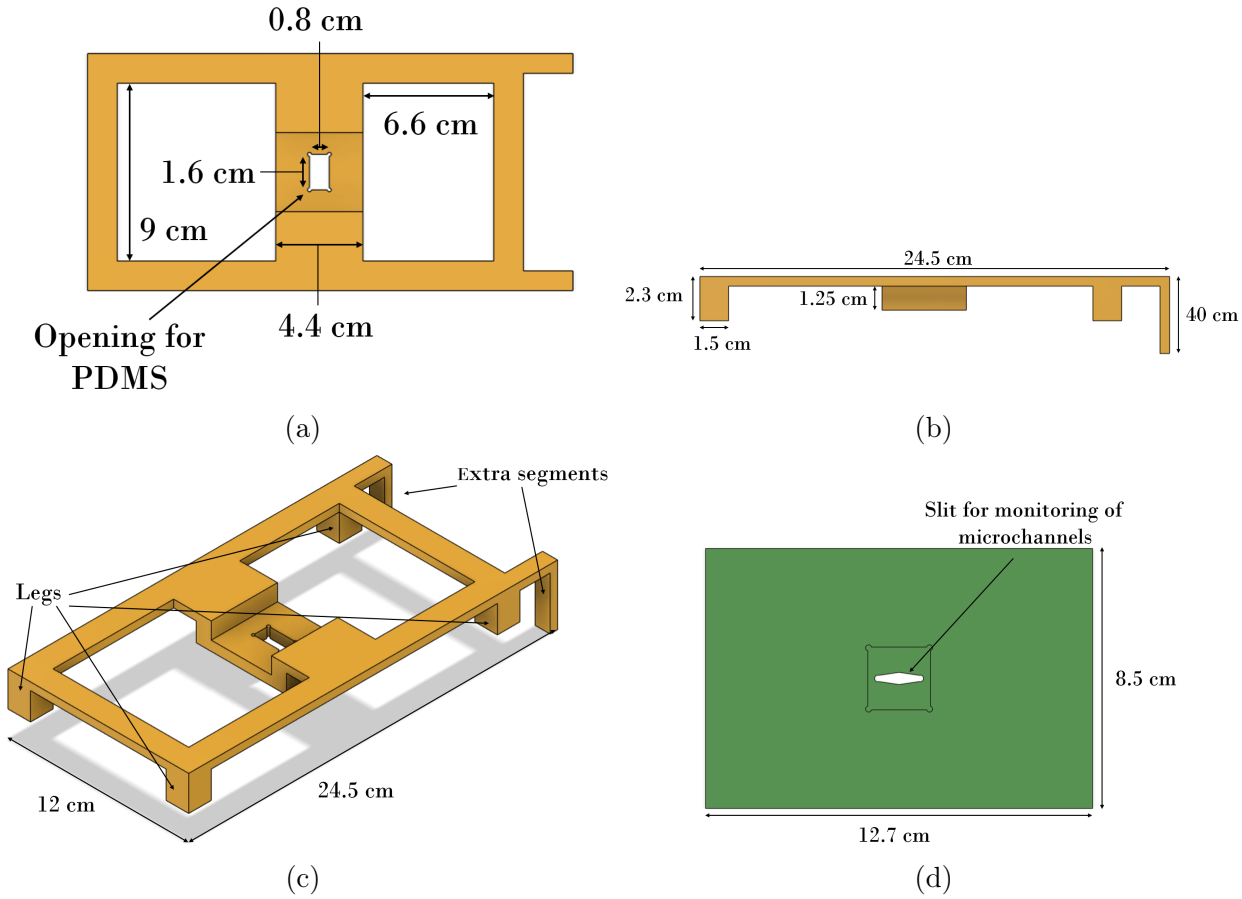

Figure 4.9: Rendering of alignment components: (a) top view of framework, (b) side view of framework, (c) overall view of framework and (d) top view of microscope plate.

The framework consists of a support structure where an opening with the same dimensions as the PDMS slab is present (Figure 4.9a). Once stuck in the opening, PDMS will be slightly compressed and hence, thanks to its elastic nature, it will not slide down due to gravity. At the same time, it will be easy to simply push it down when the correct alignment is achieved. The framework is sustained by four legs that are meant to rest on the fixed part of the equipment, but two extra segments are added on one side (Figure 4.9c): the purpose is to take into account and limit any rotational misalignment in the plane by exploiting the frame of the microscope. A custom microscope plate was designed as well, in order to allow for the hosting and movement of the glass chip; a slit to permit live monitoring with a microscope is present (Figure 4.9d).

The framework and the microscope plate are in close proximity, but not in contact: this permits the free movement of the plate through the mechanism of the optical microscope, while the framework is fixed and hovering over it. Once that the glass chip is positioned on the plate and that PDMS is mounted in the framework, the first step is to focus on the alignment marks imprinted in the PDMS; considering that the distance between PDMS and glass is minimal, the alignment marks on glass will be visible as well, even if blurry. A small change in focus allows to obtain the best resolution on them, thus alignment is possible by

shifting the focus back and forth. After that, applying pressure on the exposed surface of PDMS is enough to put the two parts in contact.

Both the framework and the custom microscope plate were 3D-printed with a Bambu Lab P1S printer; a white PLA Basic filament was employed. The final printed elements are displayed in Figure 4.10.

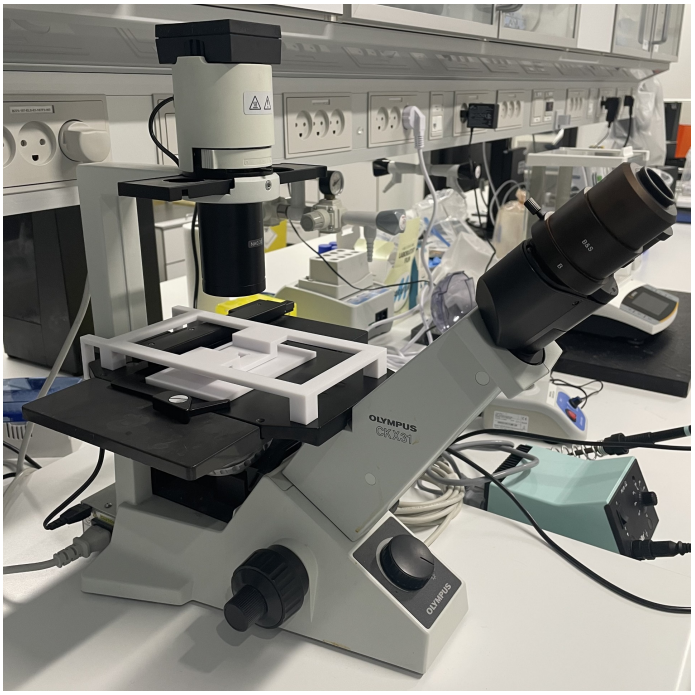

(a)

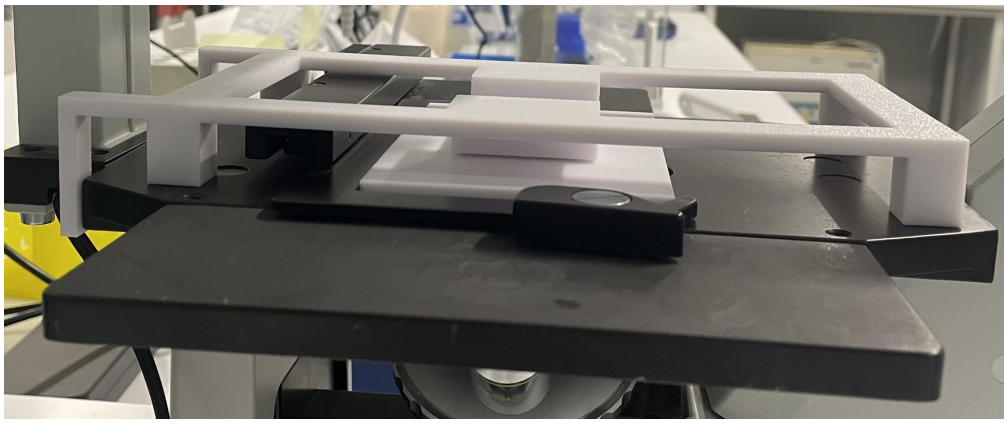

(b)

Figure 4.10: 3D-printed alignment framework and custom microscope plate placed on the optical microscope: (a) overall view and (b) side view.

4.5.2 Chip bonding

After fabricating the two parts composing the chip, a tight seal to avoid leakage is necessary. At first, simply applying pressure on top of the PDMS was tested out; however, when injecting liquid through the inlet, the fluid was not contained inside the channel and it leaked underneath the PDMS, provoking potential disruptions in the stream and altering a flow that is supposed to be laminar. A reason for the leakage can be found in the pressure to which the system is subjected to when liquids are introduced: the hydraulic resistance for such a small channel is very high, thus, according to Hagen-Poiseuille law, the pressure difference between inlet and outlet required to have flow is very high as well (see subsection 2.2.2). This excessive pressure may be the cause of detachment if the two parts are not tightly sealed.

An alternative and more successful method in obtaining a closed chip consists in oxygen plasma bonding: the surfaces to be bonded are cleaned and placed in a vacuum chamber at 0.5 torr, then an RF signal is applied to create plasma. The plasma interacts with the target surfaces and it activates them, meaning that it makes them chemically reactive by increasing their surface energy; this is possible thanks to the radicals composing the plasma, which are able to interact with the surfaces creating new highly reactive functional groups. Then, glass and PDMS are pressed together and annealed at 64 °C for 5 minutes to increase the strength of the chemical bond. This process yields a chip that is sealed tightly: no liquid was observed to leak after plasma bonding was performed. A picture of the final chip is shown in Figure 4.11.

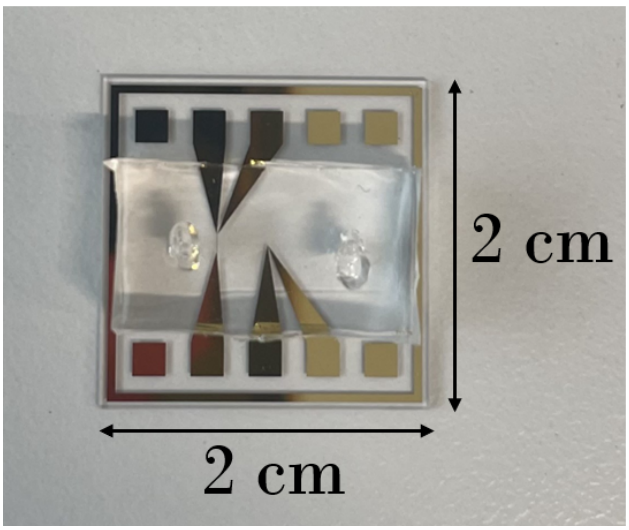

Figure 4.11: Top view of the final chip.

Chapter 5

Methodology

In this Chapter, all equipment and procedures that made the acquisition of experimental data achievable are illustrated. After clarifications on experimental setup and procedure, specification about the preparation of the tested samples are provided. Finally, details on the acquisition and analysis of data are included.

5.1 Experimental setup

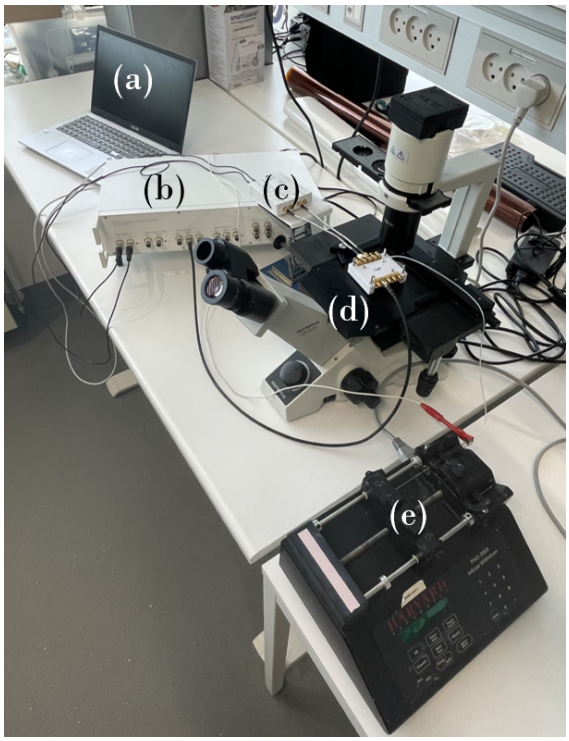

Figure 5.1: Experimental setup: (a) computer for data acquisition, (b) impedance spectroscope, (c) current amplifier, (d) optical microscope and (e) syringe pump with syringe.

The equipment needed for IFC measurements is displayed in Figure 5.1 and it includes:

- disposable 1 ml syringe with metallic 19G needle;
- syringe pump PHD 2000, Harvard Apparatus;
- plastic tubing (inner diameter: 0.8 mm, outer diameter: 1.6 mm);
- optical microscope OLYMPUS CKX31;
- impedance spectroscope HF2IS, Zurich Instruments;
- current amplifier HF2TA, Zurich Instruments;
- computer for data acquisition.

In particular, in order to allow for electrical connections, the chip necessitates a holder to support it, keep it steady and permit contact with a printed circuit board (PCB). Both components were designed specifically for the chips involved in the project.

5.1.1 Chip holder

A support for the chip was designed on Fusion and then 3D-printed: it is made of a top part and a bottom part, a rendering of which is illustrated in Figure 5.2. The optimization of the holder required the printing of several copies, but the dimensions reported concern the final version.

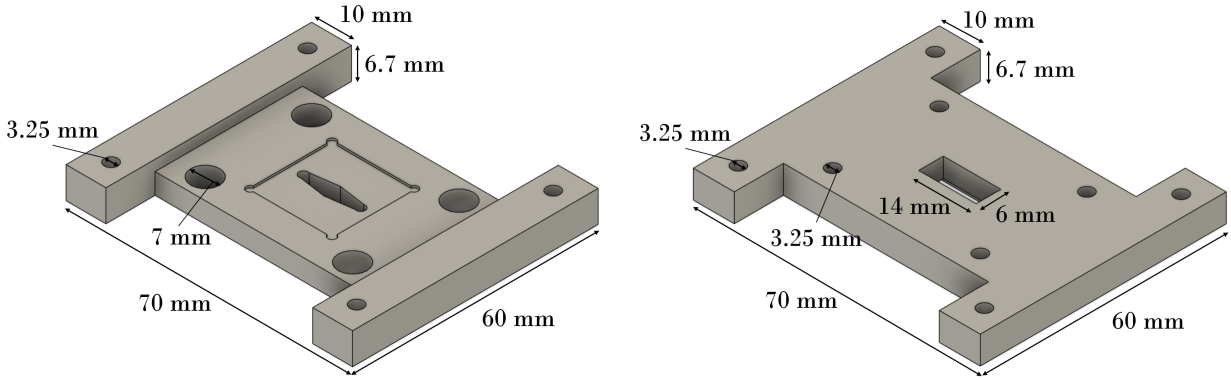

(a) (b)

Figure 5.2: Rendering of chip holder for experimental measurements: (a) bottom part with hosting for the chip and (b) top part. Both parts present holes for screws.

The bottom part (Figure 5.2a) includes a square indent for the hosting of the chip (with a slit to allow for visualization of the channel), bigger holes for bolts and smaller holes for screws.

The top part (Figure 5.2b) has a similar shape: holes for screws are present and a (14 $\times$ 6) mm rectangular opening in the middle allows for the connection of tubing to inject liquids. The perimeter of the opening is smaller than the one of the (16 $\times$ 8) mm PDMS slab, hence the top part of the holder can rest on the PDMS and secure it.

5.1.2 Printed circuit board

A PCB is a fundamental element in most electronic devices, as it provides mechanical support while enabling connections between components through electrical pathways. Electrical connections in the device were provided by a custom PCB designed with the software KiCad 9.0 and ordered from the company PCBWay. Spring pins and SubMiniature version A (SMA) connectors were soldered with tin to the board: the former have to be put in contact with the Au connection pads on the chip (see Figure 4.4), while the latter allow for connection to the impedance spectroscope for data acquisition. Each SMA connector is associated to a copper pathway on the PCB ending in a spring pin, thus an electrical signal can be applied to each connection pad. A picture of the PCB with spring pins and SMA connectors is shown in Figure 5.3.

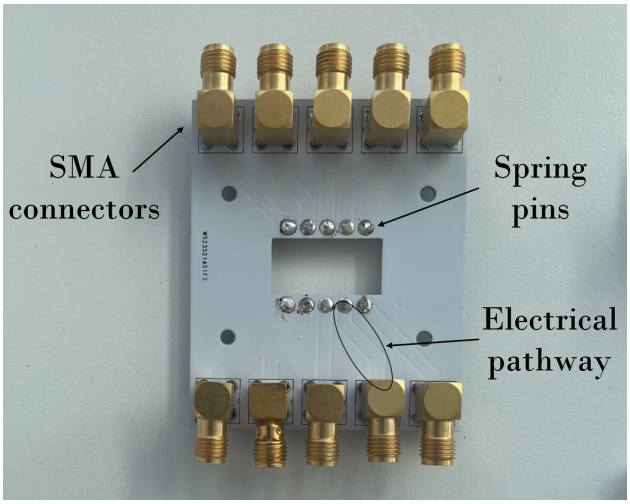

Figure 5.3: PCB with soldered spring pins and SMA connectors. Holes for screws and a rectangular opening to let the PDMS through are present.

The PCB can be secured to the top part of the holder by screws terminating with bolts that fit through the bigger holes in the bottom part of the holder. Then, the system composed by (from bottom to top)

1. bottom part of the holder
2. chip
3. PCB
4. top part of the holder

is fixed together with additional screws and ready to be placed on the optical microscope and be used in experimental measurements. A picture of it is shown in Figure 5.4.

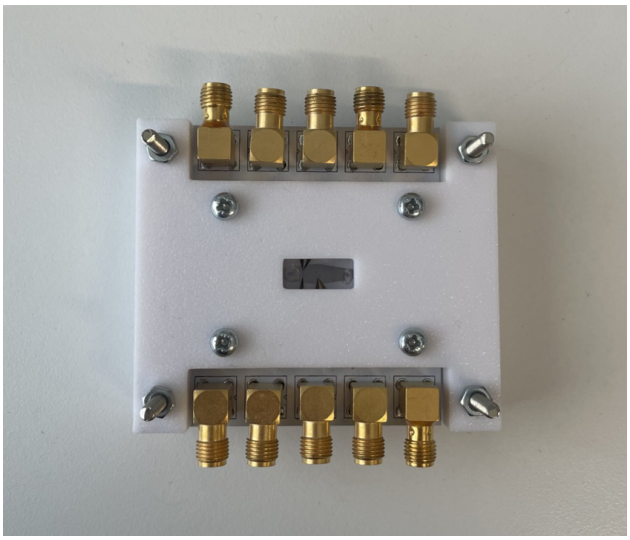

Figure 5.4: Final system for experimental measurements: the chip is supported by a custom 3D-printed holder that allows for the inclusion of the PCB as well.

5.2 Measurement procedure

After connecting plastic tubing to the inlet of the chip on one end and to the syringe on the other, the sample is injected into the system by means of the syringe pump. The employed flow rate is set between 0.01 µl/min and 1 µl/min. A higher flow rate would subject the chip to excessive pressure, potentially provoking the detachment of PDMS and glass. Furthermore, particles cannot de detected properly by the sensor if they are traveling too fast [42] and the signal to noise ratio decreases. A lower flow rate is not achievable with the available instrumentation as the mechanism of the syringe pump operates in steps based on the inner diameter of the syringe. The lower resolution for the plastic syringe in use is 0.01 0.01 µl/min. In general, the flow rate was initially set to 1 µl/min until the sample reached the electrodes; after that, it was lowered to 0.01 µl/min and allowed to stabilize for a few seconds before data acquisition.

An additional segment of tubing is attached to the outlet of the chip to collect waste. Details on how electrical excitation is applied in input and registered in output are provided in the following.

5.2.1 Impedance spectroscope and current amplifier

A schematic of how data acquisition is enabled can be seen in Figure 5.5. A potential is applied to the middle excitation electrode, then the current is measured on each of the two outermost detection electrodes and subtracted. As explained in subsection 2.3.1, the differential signal is zero if no particle is present in the channel.

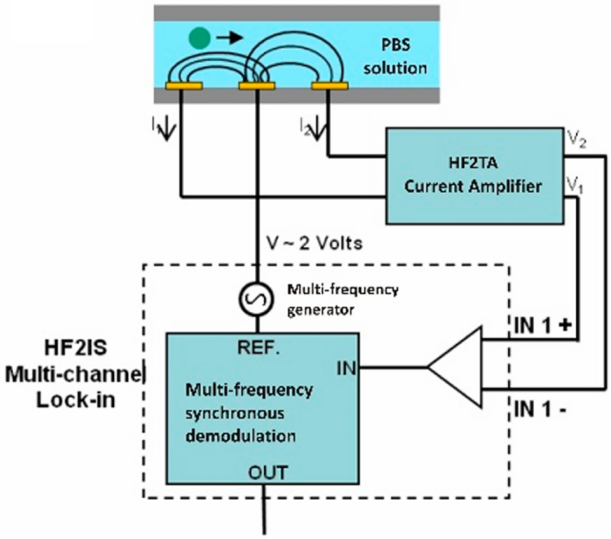

Figure 5.5: Schematic of the signal path, involving the impedance spectroscope HF2IS and the current amplifier HF2TA. Taken from [7].

An impedance spectroscope analyzes the reaction of a system to alternating current across a range of frequencies. A sine wave with up to 8 frequencies at a time can be generated, but in this project only one frequency, i.e. 250 kHz, will be tested out. The choice was guided by a previous project involving a microfluidic chip with coplanar electrodes, where it was experimentally found that the frequency range of interest was between 100 and 250 kHz [23]. The signal is converted to an analog one in a digital-analog converter (DAC), then it is provided to the chip. After exiting the chip, the signals from each of the two detection electrodes are amplified through a transimpedance amplifier (TIA). Amplification can be set manually on the software provided by Zurich Instruments; it has to be very high in order to amplify the small changes in current induced by the transitions of particles. Then, the two signals are subtracted from each other and the differential signal is converted to a digital one in an analog-digital converter (ADC) for further processing.

The principle of detection in the impedance spectroscope relies on the use of a lock-in amplifier (LIA) to generate and detect the signal: when the signal is buried in noise, a LIA makes its detection possible. The noisy input signal is multiplied with a synchronous reference signal, meaning that they have the same frequency. This is called demodulation and it shifts the desired signal to DC (zero frequency), while the noisy background is shifted to higher frequencies. The noise is then removed by a low-pass filter, which is designed to cut off high frequency components. The remaining signal is directly related to the original one at the reference frequency. Setting the correct cut-off frequency for the low-pass filter is crucial in ensuring that enough noise is suppressed while preserving the essential signal components.

The sample rate must be carefully selected as well, as it affects the reliability, accuracy and resolution of signal detection and analysis. Sampling too slowly causes aliasing, where high frequency signals are not registered correctly and misinterpreted as lower frequencies. Conversely, a higher sample rate improves the resolution in the frequency domain and the ac-

curacy of demodulation. However, an excessively high sample rate would yield unnecessarily heavy data files.

5.3 Sample preparation

The sample injected in the chips consists of an electrolyte medium into which particles are dispersed. The electrolyte is Dulbecco's Phosphate Buffered Saline (PBS) solution from Sigma Aldrich, diluted with Milli-Q water at various concentrations. Both pure 1x PBS and 1/20x PBS were tested: the results for the two cases are presented in the next Chapter.

The dispersed particles are polystyrene microbeads from Polysciences Inc. with a 2 µm diameter. They are close in size to bacteria and small enough to reduce the risk of clogging the channel, but not too small that they cannot be seen with the available optical microscope. A concentration between 1×10^6/ml and 5×10^6/ml was used in all cases, to ensure enough transitions in the running time for experiments.

The sample has to be mechanically agitated before use to prevent sedimentation in the vial and the formation of agglomerates that may clog the syringe. During time consuming experiments, it is also recommended to periodically turn the syringe upside down to maintain suspension and prevent clogging.

5.4 Data acquisition and analysis

The data is acquired using the software Zurich Instruments LabOne, which captures both real and imaginary part of the differential current for the selected frequencies. Electronic settings and parameters for the acquisition are user-defined.

The acquired data is analyzed with the software MATLAB, using a script developed for previous projects in the NaBIS group. The script is conceived for the handling of two frequencies at a time, but only one was used in this project. After importing the data, further low-pass filtering is possible and a noise level is defined by the user so that only proper particle transitions are detected. Then, the peaks are found in the real signal by searching for maxima in the data stream and their location is stored. The peaks in the imaginary signal are found by searching the immediate area of the real peaks and their position is stored as well. The graph for a single transition is reported in Figure 5.6.

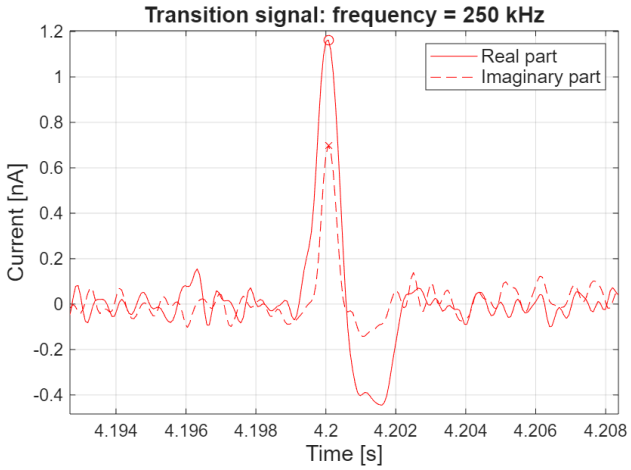

Figure 5.6: Transition of a particle identified with MATLAB.

After identification with MATLAB, the data for each transition was imported and analyzed on OriginPro in the same way that simulated data was: a Gaussian fit was performed and relevant parameters such as FWHM and magnitude of the peaks were extracted. Further processing was carried out on MATLAB.

It is to be highlighted that only data for the real part of the signal was taken into consideration.

Chapter 6

Experimental results

This Chapter presents the experimental work conducted in the final period of the project. Many issues in the detection of particle transitions were encountered in the beginning, hence a long time was spent troubleshooting and attempting to identify the main causes that lead to the delay of signal registration. Firstly, the adopted strategies are discussed and the different precautions that eventually lead to events detection are highlighted. Then, after the characteristic bipolar double Gaussian of particle transitions in IFC was achieved, the results are presented and a walkthrough on the extraction of relevant parameters introduced in Chapter 3 is illustrated. Polystyrene microbeads with a 2 µm diameter were employed in all experiments.

6.1 Achieving transitions of particles

The acquisition of a current registered at the detection electrodes was not immediately achieved. Several issues were encountered, which made the experimental measurements difficult to carry out. Data from the IFC electrodes were finally able to be acquired in the last weeks of the project, therefore the investigation of it was constrained by time limits. Due to the already mentioned complications in aligning EIS electrodes, no full-frequency spectrum data acquisition was possible.

In the first place, some considerations were made in order to establish the order of magnitude of the parameters for the electronics. It was considered reasonable to have a resolution of a transition (from peak to peak) of at least 10 measurement points and, for the selected geometry of IFC electrodes, the distance that a particle travels in that time is 20 µm. It is equivalent to a transition time of approximately 12 ms, for a flow rate of 0.01 µl/min in a (10 × 10) µm channel, so the sample rate was set to at least 1000 Sa/s in order to achieve the target resolution for a transition. The transition frequency is approximately 100 Hz for the same settings, therefore the cut-off frequency of the low pass filter was set higher than that. Further filtering of data to neglect high-frequency noise was possible with the MATLAB script for data processing.

The frequency of the signal was set to 250 kHz according to the research group standard and a voltage of 1 V was applied. Undiluted PBS was initially employed as the conductive medium.

One of the first observed complications was to get the sample into the channel. It was unsure if it was due to leakage in the system or if the channels of some of the tested chips were clogged. PDMS flakes deriving from the punched holes for the connection of tubing were speculated to be the reason for the obstruction of channels. Moreover, another potential reason for that was found in contamination of the surfaces before chip bonding: glass and PDMS must be cleaned thoroughly to prevent clogging due to dust particles.

To ensure the presence of sample in the channel, the flow rate was set to higher values, up to 1 um/min, until a sinusoidal signal was registered on the spectroscope: that indicated the existence of electrical connections between the electrodes, so the presence of an electrolyte in the channel.

Once the presence of sample in the channel was verified, at first no transition was detected. As a first approach to solve the issue, the electronics parameters such as sample rate, low-pass filter cut-off frequency and voltage were tuned to assess their influence, but the method was not effective in obtaining transition signals.

Then, a glass syringe was tested out: the new syringe had a smaller diameter, allowing for a finer control of the flow rate set on the syringe pump. Moreover, glass is rigid, so any potential deformation in a plastic syringe that can introduce alteration in the flow was prevented. A few strategies were adopted to get a tight seal between the glass syringe needle and plastic tubing. The diameter of the former was not thick enough for the tubing to fit firmly and liquid was observed to be leaking before reaching the chip. The successful solution to that was connecting the tubing directly to the syringe without the need for a needle, exploiting an adapter to get a tight seal. The glass syringe did not give any result either and no improvement in the setup was observed, so the experiments were continued with the plastic syringe.

After careful observation with the optical microscope, it was discovered that the electrodes were damaged. In particular, the middle one was always degraded (Figure 6.1a), then the damage tended to spread to neighboring ones as time went by (Figure 6.1b). That happened for all the test performed until then, so the absence of transitions was attributed to that. A first hypothesis for that was mechanical detaching due to flow friction, but that was quickly discarded as the damage would have been sustained by all the electrodes irrespective of their position. A second supposition was that electrodes underwent electrical damage from the applied voltage; that is the reason why the voltage was decreased down to values of 100 mV. That did not solve the issue, as the electrodes were still heavily damaged. A third hypothesis was that the electrode batch in use was defective to begin with.

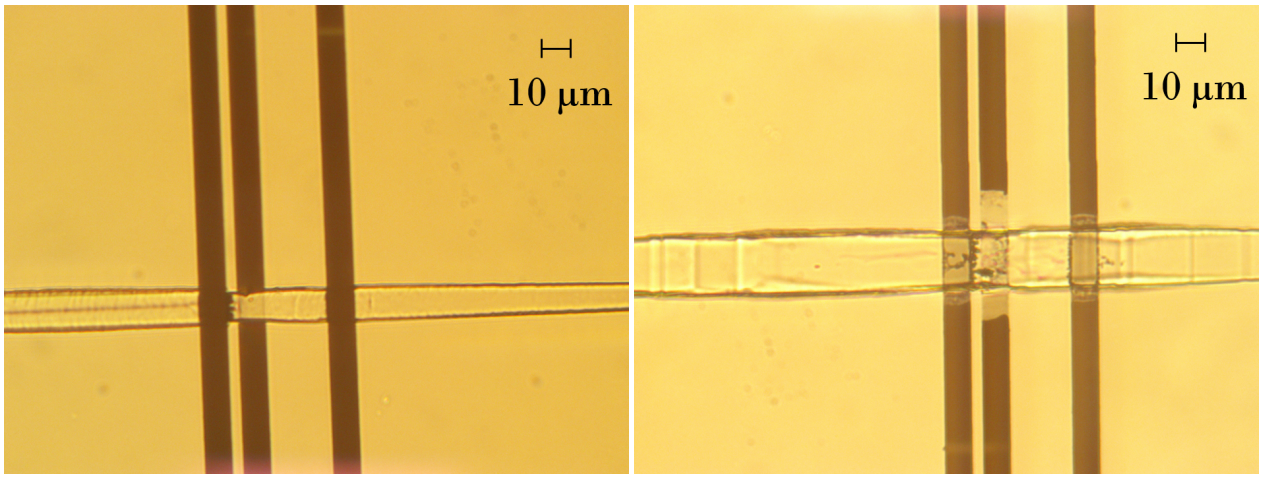

(a) (b)

Figure 6.1: Degradation of electrodes: the damaged started from the electrode to which voltage was supplied (a) and then spread to detection electrodes (b).

As the electrical motivation was thought to be the most plausible cause for the degradation of electrodes, the current flowing through the electrodes was reduced by decreasing the conductivity of the medium. That was achieved by diluting the solution with ultrapure (Milli-Q) water. A concentration of 1/20x PBS was employed and, at the same time, the ground from the impedance spectroscope was connected to the needle of the syringe, in order to ground the sample. A parameter that was not taken into consideration until then was the amplification of the TIA. It was set to 10k for the next tests. All of these corrections lead to the recording of transition signals: a plot for a single event was shown in Figure 5.6.

6.2 Analysis of extracted parameters

Once that transitions were identified in the current as a function time trace on the software provided by Zurich Instrument, the data was stored and analyzed with the MATLAB script introduced in section 5.4. Further filtering to the data was applied to tune the high frequency noise down without losing the characteristic frequencies of the signal: this was possible with a low-pass filter implemented in the MATLAB script for post-ptocessing of data, set at 2000 Hz.

For the moment, let us focus on a single transition: an overview on how it was analyzed is illustrated here. The graph for a single transition was showed in Figure 5.6. From the plot it is possible to calculate the velocity for the particle by remembering that the peak-to-peak time is needed to travel a known distance, i.e. 10 µm, corresponding to the middle of the first gap to the middle of the second gap. Due to the parabolic profile of a Poiseuille flow (see subsection 2.2.3), the velocity of a particle depends on its position along the height of the channel, therefore it is not equal for all particles and its value needs to be determined individually for each transition. By knowing the velocity of the particle, it is possible to rescale the entire x-axis in units of space, in order to replicate the output plots of COMSOL

simulations and make comparisons realistic.

The converted experimental transition plot representing the real part of the differential current as a function of space was imported in OriginPro and the same Gaussian fitting that was employed for simulated data was applied. A post-processed plot for the same single transition as Figure 5.6 is showed in Figure 6.2.

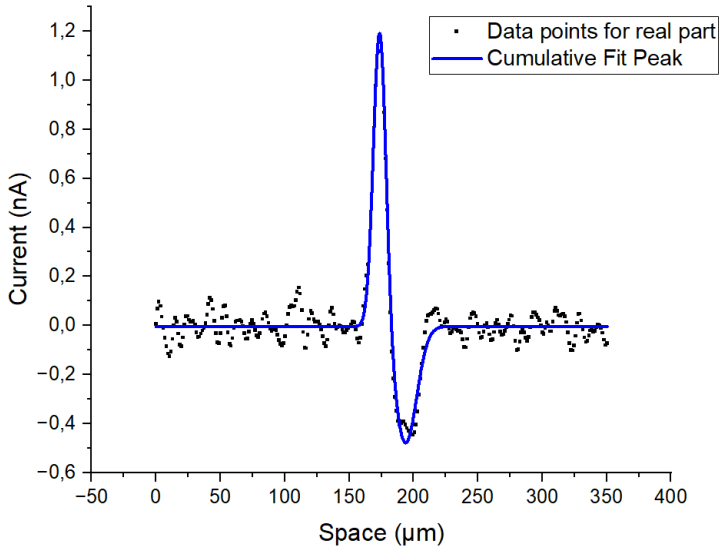

Figure 6.2: Transition of a particle fitted with a bipolar double Gaussian on OriginPro: the real part of the differential current is plotted as a function of space.

From such a graph, relevant parameters to determine W_r and H_r were extracted, so that comparison with simulated data could be achieved. W_r was defined as the ratio of the FWHM of negative and positive peak, while H_r was defined as the ratio of the magnitude of negative and positive peak.

The process described for a single transition was repeated for several events. A limited number of transitions had to be chosen for further analysis because the fitting procedure on OriginPro involves the individual treatment of each transition. The procedure was not optimized to handle more than a few 10s of events, hence, in an attempt to get an analysis with a limited degree of statistical relevance anyway, it was decided to take 20 arbitrarily chosen transitions into consideration.

The extracted values for W_r and H_r for the 20 transitions were plotted as function of the magnitude of the positive peak. As mentioned previously in subsection 3.3.3, the magnitude of the positive peak is equivalent to I_{diff} when the particle is in between electrode 1 and 2 along the length of the channel, so it will be referred to as I_{diff} in the following. The results are showed respectively in Figure 6.3 and Figure 6.4, where W_r was fitted with a linear relationship, while H_r was fitted with both a linear and a decaying exponential function.

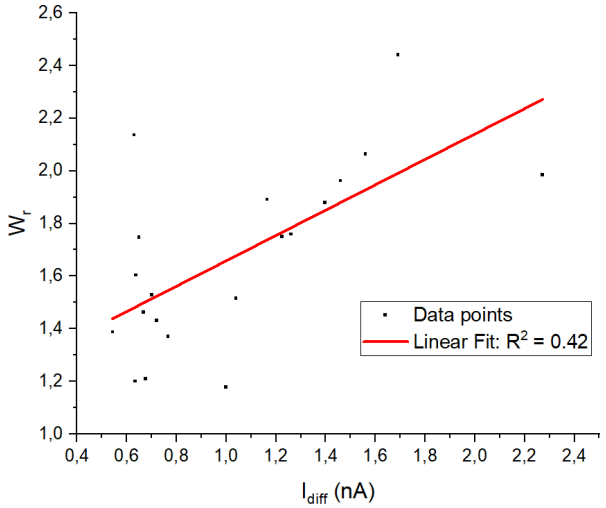

Figure 6.3: Experimental W_r as a function of I_{diff}, fitted with a linear function.

As can be seen in Figure 6.3, the distribution of data is not obvious for fitting purposes because points appear almost uniformly scattered in the plot. However, a linear relationship was revealed to be the most suited, leading to $R^2 = 0.42$. The fitting function is reported in Equation 6.1.

$$y = a + bx, \quad \text{where } y = W_r, \ x = I_{diff}, \ a = 1.18 \text{ and } b = 0.48. \tag{6.1}$$

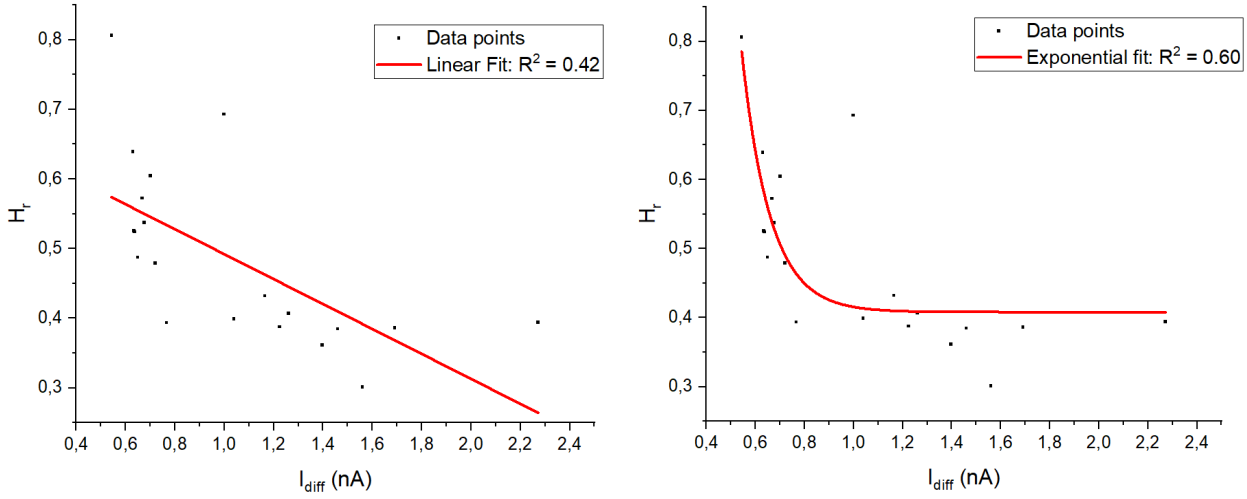

(a) (b)

Figure 6.4: Experimental H_r as a function of I_{diff}, fitted with (a) a linear function and (b) a decaying exponential function.

In analogy to Figure 6.3, H_r was fitted with a linear function as well (Figure 6.4a): that yielded the same value $R^2 = 0.42$. Nevertheless, a decaying exponential was found to

be better suited, with a value $R^2 = 0.60$ (Figure 6.4b). The fitting function is reported in Equation 6.2.

$$y = A_1 e^{-\frac{x}{t_1}} + y_0, \qquad \text{where } A_1 = 40.94,\ t_1 = 0.12 \text{ and } y_0 = 0.41. \tag{6.2}$$

Chapter 7

Discussion

In this Chapter, the complications encountered in setting up the experiments and achieving successful acquisition of data are discussed. Moreover, experimental IFC measurements are debated and a comparison with simulated data is presented. Improvements for future work are provided throughout the Chapter and further suggestions on the topic are given at the end.

7.1 Alignment optimization

The first issue encountered in the experimental setup was alignment between glass chip and PDMS slab. As shown in Figure 7.1, the IFC electrodes were designed long enough so that alignment was easily achieved by naked eye. It is not necessary for the channel to lie exactly in the middle of the electrodes length in the case of IFC, but particular care is needed in making sure that the channel is perpendicular to the electrodes as that may affect the registered signal. The influence of minimal rotational misalignment was not assessed. Nevertheless, the overall accuracy achieved was deemed sufficient for all IFC electrodes.

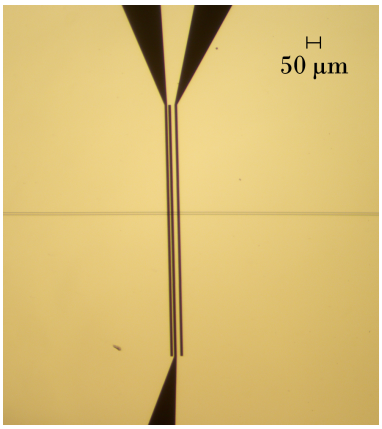

Figure 7.1: Alignment of IFC electrodes.

However, a more precise alignment is necessary in the case of EIS electrodes. As men-

tioned in subsection 4.5.1, the dimensions of the trap site are very small and, as a consequence, so are the electrodes: even a misalignment of 1 µm may cause the electrodes to lie in the wrong part of the channel and that can have a significant influence on the signal that is registered.

The effectiveness of the strategies adopted to facilitate alignment, i.e. the 3D-printed framework and the alignment marks, are here discussed. Without alignment marks on the glass chip and on the PDMS slab, the framework alone was not able to yield any successful alignment. The best result out of 10 trials is reported in Figure 7.2b: the correct alignment involves electrodes lying on the narrowest part of the trap site (Figure 7.2a), so the result is off by approximately 20 µm in the direction parallel to the main channel.

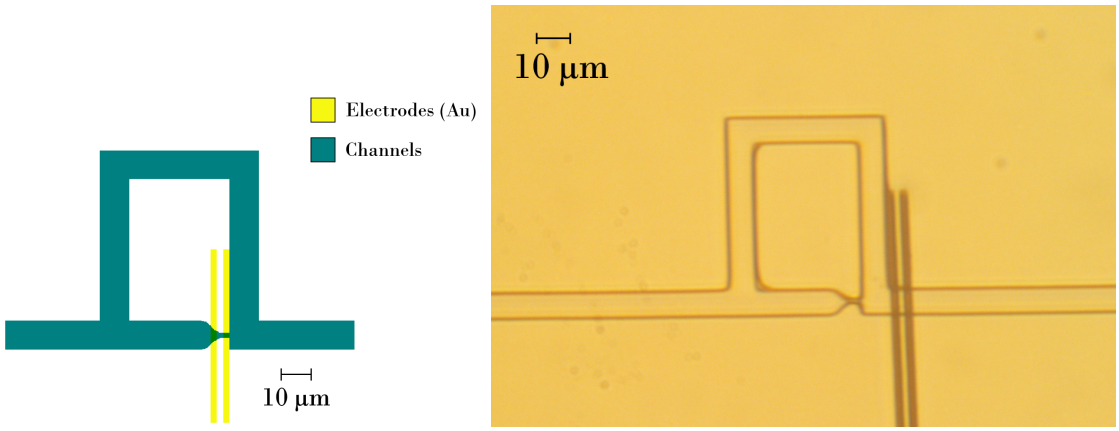

(a) (b)

Figure 7.2: Alignment of EIS electrodes without alignment marks: (a) sketch of target position and (b) obtained result.

One of the most critical aspects in aligning with the 3D-printed framework was pushing down the PDMS once that it looked correctly positioned through the microscope. This step was done by hand, therefore the pressure applied on the exposed surface of PDMS was not uniform nor constant. That may cause tilting of the PDMS slab in the framework, altering the relative position of glass and PDMS that was observed with the microscope before pushing the slab down. To improve this aspect, a mechanical system to lower the PDMS slab down may be helpful in preventing misalignment caused by unwanted tilting. A framework capable of moving the slab down perpendicularly to the glass could eliminate the issue of non-uniform pressure to which PDMS is subjected to when the procedure is done by hand. Moreover, all chips would be subjected to the same conditions, therefore the reproducibility of alignment would be improved.

Another issue was identified in the fact that it is not possible to obtain a perfectly focused image of PDMS and glass at the same time before they get in contact. The framework allows to place them in close proximity, down to approximately 0.5 µm, but that means that they are not on the same focus plane in any case. The problem is solved in part by decreasing the aperture of the microscope: in this way, the depth of field is increased, meaning that the thickness of the in-focus region extends. However, resolution is lost at the same time,

thus the edges of the features are less sharp. This represents an issue when fine tuning is required as in the case of alignment of EIS electrodes. To mitigate the focus inconvenience, the framework should be modified to allow the smallest possible distance between PDMS and glass before they adhere to each other.

In addition to the 3D-printed framework, a second expedient was introduced to guide the positioning of PDMS on the glass chip. Alignment marks were introduced on both parts of the chip, close enough to the critical features such as the trap sites. In this way, they were visible in the field of view of the optical microscope for which the design of the framework was based on. Significant improvements in alignment were observed: the combined strategies of alignment marks and 3D-printed frameworks yielded 3 successfully aligned chip out of 10 trials. Two of them are reported in Figure 7.3. It is possible to see that alignment was achieved even when two sets of EIS electrodes had to be aligned on the same trap design (Figure 7.3a). Unfortunately, successful alignment was accomplished in the last few weeks of the project, therefore time constraints prevented the acquisition of EIS data.

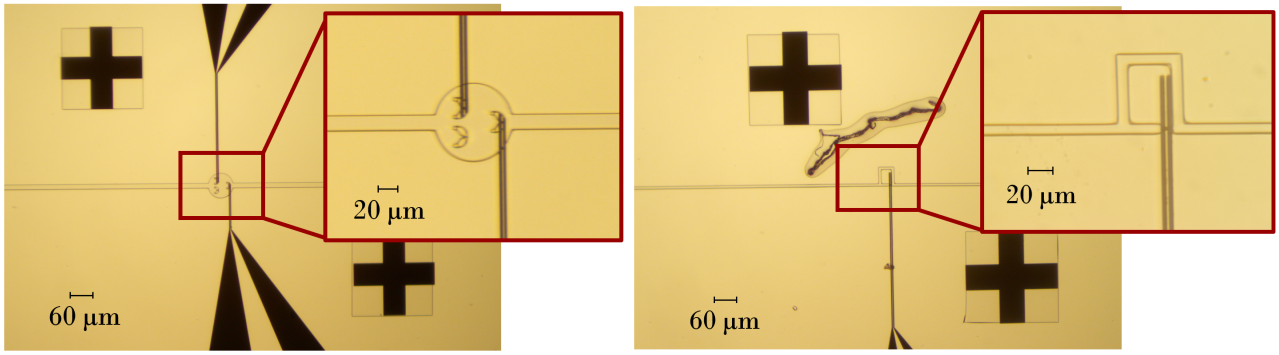

(a) (b)

Figure 7.3: Alignment of EIS electrodes with alignment marks: (a) trap site with two sets of EIS electrodes and (b) trap site with a single set of EIS electrodes. An impurity above the trap site is present in (b).

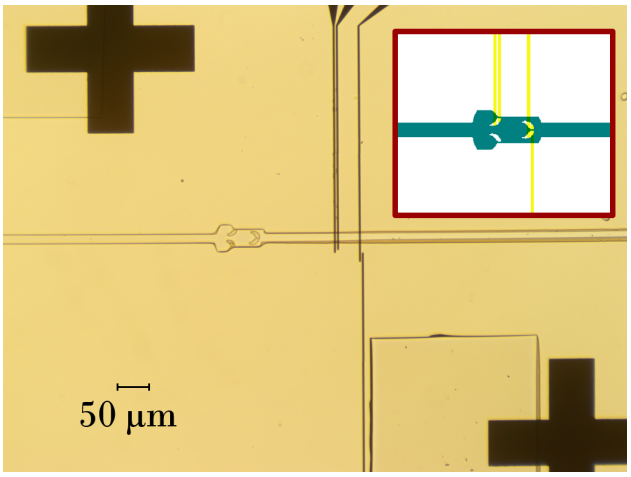

Figure 7.4: Unsuccessful positioning of EIS electrodes. An insertion with the target alignment is included.

Although the increase in success rate observed with the inclusion of alignment marks is evident, the method is far from being perfect. In the worst case scenario, alignment was off by approximately 150 µm in the direction parallel to the main channel (Figure 7.4). Despite lacking reliability and consistency in obtaining the desirable outcome, the addition of alignment marks is the recommended approach to achieve the correct positioning of PDMS channels on top of electrodes. The combination of alignment marks and an optimized 3D-printed framework is a promising strategy to obtain a correctly aligned working chip.

7.2 Degradation of electrodes

During experimental work, acquisition of particle transition data was heavily delayed: after attentive investigation, the main cause for that was attributed to electrode degradation. It was discovered that all the previously tested chips had undergone electrode degradation, which likely played a major role in the absence of events in the signal trace.

The motivation for electrode degradation was thought to be mechanical at first. The friction of flow on the metal may had provoked damage in the electrodes. However, if that was the case, all electrodes should have been ruined. It was observed that the first electrode to be degraded was the middle one, while the outer two looked fine at the beginning of experiments. Since the degradation of electrodes was uneven, the possibility of a mechanical cause was quickly disregarded.

After assessing that the first electrode to be damaged was always the one to which a voltage was being applied, an electrical cause was thought to be the most appropriate. However, reducing the voltage did not guarantee the integrity of gold. Degradation was not observed when the following three strategies were implemented at the same time.

1. The amplification of the TIA was increased to 10k.

2. The sample was grounded.

3. The conductivity of the sample was reduced by diluting the electrolyte solution.

Strategy 1 is unlikely to be the cause of electrode degradation, as the amplification step occurs after the signal has left the electrodes. That means that it should not affect the chip itself.

Strategy 2 and strategy 3 are both good candidates to have been the cause for electrode degradation. It is unsure if one strategy is more relevant than the other to prevent damage to the metal. After the first transitions were recorded with these settings, the grounding wire was disconnected from the needle of the syringe. No damage in the electrodes was observed after that, so, if the lack of grounding was the primary cause of degradation, grounding the sample before starting the experiment seems to be sufficient to prevent the issue. Conversely, if the main cause of degradation was the undiluted PBS solution, the experiments should be run again with not-grounded 1/20x PBS. The electrodes would not be subjected to degradation and the correct strategy to implement in order to avoid the issue would be identified to a fair degree of confidence.

7.3 IFC measurements

The main results yielded from experimental data of IFC measurements involving three coplanar electrodes with asymmetric gaps are gathered in Figure 6.3 and Figure 6.4. The most appropriate fitting for W_r was deemed to be a linear function, whose statistical strength in investigated in the first subsection. A comparison between experimental and simulation data is presented in the second subsection.

7.3.1 Statistical strength of linear correlation for experimental W_r

When assessing the statistical relevance of experimental plots, it is appropriate to draw conclusions on population and not just samples. The coefficient of determination R^2 gives information on the strength of a linear relationship in samples only, where in this case a sample is the dataset under analysis. If the sample is not statistically representative of the population, the value of R^2 can potentially be different when another sample is taken into account and therefore different conclusions may be drawn. When two samples taken from the same population yield inconsistent outcomes, the statistical strength of the samples is questionable and concerns about the reliability of conclusions arise.

The P-value is used to assess the statistical strength of a linear correlation in a sample: it quantifies the likelihood that the obtained data, i.e. W_r, occurred by chance if there was no actual correlation with the independent variable, i.e. I_{diff}, in the population. If the P-value is low, there is a high chance that a linear correlation between the variables exists, hence conclusions drawn from the fit are more likely to be reliable.

The calculation of P-value is achieved through the test statistic t^*, given by the formula

$$t^* = \frac{r\sqrt{n-2}}{\sqrt{1-R^2}}, \tag{7.1}$$

where $r = \sqrt{R^2}$ is the correlation coefficient, n is the number of data points, i.e. the number of transitions considered, and R^2 is the coefficient of determination. The P-value represents the probability of obtaining a test statistic t^* as extreme as the one observed, assuming there is no true correlation in the population. In particular, the P-value is determined by referring to a t-distribution with $n - 2$ degrees of freedom.

In the case of W_r as a function of I_{diff} obtained from experimental data and fitted with a linear relationship on OriginPro (Figure 6.3), the coefficient of determination is $R^2 = 0.42$. Using the statistical tools provided by MATLAB, the P-value was calculated to be 0.2%. This indicates that the probability to obtain $R^2 = 0.42$ if there was no correlation between W_r and I_{diff} is very low. Therefore, there is strong statistical evidence to support a linear correlation between W_r and I_{diff}.

Furthermore, a P-value of 0.2% for $n = 20$ supports the fair adequacy of the chosen number of transitions for analysis. For reference, the P-value would be approximately 23.7% for $n = 5$, indicating a much lower statistical significance and thus reducing the reliability of the results.

The validity of the P-value statistical test is limited to linear relationships. Since the best fit for H_r was determined to be a decaying exponential function (Figure 6.4b), an alternative method must be found to investigate the statistical strength of the relationship between H_r and I_{diff}. The alternative method should be equivalent to the P-value one, but applicable to exponential functions.

7.3.2 Comparison between simulated and experimental results

The dependence of the signal on the particle position along the height of the channel is intrinsic in IFC for a coplanar electrode configuration. The potential of extracted parameters W_r and H_r as a starting point for the development of a compensation strategy to mitigate this effect was demonstrated in subsection 3.3.3. In order to support this claim, the results based on COMSOL simulations must be compared with experimental data.

The experimental measurements described in Chapter 6 were conducted with particles of 2 µm in diameter. In order to allow for direct comparison, the curves of W_r and H_r as a function of I_{diff} for simulated beads with $r = 1$ µm were extracted from Figure 3.19 and fitted on OriginPro. The same fitting functions as the ones used for fitting of experimental data in Figure 6.3 and Figure 6.4b, i.e. a linear function for W_r and a decaying exponential function for H_r, were applied. The fitting for simulated data is shown in Figure 7.5.

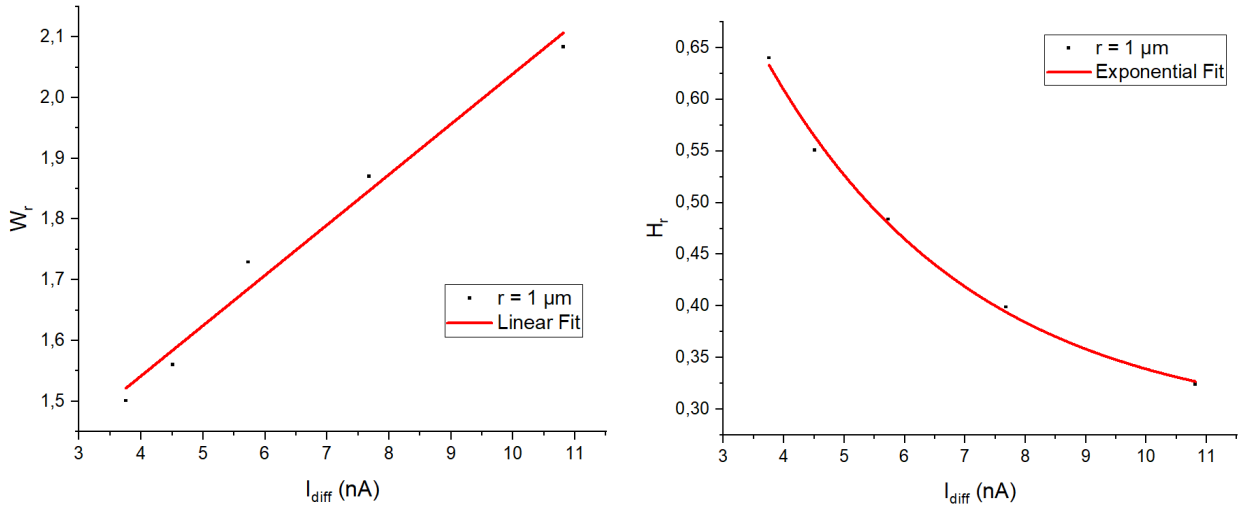

(a) (b)

Figure 7.5: Selected parameters as function of I_{diff} for a simulated bead with different radius $r = 1$ µm: (a) $W_r(zc)$ and (b) $H_r(zc)$. Data are extracted from COMSOL simulations and fitted on OriginPro.

It is possible to notice that the behavior of the curves for simulated data is the same as the one reported in Figure 6.3 and Figure 6.4b for experimental data. Simulations and experiments show good agreement in the trends of W_r and H_r as functions of I_{diff}.

With reference to the fitting functions Equation 6.1 and Equation 6.2, a direct comparison of the fitting parameters for simulated and experimental data is reported in Table 7.1, respectively.

Table 7.1: Comparison of fitting parameters: (a) W_r and (b) H_r.

Fitting parameter	Simulated data	Experimental data
a	1.21	1.18
b	0.08	0.48

(a) Linear fit for W_r.

Fitting parameter	Simulated data	Experimental data
A_1	1.05	40.94
t_1	3.44	0.12
y_0	0.28	0.41

(b) Exponential fit for H_r.

As mentioned previously, the behavior of W_r and H_r as functions of I_{diff} is consistent in

simulated and experimental data. However, discrepancies are observed in the corresponding fitting parameters. Several factors may contribute to this.

First of all, the fitting method itself introduces an approximation. By definition, fitting data with a mathematical function is inherently an estimation and it should not be considered as an exact representation of the data. This is evident when fitting both simulated and experimental IFC signals with a bipolar double Gaussian (e.g. Figure 3.16 and Figure 6.2): when looking at data points, the negative peak appears to be composed by two sub-peaks and this feature is not captured by the fitting function. Such approximation may influence the accuracy of extracted peak parameters, such as FWHM and peak magnitude, which are used to calculate W_r and H_r, respectively.

Secondly, only 20 transitions were considered in the experimental analysis. Including a larger number of events could lead to different fitting parameters, besides improving statistical reliability. To extend the current study, it may be beneficial to take more transitions into account and refine the fitting method to enable the simultaneous analysis of a greater number of transitions.

Finally, it is worth highlighting that the range of I_{diff} is different for simulated and experimental data, as can be concluded by inspecting and comparing Figure 7.5a and Figure 6.3. The differential current is approximately one order of magnitude lower in experiments, which is unexpected considering that a higher voltage was applied with respect to simulations. One of the reasons for this may be related to the current amplification step in the TIA, as it is not clear how it treated by the software. Another reason for the inconsistent current ranges may reside in how the differential current is computed. It was discovered late in the project that simulation and experimental setups likely adopt different procedures for this calculation. In simulations, the real part of the current at each detection electrode is stored separately and then the differential current is obtained by subtracting these values. Conversely, the Zurich Instruments software used for experimental data acquisition is speculated to first compute the difference between the currents at the two electrodes and then extract the real part. For further investigation on this topic, more research on the current computation method employed for the impedance spectroscope is recommended. If speculations are confirmed, simulations should eventually be repeated in order to allow for the evaluation of the differential current using a method aligned with the way in which it is calculated in the experimental setup.

Despite discrepancies in the fitting parameters, the overall trends for both W_r and H_r as functions of I_{diff} reported in Figure 7.5 for simulated data are compliant with experimental results. While further investigation is needed to strengthen the experimental validation of simulation outcomes, the current findings are encouraging. W_r and H_r appear to be promising parameters as a foundation for the development of a compensation strategy to the signal dependence on particle position along the height of the channel in an IFC setup with coplanar electrodes.

7.4 Further recommendations for future work

Possible improvements for the experimental setup and suggestions for future work have been provided throughout the Chapter. The main aspects are summarized here and additional recommendations are given.

Regarding the experimental setup, difficulties were encountered in monitoring the experiments under the optical microscope due to the holder hosting the chip not being securely fixed to the microscope plate. Plastic tubing connecting the chip to the syringe and electrical wires for the spectroscope were the cause for the challenging handling of the holder. To address this issue, it would be beneficial to design a custom support ensuring stable positioning of the holder under the objective lens, possibly involving clamping of the holder to the microscope plate. This would stabilize the chip and allow for an easier observation of the magnified channels.

One of the first complications that delayed the acquisition of experimental data was the introduction of samples in the chip. To ease the flow into the channel, it is suggested to modify its design close to the inlet hole. For instance, a funnel shape would avoid a sudden change in hydraulic resistance from plastic tubing to microchannel, facilitating the injection of the solution. In this way, particles would not accumulate at the inlet and clogging may be less likely.

A glass syringe has a smaller inner diameter than a plastic one, hence it would allow for a finer tuning of the flow rate injected with the pump. However, with such a tool, the connection of the sample with the grounding wire form the spectroscope was not achievable. Since grounding of the sample seemed to be very important for the successful acquisition of data, a method to ground the liquids in the glass syringe would be beneficial and could be implemented for a finer control of flow rates.

Concerning the mitigation of the signal dependence on the particle position along the height of the channel when coplanar electrodes are employed for IFC measurements, further investigation should be carried out on the parameters W_r and H_r to asses their relevance. First of all, the method used for the calculation of the differential current in the Zurich Instruments software must be determined to allow for solid comparison with simulations.

Then, a larger number of transitions should be analyzed to increase the statistical relevance of experimental findings. A number of 20 was chosen for this thesis due to the fitting procedure not being optimized for the simultaneous handling of several transitions. Improving this aspect would make data analysis faster and more efficient.

In the context of future research on the topic, another important consideration is that only 2 µm beads were experimentally tested in this project. The conclusions drawn from experimental data are therefore limited and the acquisition of data for particles of different sizes should be pursued. If asymmetric gaps turn out to be unsuccessful in providing information on the position of the particles along the height of the channel, more electrodes geometry must be tested out .

Chapter 8

Conclusion

The primary objective for this project was to design a coplanar electrode layout for IFC that is capable of minimizing the signal dependence on the particle position within the microfluidic channel. This is the main issue of a coplanar configuration and a compensation strategy for such dependence can improve the performance of a layout that is more easily fabricated than a front-facing one. Additionally, the project aimed at the development of a functional experimental setup for IFC. This involved the design of a holder for the device to ensure support and connections to the equipment needed, in addition to an alignment and bonding process able to yield efficacious chips. The final goals of the project were the testing of the designed setup and the validation of simulation results through experimental measurements.

The optimization of the electrode layout was addressed through COMSOL simulations, yielding preliminary but valuable insights. A three-electrode symmetric design was explored at first: the optimal geometry was found to involve 10 µm wide electrodes separated by 5 µm gaps. This layout guarantees the best performance in terms of magnitude of the differential current according to simulations. However, no attenuation of the position dependence of the signal was observed when simply modifying widths of electrodes and gaps in a symmetric configuration. Afterwards, investigations into the impact of asymmetric electrode widths and gaps were conducted. While varying the electrode widths was inconclusive, introducing asymmetric gaps demonstrated potential for the mitigation of the positional dependence of the IFC signal. Two parameters, W_r and H_r, extracted from a double Gaussian fit of the differential current and related to FWHM and magnitude of the peaks, respectively, were identified as promising indicators of the particle position. Their independence on the size of the bead was successfully observed when comparing results for 1 µm and 2 µm beads.

Experimental validation of the simulation results was partially achieved. Although direct confirmation of the simulated outcomes was not possible, the trends observed for W_r and H_r in experimental data aligned well with those predicted in simulations. This suggests that the extracted parameters could indeed serve as reliable indicators of particle height. However, only one particle size was tested, i.e. beads with a 2 µm diameter, and no bacterial measurements were conducted due to time constraints. The conclusions drawn on the polystyrene beads employed in this project are not definitive, but rather may serve as a starting point for further research and development. To generalize and solidify the findings,

testing with multiple particle sizes and bacterial samples has to be investigated. Moreover, a bigger amount of transitions should be analyzed for statistical relevance; in order to do so, the optimization of the fitting procedure for experimental data so that multiple transitions can be investigated simultaneously has to be pursued.

The development of an actual compensation strategy was not achieved: further effort has to be put on the matter. However, W_r and H_r have shown promising result at being indicators for the position of the particle along the height of the channel. If they can be demonstrated to be independent on the particle size, a correction factor to be applied in the post-processing of data can be conceived. In this way, the compensation of the positional-dependence of the signal may be achieved.

The construction of the experimental setup presented several challenges. Despite this, a functional holder for the chip was successfully developed, ensuring both electrical connections and fluidics integration. The chip bonding process was also optimized: while initial attempts using mechanical pressure were insufficient as the sample was observed to be leaking, oxygen plasma bonding provided effective sealing of the PDMS slab to the glass chip.

The 3D-printed framework for the alignment of electrodes and PDMS, although not yet fully reliable, showed encouraging results when used in combination with alignment marks. With further refinement, the process could be made more consistent. Unfortunately, due to time limitations, EIS measurements could not be performed, as successful alignment, which is essential in the trap site, was only achieved at the very end of the project.

Overall, the project addressed the simulation and experimental integration goals to a reasonable extent, providing initial insight into the potential for reducing signal dependence on particle position in IFC. While encouraging trends were observed, a complete and validated compensation strategy is yet to be developed. Key points such as testing with bacteria and reliable, consistent alignment of PDMS and electrodes remain outstanding as well. Nonetheless, the results offer a useful starting point and indicate directions for further development of an efficient coplanar electrode configuration involving asymmetric gaps.

List of Figures

List of Tables

Nomenclature

E. coli *Escherichia coli*

DRIE Deep Reactive Ion Etching

ECM Equivalent Circuit Model

EIS Electrochemical Impedance Spectroscopy

FEM Finite Element Method

FWHM Full Width Half Maximum

IFC Impedance Flow Cytometry

LIA Lock-In Amplifier

LOC Lab-On-a-Chip

PBS Phosphate Buffered Saline

PCB Printed Circuit Board

PDE Partial Differential Equation

PDMS PolyDiMethylSiloxane

SNR Signal-to-Noise Ratio

TIA TransImpedance Amplifier

Bibliography

[1] J. B. Kaper, J. P. Nataro, and H. L. Mobley, "Pathogenic escherichia coli," 2 2004.

[2] G. Ekici and E. Dümen, *Escherichia coli and Food Safety*. 5 2019.

[3] V. M. Cardoso, G. Campani, M. P. Santos, G. G. Silva, M. C. Pires, V. M. Gonçalves, R. de C. Giordano, C. R. Sargo, A. C. Horta, and T. C. Zangirolami, "Cost analysis based on bioreactor cultivation conditions: Production of a soluble recombinant protein using escherichia coli BL21(DE3)," *Biotechnology Reports*, vol. 26, 6 2020.

[4] A. Mandal, "Further reading all flow cytometry content using flow cytometry in disease diagnosis flow cytometry and drug discovery using flow cytometry in biomarker detection flow cytometry methodology, uses, and data analysis," 2023.

[5] K. M. McKinnon, "Flow cytometry: An overview," *Current Protocols in Immunology*, vol. 2018, pp. 5.1.1–5.1.11, 2 2018.

[6] K. Cheung, S. Gawad, and P. Renaud, "Impedance spectroscopy flow cytometry: On-chip label-free cell differentiation," *Cytometry Part A*, vol. 65, pp. 124–132, 6 2005.

[7] C. V. Bertelsen, "Screening of bacteria using impedance flow cytometry," PhD thesis, 2021.

[8] F. Caselli, P. Bisegna, and F. MacEri, "Eit-inspired microfluidic cytometer for single-cell dielectric spectroscopy," *Journal of Microelectromechanical Systems*, vol. 19, pp. 1029–1040, 10 2010.

[9] F. Caselli, M. Shaker, L. Colella, P. Renaud, and P. Bisegna, "Modeling, simulation, and performance evaluation of a novel microfluidic impedance cytometer for morphology-based cell discrimination," *Journal of Microelectromechanical Systems*, vol. 23, pp. 785–794, 2014.

[10] F. Caselli, A. D. Ninno, R. Reale, L. Businaro, and P. Bisegna, "A novel wiring scheme for standard chips enabling high-accuracy impedance cytometry," *Sensors and Actuators, B: Chemical*, vol. 256, pp. 580–589, 3 2018.

[11] N. Demierre, T. Braschler, P. Linderholm, U. Seger, H. V. Lintel, and P. Renaud, "Characterization and optimization of liquid electrodes for lateral dielectrophoresis," *Lab on a Chip*, vol. 7, pp. 355–365, 2007.

[12] A. D. Ninno, V. Errico, F. R. Bertani, L. Businaro, P. Bisegna, and F. Caselli, "Coplanar electrode microfluidic chip enabling accurate sheathless impedance cytometry," *Lab on a Chip*, vol. 17, pp. 1158–1166, 3 2017.

[13] H. Wang, N. Sobahi, and A. Han, "Impedance spectroscopy-based cell/particle position detection in microfluidic systems," *Lab on a Chip*, vol. 17, pp. 1264–1269, 4 2017.

[14] T. Tang, X. Liu, R. Kiya, Y. Shen, Y. Yuan, T. Zhang, K. Suzuki, Y. Tanaka, M. Li, Y. Hosokawa, and Y. Yalikun, "Microscopic impedance cytometry for quantifying single cell shape," *Biosensors and Bioelectronics*, vol. 193, 12 2021.

[15] R. Reale, A. D. Ninno, L. Businaro, P. Bisegna, and F. Caselli, "High-throughput electrical position detection of single flowing particles/cells with non-spherical shape," *Lab on a Chip*, vol. 19, pp. 1818–1827, 5 2019.

[16] A. Farooq, N. Z. Butt, and U. Hassan, "Biochip with multi-planar electrodes geometry for differentiation of non-spherical bioparticles in a microchannel," *Scientific Reports*, vol. 11, 12 2021.

[17] *Size limits of very small microorganisms : proceedings of a workshop*. National Academy Press, 1999.

[18] Y. Feng, L. Huang, P. Zhao, F. Liang, and W. Wang, "A microfluidic device integrating impedance flow cytometry and electric impedance spectroscopy for high-efficiency single-cell electrical property measurement," *Analytical Chemistry*, vol. 91, pp. 15204–15212, 12 2019.

[19] C. D. Chin, V. Linder, and S. K. Sia, "Lab-on-a-chip devices for global health: Past studies and future opportunities," 2007.

[20] E. Team, "Lab-on-a-chip 2024: review, history and future," *Elveflow*, 8 2023.

[21] D. Wartmann, M. Rothbauer, O. Kuten, C. Barresi, C. Visus, T. Felzmann, and P. Ertl, "Automated, miniaturized, and integrated quality control-on-chip (QC-on-a-chip) for cell-based cancer therapy applications," 9 2015.

[22] "Release history." `https://www.comsol.com/release-history`.

[23] C. Bertelsen, "Using impedance spectroscopy for antibiotic susceptibility testing," Master Degree thesis, 2014.

[24] H. Bruus, *Theoretical Microfluidics*. Oxford University Press Inc., 2008.

[25] S. K. A. Al-Amshawee and M. Y. B. M. Yunus, "Electrodialysis membrane with concentration polarization – a review," 1 2024.

[26] G. E. Skands, C. H. Clausen, and W. E. Svendsen, "Differentiation of bacteria and non-biological particles in drinking water using impedance flow cytometry," Master Degree thesis, 2014.

[27] D. D. Carlo, D. Irimia, R. G. Tompkins, and M. Toner, "Continuous inertial focusing, ordering, and separation of particles in microchannels," 2007.

[28] S. Mishra, N. K. Singh, and V. Rousseau, "Display interfaces," *System on Chip Interfaces for Low Power Design*, pp. 53–126, 1 2016.

[29] H. Morgan, T. Sun, D. Holmes, S. Gawad, and N. G. Green, "Single cell dielectric spectroscopy," in *Journal of Physics D: Applied Physics*, vol. 40, pp. 61–70, 1 2007.

[30] K. D. Young, "The selective value of bacterial shape," *Microbiology and Molecular Biology Reviews*, vol. 70, pp. 660–703, 9 2006.

[31] S.-M. Lee, "Atomic layer deposition on biological matter," PhD thesis, 2009.

[32] A. J. Bard and L. R. Faulkner, *Electrochemical methods : fundamentals and applications*. John Wiley & Sons, Inc., 2001.

[33] L. Jiang, D. Li, X. Xie, D. Ji, L. Li, L. Li, Z. He, B. Lu, S. Liang, and J. Zhou, "Electric double layer design for Zn-based batteries," *Energy Storage Materials*, vol. 62, p. 102932, 9 2023.

[34] G. C. Barker, "The equivalent circuit for the electrical double layer," *Journal of electroanalytical chemistry*, 1966.

[35] C. Bao, H. Zhu, and J. Liu, "Introduction of parasitic capacitance and methods of reducing its capacitance," *Applied and Computational Engineering*, vol. 85, pp. 141–147, 7 2024.

[36] R. Ho, "Non-invasive determination of bacterial single cell properties by electrorotation," 1999.

[37] W. Olthuis, W. Streekstra, and P. Bergveld, "Theoretical and experimental determination of cell constants of planar-interdigitated electrolyte conductivity sensors," 1995.

[38] "Origin help - Gauss." `https://www.originlab.com/doc/origin-help/gauss-fitfunc`.

[39] "Origin help - ExpDec1." `https://www.originlab.com/doc/Origin-Help/ExpDec1-FitFunc`.

[40] "Origin help - ExpGro1." `https://www.originlab.com/doc/Origin-Help/ExpGro1-FitFunc`.

[41] E. Team, "PDMS: A review," *Elveflow*, 2 2021.

[42] N. Haandbæk, K. Mathwig, R. Streichan, N. Goedecke, S. C. Bürgel, F. Heer, and A. Hierlemann, "Bandwidth compensation for high resolution impedance spectroscopy," in *Procedia Engineering*, vol. 25, pp. 1209–1212, 2011.

[43] V. Markel and V. A. Markel, "Introduction to the Maxwell Garnett approximation: tutorial," *Journal of the Optical Society of America. A Optics, Image Science, and Vision*, vol. 33, pp. 1244–1256, 2016.

[44] D. Holmes, D. Pettigrew, C. H. Reccius, J. Gwyer, C. V. Berkel, J. Holloway, D. Morganti, D. E. Davies, and H. Morgan, "Supplementary information for leukocyte analysis and differentiation using high speed microfluidic single cell impedance cytometry," *The Royal Society of Chemistry*, 2009.

Appendix A

Mathematical model

A.1 Maxwell Garnett mixing formula

In principle, a complete description of the dielectric properties of a suspension of diluted homogeneous spherical particles (here referred to as "inclusions") can be obtained with the Maxwell Garnett mixing formula, which states that the complex permittivity ϵ_{MG} of the suspension is calculated as [43]

$$\epsilon_{MG} = \epsilon_h \frac{1 + 2f\dfrac{\epsilon_i - \epsilon_h}{\epsilon_i + 2\epsilon_h}}{1 - f\dfrac{\epsilon_i - \epsilon_h}{\epsilon_i + 2\epsilon_h}}, \tag{A.1}$$

where ϵ_h is the complex permittivity of the host medium, ϵ_i is the complex permittivity of the inclusions and f is the volume fraction of the inclusions to the detection volume. When the suspended particles are more complex and consist of a core surrounded by a shell, an effective inclusion permittivity $\epsilon_{i,eff}$ can be derived as [44]

$$\epsilon_{i,eff} = \epsilon_{mem} \frac{\left(\dfrac{R}{R-d}\right)^3 + 2f\dfrac{\epsilon_c - \epsilon_{mem}}{\epsilon_c + 2\epsilon_{mem}}}{\left(\dfrac{R}{R-d}\right)^3 - f\dfrac{\epsilon_c - \epsilon_{mem}}{\epsilon_c + 2\epsilon_{mem}}}, \tag{A.2}$$

where ϵ_{mem} and ϵ_c are the complex permittivity of the particle membrane and of the particle core respectively, R is the radius of the particle and d is the thickness of the shell. This allows the extension of the Maxwell Garnett approximation to include shelled inclusions as well.

Knowing the complex permittivity of the suspension, it is then possible to calculate the capacitance C_{susp} for a set of two front-facing electrodes with area A separated by a distance l as

$$C_{susp} = \epsilon_0 \epsilon_{MG} \frac{A}{l}, \tag{A.3}$$

where ϵ_0 is the vacuum permittivity. The complex impedance response of the system is given by

$$Z_{susp} = \frac{1}{j\omega C_{susp}}, \tag{A.4}$$

where ω is the angular frequency of the current and j is the imaginary unit.

In the case of coplanar electrodes, the calculation of C_{susp} is challenging and not as straightforward, therefore exploiting an equivalent circuit model is the most convenient alternative to relate impedance response and electrical properties of the suspension.

Appendix B

Extra simulation output

B.1 W_d and H_d

Additional parameters to be extracted from the graphs of I_{diff} as a function of xc (e.g. Figure 3.16) for multiple zc positions were W_d and H_d, defined as

$$W_d = (\text{FWHM of negative peak}) - (\text{FWHM of positive peak}) \tag{B.1}$$

$$H_d = (\text{Magnitude of negative peak}) - (\text{Magnitude of positive peak}). \tag{B.2}$$

Their dependence on zc for various bead sizes is depicted in Figure B.1b.

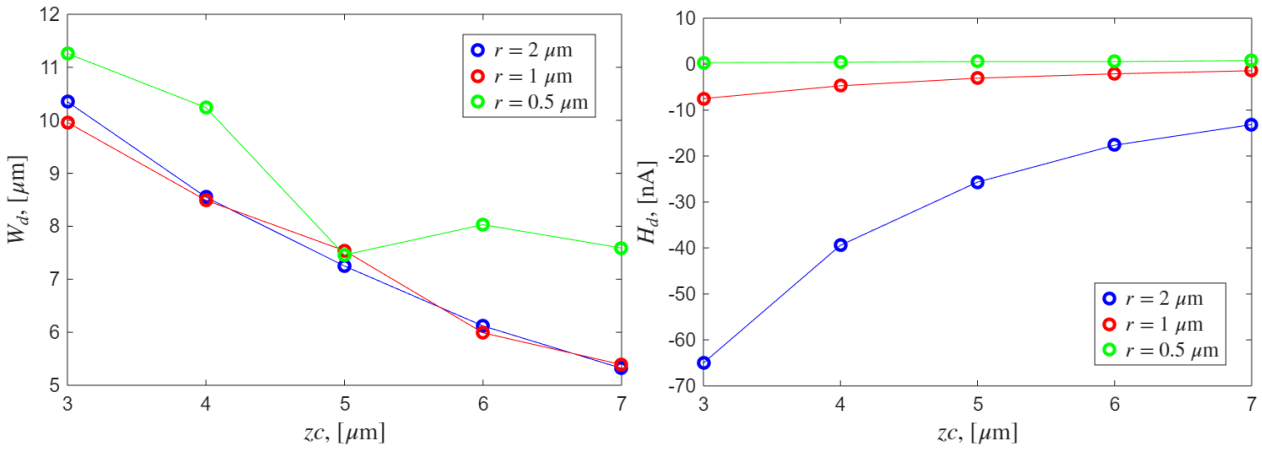

(a) (b)

Figure B.1: Additional parameters as function of zc for a bead with different radii ($r = 0.5$ µm, $r = 1$ µm, $r = 2$ µm): (a) $W_r(zc)$ and (b) $H_r(zc)$.

B.2 $I_{diff}(xc)$ for different bead size

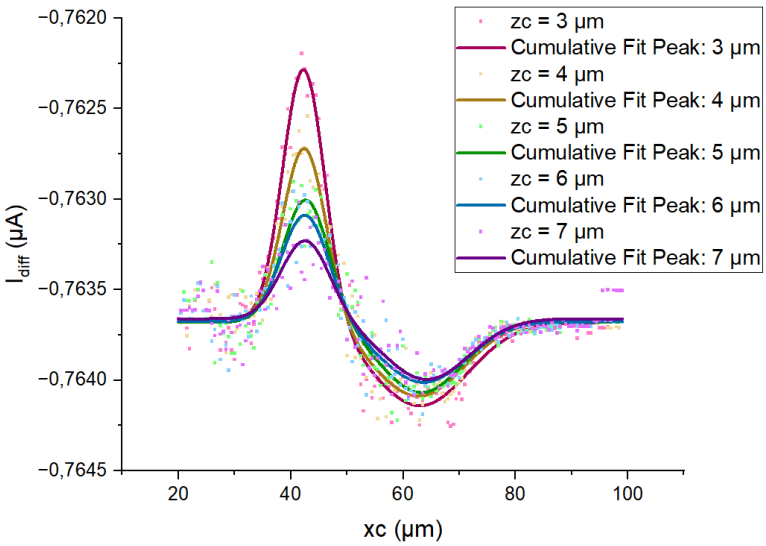

Figure B.2: I_{diff} as a function of xc for multiple values of zc for a bead with $r = 0.5$ µm.

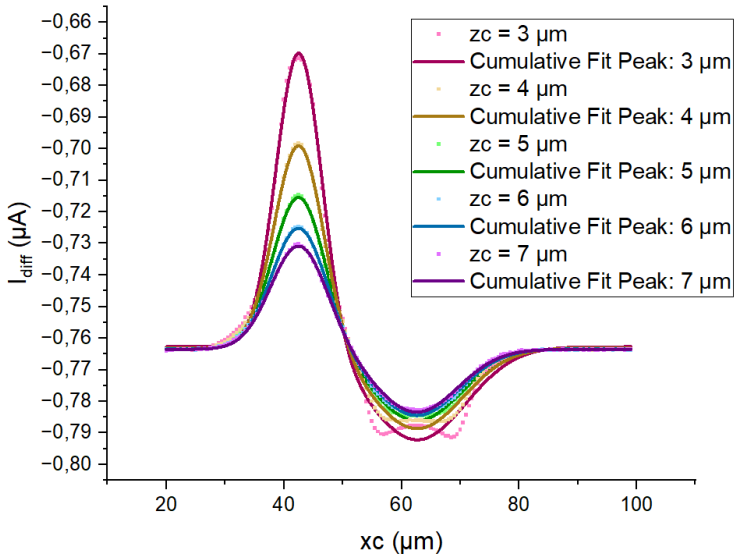

Figure B.3: I_{diff} as a function of xc for multiple values of zc for a bead with $r = 2$ µm.

Appendix C

Process flows and protocols

Detailed process flows and protocols for the fabrication of all chip components are included here.

C.1 Electrode process flow

Step	Heading	Equipment	Procedure	Comments
1	**Preparation**			
1.1	Wafer selection	Wafer box	Boron glass - Labmanager: SB616	
2	**Exposure**			
2.1	Photoresist deposition	Spin coater: Gamma UV	AZ 5214E (positive) Thickness=1.5µm	3411 - DCH 100mm 5214E 1,5um HDMS
2.2	UV Exposure	Aligner: Maskless 01	λ=365nm; Dose=110mJ/cm^2; Defocus=0	Design: SDP_maskrunX.cif Mode: Fast
3	**Development**			
3.1	TMAH development	Developer: TMAH UV-lithography	Develop: SP TMAH for 60s	Recipe 1002 DCH 100mm SP60s
4	**Metal dep & Lift-off**			
4.1	Metallization	E-beam evaporator (Temescal)	Ti: 10nm at 2Å/s Au: 150nm at 5Å/s	
4.2	Lift-off	Lift-off	Remover 1165 Δt = 30-55 min at rough 9	After lift-off: 5min in IPA at rough 9 + water rinse + dry
5	**Cut**			
5.1	Cut	DAD 321 Dicing Saw	Cuts in CH1: 4 x 20 mm Cuts in CH2: 4 x 20 mm	Blade height 0.15 mm

C.2 Si mold process flow

Step	Heading	Equipment	Procedure	Comments
1	**Preparation**			
1.1	Wafer selection	Wafer box	Silicon 4" wafers SSP SN629	Orientation<100> Expected thickness: 525 ±20 µm
2	**Exposure**			
2.1	Photoresist deposition	Spin coater: Gamma UV	AZ nLOF 2020 (negative) Thickness=1.5µm	2411 – DCH 100mm nLOF 2020 1.5µm HMDS
2.2	UV Exposure	Aligner: Maskless 01	λ=365nm; Dose=180mJ/cm^2; Defocus=0	Design: SDP_maskrunX.cif Mode: Quality
3	**Development**			
3.1	PEB+TMAH development	Developer: TMAH UV-lithography	Post exp bake 60s @110°C Develop: TMAH for 60s	Recipe 3001 DCH 100mm PEB60s@110C SP60s
4	**Dry etching and resist strip**			
4.1	Dry etching	PEG-1	Process D4 2 min	
4.2	Resist strip	Plasma Asher		
5	**Molecular vapor deposition**			
5.1	FDTS deposition	MVD	Stamp2NP	Multi layer

C.3 PDMS protocol

- **Mixing**: weigh liquid polymer and curing agent with ratio 10:1 on a scale inside a fume hood. The same disposable plastic container is used for the two components. Stir gently to limit incorporation of air.
- **Pouring**: the obtained mixture is poured onto the Si wafer mold. Place the wafer inside a custom 3D-printed circular holder (Figure C.1) and pour the mixture on top of it, possibly in the middle of the wafer for best homogeneity. To be performed in a fume hood.

Figure C.1: 3D-printed circular holder hosting a Si wafer with diameter 100 mm: liquid PDMS is ready to be poured on top.

- **Desiccation**: place the circular holder in a desiccator and open vacuum suction. Leave it there until bubbles have significantly reduced (at least 1 hour). Make sure to close vacuum suction when opening the desiccator and perform it under a ventilation tube. Detach the tubing from the desiccator slowly, to avoid sudden change in pressure inside the chamber by letting it vent.
- **Curing**: place the circular holder in an oven at 60 °C for 3 hours. Remove it from the oven and let it cool down before cutting the solidified PDMS with a scalpel.

Appendix D

Project plan

D.1 Project description

In this project, a device for the electrical characterization of bacteria will be developed. The aim will be the maximization of signal-to-noise ratio (SNR) in an impedance flow cytometry design (IFC), where the electric field between two or more electrodes is perturbed by a particle passing through: such variation in signal can be analysed to extract information on the particle. When a set of coplanar electrodes is employed, the intrinsic issue for this characterization technique is the dependence of the signal on the particle position inside the channel, which can lead to misinterpretation of results; in order to account for it, the electrodes will be optimized by changing the dimensions and trying out different configurations. Finite element method simulations will be carried out in the software COMSOL, then the device will be fabricated in the cleanroom (Sara Di Paolo MSc project) and the experimental setup to perform measurements will be built in a laboratory. In particular, the holder for the device and the mold for the PDMS part that seals it will be 3D printed. All of the preliminary studies will be conducted on simple plastic beads, then different shapes will be tested out in COMSOL and finally bacteria (Escherichia coli) will be analyzed: electrical characterization on a full frequency spectrum performed on single trapped particle may yield relevant information on the flow of particles and their dielectric properties, besides being useful in determining the correct frequencies to employ in the fixed-frequency flow analysis, which, in turn, allows the investigation of many particles at the same time. The combination of the two techniques yields a more comprehensive inspection of the flow and its dielectric properties, which can be useful for the counting and characterization of cells in bioreactors.

D.2 Objectives and costs

The main aim of the project will be the electrical characterization of simple beads and bacteria, minimizing the effect of particle position in the channel on the output signal. Assuming that all previously existing lab equipment (e.g.: impedance spectroscope) works properly, no major concern regarding costs arises; nevertheless, expenses will be discussed

with the supervisors as the project moves forward.

D.3 Applied techniques

- Microfluidics simulations on COMSOL: finite element modelling will be exploited in order to predict the performances of the proposed chip designs.
- 3D printing design on Autodesk Fusion: the software will be employed for the design of the holder for the chip and the mold for the PDMS channels.
- CleWin6: computer-aided design will be employed for the masks needed for chip fabrication.
- Data analysis will be performed on MATLAB and Origin Pro.
- All relevant data and files will be stored on Microsoft Teams.

D.4 Work plan

- Literature study: week 1-2 (03/02 - 16/02)

  A literature study will be conducted in the first part of the project, which will include research on impedance flow cytometry and different geometrical optimizations and configurations of coplanar electrodes. In particular, articles study will be focused on the influence of particles shape and position in the microfluidic channel on the output signal.

- Design: week 2-14 (10/02 - 09/05)

  COMSOL simulations will be performed to determine the most suitable design for coplanar electrodes. Autodesk Fusion will be employed to design the mold for the PDMS part of the device and the device holder, while CleWin6 will serve to design the chips for fabrication. The first designs ready for fabrication will be available at the end of February. In this phase, several designs will be tried and tested; at the end of the period, the final design of the chip should be ready.

- Lab work: week 5-18 (03/03 - 06/06)

  The experimental setup, which includes a microscope, a current amplifier, an impedance spectroscope, a syringe pump and a computer, will be assembled in DTU facilities. Additionally, in this time span, the 3D designs will be printed and the device will be fabricated (Sara Di Paolo). The PCB is going to be designed as well, according to the final design of the chip, and ordered from an external provider (estimated delivery time: 1 week approx.). Then, the measurements will take place, firstly with simple beads and then with bacteria. The first tests on the chips will start approximately in April.

- Writing - week 19-21 (09/06 - 29/06)

  The final stage is the writing phase. All of the results will be gathered in the final thesis, and a discussion will be written based on these. Any incomplete work, or work that needs to be repeated will also be done in this phase of the project.

- Supervisors meetings: every Wednesday (Maria + Christian + Rahul). Once a month meeting with Winnie. A presentation to show the overall progress of the project to the research group will be scheduled approximately halfway through the thesis period.

- Data analysis: performed along simulations and measurements in lab.

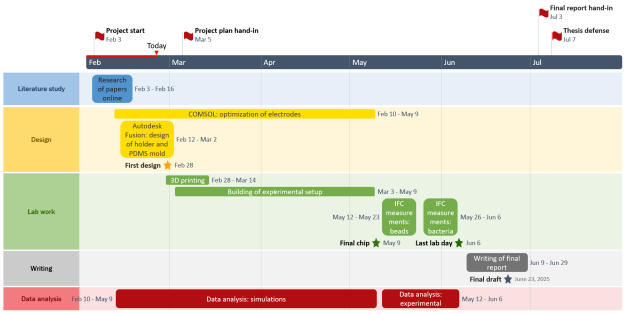

Figure D.1: Timeline for project plan.

D.5 Risk assessment

There will be risks associated with a project that includes a significant amount of experimentation. For this project, these are as follows:

- the signal cannot be made totally independent from the position of the particle along the channel height due to intrinsic design characteristics or fabrication limitations.

- microfluidic channels may get clogged if the channel is too small or the concentration of beads/bacteria is too high, causing delays in the project.

- the whole fabrication process may be subject to delays, due to the complexity of achieving the required resolution in order to trap and analyze bacteria. Furthermore, availability of the necessary machines is to be taken into account.

- the behaviour of bacteria cannot be predicted, and issues such as snapping or sticking to walls may be encountered, so that their characterization may even not be achieved.

- COMSOL simulations may not converge or take too long to complete, so that a trade-off between accuracy and time constraints should be preferred.

D.6 Final comments

The initial timeline was quite accurate for the first part of the project, but delays were encountered towards the end. Unexpected issues prevented the acquisition of data, which was achieved unfortunately too late to perform a more thorough analysis.

The goal of the project shifted slightly along the way, as less focus was put into the maximization of SNR and more efforts were made in the successful building and testing of the experimental setup.